

# Journal of Biomedical Optics

BiomedicalOptics.SPIEDigitalLibrary.org

## Optical coherence tomography today: speed, contrast, and multimodality

Wolfgang Drexler  
Mengyang Liu  
Abhishek Kumar  
Tschackad Kamali  
Angelika Unterhuber  
Rainer A. Leitgeb

**SPIE.**

# Optical coherence tomography today: speed, contrast, and multimodality

Wolfgang Drexler,\* Mengyang Liu, Abhishek Kumar, Tschackad Kamali, Angelika Unterhuber, and Rainer A. Leitgeb

Medical University of Vienna, Center for Medical Physics and Biomedical Engineering, Waehringer Guertel 18-20, A-1090 Vienna, Austria

**Abstract.** In the last 25 years, optical coherence tomography (OCT) has advanced to be one of the most innovative and most successful translational optical imaging techniques, achieving substantial economic impact as well as clinical acceptance. This is largely owing to the resolution improvements by a factor of 10 to the sub-micron regime and to the imaging speed increase by more than half a million times to more than 5 million A-scans per second, with the latter one accomplished by the state-of-the-art swept source laser technologies that are reviewed in this article. In addition, parallelization of OCT detection, such as line-field and full-field OCT, has shortened the acquisition time even further by establishing quasi-akinetic scanning. Besides the technical improvements, several functional and contrast-enhancing OCT applications have been investigated, among which the label-free angiography shows great potential for future studies. Finally, various multimodal imaging modalities with OCT incorporated are reviewed, in that these multimodal implementations can synergistically compensate for the fundamental limitations of OCT when it is used alone. © The Authors. Published by SPIE under a Creative Commons Attribution 3.0 Unported License. Distribution or reproduction of this work in whole or in part requires full attribution of the original publication, including its DOI. [DOI: 10.1117/1.JBO.19.7.071412]

Keywords: optical coherence tomography; multimodal imaging; photoacoustic imaging; nonlinear optical microscopy; optical coherence angiography; akinetic swept source.

Paper 140082VSSR received Feb. 11, 2014; revised manuscript received Apr. 4, 2014; accepted for publication Apr. 25, 2014; published online Jul. 31, 2014.

## 1 Introduction

Optical coherence tomography (OCT) is one of the most innovative and rapidly emerging optical imaging modalities in the last decades<sup>1–4</sup> because it is capable of perfectly noninvasively exploiting the wealth of morphologic and functional tissue information in the first few millimeters of organs. Since the beginning of OCT in the late 1980s and beginning of the 1990s,<sup>5–7</sup> more than 50 OCT companies have been created, more than a hundred research groups are involved in OCT, over a thousand OCT patents have been granted, and more than ten thousand research articles have been published—mostly in ophthalmology, followed by technology-related journals and cardiovascular publications (<http://www.octnews.org/>). In ophthalmic diagnosis especially, OCT is the fastest adopted imaging technology in the history of ophthalmology. While 108 million x-rays, 30 million single-photon emission computed tomographs (CT), positron emission tomographs, and CTs, and 26 million magnetic resonance (MR) imaging examinations have been performed in 2010, ~32 million ophthalmic OCT scans have already been conducted (<http://www.octnews.org/>). In >110 years of x-ray imaging development, the bionizing radiation dose has been reduced by 1500 times; imaging speed is 257,000 faster; its contrast significantly increased and the images are much less blurry.<sup>8</sup> In <20 years of OCT development, on the contrary, the axial resolution has been improved by >10 times; the imaging speed is increased by more than half a million times; image contrast is greatly enhanced and many functional extensions of OCT have been developed.

The original idea of OCT was to enable noninvasive optical biopsy, i.e., the *in situ* imaging of tissue microstructure with a

resolution approaching that of histology without the need for tissue excision and processing.<sup>9</sup> Thus, we have the following prerequisites: (1) visualization of subcellular morphology (i.e., ultrahigh isotropic resolution), (2) three-dimensional imaging (resulting in the need for ultrahigh imaging speed), (3) sufficient (tissue) contrast, (4) molecular, biochemical sensitivity (i.e., sensitive to absorption of diagnostically relevant endogenous or exogenous chromophores), (5) localized (quantitative) functional tissue information, and (6) sufficient (diagnostically relevant) tissue penetration. Axial resolution improvement (prerequisite 1) has been the key technological milestone in the history of OCT in its first decade,<sup>10–14</sup> which has been achieved by using ultra-broadband sources. OCT imaging speed improvements (prerequisite 2) evolved in its second decade, which were accomplished by Fourier domain (FD)/spectral domain (SD)<sup>15–18</sup> and swept source (SS) OCT.<sup>19–23</sup> While in FD/SD OCT speed is mainly determined by the readout time of the camera in a spectrometer, the wavelength-tuning speed of swept sources is the decisive factor in SS OCT. In the past 5 to 10 years, different swept source technologies have emerged to significantly improve imaging speed in (commercial) OCT systems—especially the ones using wavelengths >1 μm. In the present paper, the state-of-the-art (ultra)high-speed SS technologies are reviewed and compared (cf. Sec. 2.) and an outlook of even further improving OCT imaging speed via parallelization (line- and full-field OCT) of OCT detection is presented (cf. Sec. 3). OCT contrast enhancement (prerequisite 3) has been accomplished by introducing polarization-sensitive OCT,<sup>24–28</sup> phase-sensitive OCT,<sup>29–33</sup> optical coherence elastography,<sup>34–39</sup> spectroscopic low coherence interferometry,<sup>40–43</sup> elastic scattering spectroscopy,<sup>31,44–46</sup> and nonlinear interferometric vibrational imaging (NIVI), as well as employing endogenous or exogenous contrast.<sup>47–52</sup> In this paper, a recently developed contrast

\*Address all correspondence to: Wolfgang Drexler, E-mail: [Wolfgang.Drexler@meduniwien.ac.at](mailto:Wolfgang.Drexler@meduniwien.ac.at)

improvement for OCT, named label-free optical angiography, is reviewed (cf. Sec. 4). Some of the above-mentioned contrast enhancement OCT extensions are targeted to enable OCT molecular and biochemical sensitivity (prerequisite 4) as well as localized (quantitative) functional tissue information (prerequisite 5), with the most successful one being Doppler OCT. Though having been improved in many aspects, OCT so far is still not sensitive enough to provide absorption contrast or biochemical and molecular information. Therefore, multimodal optical imaging modalities with OCT incorporated have become a hot research topic. In this paper, the following combinations are reviewed: OCT with multiphoton tomography (MPT, for subcellular resolution); OCT with nonlinear microscopy (for label-free molecular tissue information, cf. Sec. 5.1); and OCT with photoacoustic imaging (for enhanced absorption sensitivity and penetration depth—prerequisite 6, cf. Sec. 5.2). Previous reviews of OCT focused on advanced screening in the fields of primary care,<sup>53</sup> microscopy,<sup>54</sup> rapid tissue screening,<sup>55</sup> phantoms,<sup>56</sup> high speed,<sup>57</sup> and translational research,<sup>58</sup> while recent application-specific OCT reviews covered ophthalmology,<sup>59–61</sup> cardiology,<sup>62–66</sup> dermatology,<sup>67–70</sup> novel applications in pulmonary medicine,<sup>71</sup> cancer,<sup>72</sup> and optical coherence elastography,<sup>73</sup> as well as OCT post- and signal processing.<sup>74,75</sup> This review focuses on high-speed technology (SS light technology and parallelization of OCT detection), label-free angiography, and multimodal OCT.

## 2 Swept Source Lasers for OCT—Light Source Technology Enhancing Imaging Speed

Despite the boom of new SS technologies in recent years, it is noteworthy that none of them is at the moment even close in maturity and reliability to that of the superluminescent laser diodes (SLDs) that have been already employed in (commercial) OCT systems. Nevertheless, swept sources seem to be the OCT technology of the future since they have the potential to offer significantly higher scanning speeds, extended depth range with significantly reduced sensitivity roll-off, reduced fringe washout from sample motion or rapid transverse scanning, and improved light detection efficiency due to dual balanced detection. SS OCT avoids the need for spectrometers with line scan cameras, but requires a high-speed, narrow line width swept source. Spectrometers have limited spectral resolution due to the grating resolving power, beam spot size, and finite pixel dimensions of the line scan cameras. Narrow line width swept source enables spectral resolution in SS OCT, which can be much higher than that of SD OCT. For OCT applications using wavelengths  $>1\text{ }\mu\text{m}$ , SS OCT seems to be the most promising technology of choice because indium gallium arsenide (InGaAs) line cameras are limited in speed and number of pixels, and are more expensive than silicon line cameras. SD OCT suffers from significantly more SNR roll-off with scanning depth than that achievable by using narrow line width swept sources. The seven most important swept laser technologies (from six companies; cf. Table 1) are reviewed and compared in terms of their potential for (commercial) OCT systems. Only those technologies that have been commercialized or are on the verge of commercialization have been reviewed. Novel emerging scientific approaches for swept sources are not considered in this paper.

### 2.1 Axsun Technologies Inc., Massachusetts (“a Volcano Company”)

The laser engine consists of a swept laser module, control electronics, *k*-clock, balanced receiver, and data acquisition board, which samples on *k*-clock transitions (information in this section is from [www.axsun.com](http://www.axsun.com)). More specifically, it contains a reflective microelectromechanical system (MEMS) tunable Fabry-Perot filter, a broadband gain chip, and a fiber reflector that forms the other end of the laser cavity and serves as the output coupler. Filter tuning is accomplished by changing the drive voltage on the MEMS filter. Fiber extension brings the equivalent air length of the cavity to 104 mm such that there are a handful of laser cavity modes underneath the filter at all times. The fact that this external cavity laser operates with a cluster of modes, rather than a single mode, leads to a coherence length that is an order of magnitude or more smaller than single-mode semiconductor lasers. Multimode operation can also increase relative intensity noise (RIN) though. The 100-kHz laser operates with two pulses traveling in the cavity at once separated by half the cavity round-trip time. With longer path mismatches, pulses can interfere with their neighbors, leading to the coherence revival phenomenon. This external cavity laser uses a digital *k*-clock, which is derived from a fiber-based Mach-Zehnder interferometer. Main envisaged innovations include doubling the scanning speed to 200 kHz and increasing coherence length by adjusting the filter bandwidth.

### 2.2 Hamamatsu Photonics K.K. (NTT-Advance Technology Corp.), Tokyo, Japan

A high-speed KTA1-xNb<sub>x</sub>O<sub>3</sub> (KTN) light deflector is used in an external-cavity laser (Littman-Metcalf cavity configuration) that has no moving parts (mechanical free high-speed operation) (information in this section is from [www.ntt-at.com](http://www.ntt-at.com)). It deflects light using an electro-optic effect. KTN has a very large electro-optic effect (20× higher than lithium niobate), which changes a refractive index by an applied voltage and bends the path of a light beam in a direction. The KTN crystal is precharged by applying  $\pm 500\text{ V}$  dc for 10 s and then scans the laser wavelength by applying a  $\pm 400\text{ V}$  sinusoidal voltage to the crystal. However, KTN simultaneously exhibits the characteristics of a cylindrical convex lens because of the trapped electrons. This convex lens is compensated with a cylindrical concave lens because the lens power inside the cavity degrades the instantaneous line width of the laser. At the moment, the scanning wavelength range is  $\sim 80\text{ nm}$  with 20 mW output power and up to 200 kHz (sinusoidal) sweep speed with a  $\pm 400\text{ V}$  deflector driving voltage at 1310 nm. The duty ratio changes from 50:50 to 70:30—at the moment, 200 kHz drive signal with one-way imaging—enabling a 50% duty cycle. Main envisaged innovations include 100 nm sweep width, 20 mW optical output power at 1310 nm with 200 kHz sweep rate and 8 mm coherence length—equivalent to 4 mm scanning depth ( $-6\text{ dB}$  signal roll-off), standard deviation of timing jitters between adjacent A-lines: <200 ps, which corresponds to a phase difference of <0.05 rad at a path difference of 1.5 mm of a Michelson interferometer.

### 2.3 Insight Photonics Solutions Inc., Lafayette, Colorado

Sweep flexibility of the akinetic laser is purely software-driven. The all-semiconductor laser’s distributed Bragg reflector-

**Table 1** Comparison of state-of-the-art swept source technology.

Device/system	Specific performance					Comments (pros and cons)
	Sweep speed	Sweep width	Output power	Phase stability, duty cycle	Coherence length	
<b>Axsun optical coherence tomography (OCT) engine</b>	100 kHz	100 to 140 nm (at -10 dB) at 1050 and 1310 nm	15 to 20 mW	50% duty cycle 12 mm double pass coherence length (-3 dB)		Longest on the market; hence, it should be most mature source, 200 kHz demonstrated
<b>NTT-AT KTN based, mechanical free swept source</b>	200 kHz	80 nm (at -10 dB) at 1310 nm	20 mW	50% duty cycle 6 mm round trip coherence length		Application of ±500 V dc and sinusoidal ±400 V for sweeping At the moment only at 1310 nm; low duty cycle
<b>Insight akinetic swept source</b>	4 to 400 kHz (OCT imaging demonstrated up to 200 kHz at 1550 nm and 102 kHz at 1310 nm)	40 to 80 nm at 1550 nm 30 to 60 nm at 1310 nm (flat sweeping shape -0.015 dB optical flatness)	2 to 13 mW at 1550 nm 2 to 15 mW at 1310 nm	0.5 mill radians noise and phase stability <1.8 pm root mean square (RMS) or 8 pm pk-pk 5 to 95% duty cycle adjustable for unidirectional sweep >200 mm double pass		Easy to use, compact, flexible scanning speed, direct k-clock Centimeters of coherence length (sufficient), relative intensity noise comparable to FDML, limited sweep range, yet more power needed, no source at 1050 nm, yet OCT imaging at speeds >200 kHz needed
<b>Santec MEMS-based swept source</b>	50 kHz/100 kHz at 1050 and 1310 nm	>110 nm (at -10 dB)	>50 mW	>18 mm (100 kHz) to 40 mm (50 kHz) double pass coherence length (-6 dB)		High optical power
<b>Thorlabs MEMS-VCSEL swept source</b>	50 to 580 kHz 1.2 MHz demonstrated	100 nm at 1050 and 1310 nm (at -10 dB)	10 to 20 mW	1.5 mrad at 0.3 mm 50% (unidirect.) 90% (bidirectional) >200 mm coherence length		No flat spectral sweep shape No 850-nm source, yet impressive coherence length and sweep speed
<b>Exalos external cavity laser with resonant MEMS-based one-dimensional scanning mirror</b>	40 to 150 kHz at 840 nm 20 to 150 kHz at 1050 nm 2 to 100 kHz at 1250 nm 20 to 150 kHz at 1310 nm 2 to 150 kHz at 1550 nm	60 nm at 840 nm 120 nm at 1050 nm 100 nm at 1250 nm 150 nm at 1310 nm 120 nm at 1550 nm	8 mW at 840 nm 20 mW at 1050, 1250, 1310, and 1550 nm	50% duty cycle 5 to 10 mm coherence length (-6 dB)		Only provider at five wavelength regions Reliable original equipment manufacturer (OEM) supplier for superluminescent emitting diodes
<b>FDML laser</b>	3200 kHz at 1050 nm 5200 kHz at 1300 nm 110 kHz at 1550 nm	120 nm at 1050 nm 220 nm at 1300 nm 115 nm at 1550 nm	>400 mW at 1050 nm >100 mW at 1310 nm >60 mW at 1550 nm	50 to 90% duty cycle 10 mm coherence length		Fastest (megahertz to multi-megahertz) swept sources with most optical power 1050 nm challenging No 850-nm swept source

Note: KTN,  $\text{KTa}_1\text{-xNb}_x\text{O}_3$ ; FDML, Fourier domain mode locked; MEMS, microelectromechanical systems.

like structure increases the finesse of the cavity by a factor of approximately nine times, resulting in a narrow line width (information in this section is from [www.sweptlaser.com](http://www.sweptlaser.com)). The small dimensions of the laser cavity and the fact that the entire cavity is on a single rigid structure substantially reduce cavity length variation. Superior line width and spectral performance are natural outcomes of the very short waveguide design. Experimental data show that moving from any wavelength to an adjacent wavelength with the all-semiconductor laser takes ~2.5 ns. Because the duty cycle is software-controlled, it is adjustable and, hence, can be set to almost any unidirectional

value from 5 to 95%. The all-semiconductor laser is inherently linear and does not require an external optical *k*-clock. The laser self-generates an internal electronic *k*-clock. The laser forces the wavelength to be correct at each of the evenly spaced clock transitions. The all-semiconductor laser does not need the extra cost of parts and integration of an optical *k*-clock, and eliminates the challenges frequently associated with the nonuniform triggering that can occur with external optical *k*-clocks. The result is direct triggering of the data acquisition. No postacquisition resampling is needed, avoiding ghost images and reducing computation time. The akinetic laser has a typical RMS linearity of 0.0012% at

200,000 sweeps per second ( $<\pm 1$  pm;  $\pm 0.2$  GHz) and a linearity span that is typically  $<\pm 0.002\%$  ( $<\pm 2$  pm). Wavelength repeatability of 0.5 pm (standard deviation) and  $\pm 2.5$  pm span (peak amplitude) have been confirmed for the all-semiconductor laser. In air, a wavelength repeatability of 0.5 pm produces a phase error of 0.5 mrad at 0.2 mm (5 mrad at 2 mm). Coherence revival occurs if a laser is simultaneously oscillating at multiple longitudinal modes of the cavity. Because the akinetic swept laser has a single longitudinal mode, the issues with coherence revival in mechanically tuned lasers are largely avoided. Output power in the all-semiconductor akinetic laser is directly controlled on the chip and can be selected from software. Over the life of a laser, the center wavelength will only vary by  $\sim 80$  pm based on life-test measurements taken on similar laser devices. The nonactive coherence length of the all-semiconductor laser is in the range of several tens of meters. This is substantially higher coherence than the  $\sim 200$  nm of currently available all-semiconductor lasers. Main envisaged innovations are user-adjusted coherence length and a software platform allowing detailed control over the laser's behavior. In lab experiments, all-semiconductor lasers have been demonstrated at 1 million sweeps per second. In the long run, it is believed that the akinetic technology can be pushed to roughly 2 million sweeps per second. With an akinetic laser, other power profiles may be tried by the user, under program control, for application-specific optimization without any other changes to the system. The same technology (with a modified substrate) will be employed for 1060 nm. The electronic drive circuitry is identical for 1310, 1550, and 1060 nm. It is also within the bounds of the technology to work with applications at 850 and  $>1640$  nm. The all-semiconductor technology will allow the production of lasers with wavelength coverage of  $\sim 140$  nm and wider in the future. The wafer-scale laser manufacturing technology used for the all-semiconductor laser also grants cost-effectiveness to this product. Use of high-volume telecom supplies for the internal electronics may further reduce the costs for this type of laser.

#### **2.4 Santec Corporation, Komaki, Japan**

Santec is one of the first companies to launch a swept source especially optimized for OCT imaging: an external cavity laser (ECL) with a polygon mirror and a diffraction grating, resulting in high-performance sources with a desirable linear sweep behavior in  $k$  (frequency domain), but suffering from insufficient scaling toward higher speed due to the bulkiness of the polygon mirror, which, in combination with the high price, prevents widespread cost-effective use (information in this section is from [www.santec.com](http://www.santec.com)). ECLs with a polygon mirror are available at 1300 nm (20 kHz/ $> 170$  nm/ $> 20$  mW; 50 kHz/ $140$  nm/15 to 30 mW; 1060 and 1310 nm/60 mm double pass coherence length/1 to 3 kHz/6 to 8 mW; 0.15% linearity/1310 nm/20 kHz/8 mm coherence length  $> 20$  mW) and at 1050 nm (30 to 50 kHz/70 to 120 nm/ $> 12$  mW/6 mm double pass coherence length). These sources will remain research/academic light sources due to aforementioned reasons. Santec also offers MEMS-based swept sources—at least at 1310 nm so far: 100 kHz/ $> 20$  mm double pass coherence length ( $-6$  dB)/105 nm sweep range/ $> 50$  W optical output power, which is also available as an OEM product. This 1310 nm MEMS-based swept source is very similar to the Axsun 1310 nm swept source and is, therefore, considered a proper back-up by some OCT companies. Main envisaged innovations include an MEMS-based swept source at 1050 nm.

#### **2.5 Thorlabs Inc., Newton, New Jersey**

These lasers are the first (in 2012) commercially available MEMS vertical-cavity surface-emitting laser (MEMS-VCSEL) swept sources at 1050 nm (100 nm sweep range at  $-10$  dB) and 1310 nm (150 nm at  $-10$  dB sweep range) (information in this section is from [www.thorlabs.us](http://www.thorlabs.us)). The current tuning range of 150 nm at 1310 nm is the largest reported for any MEMS-VCSEL and is comparable to the 160 nm reported for the FD mode-locked (FDML) laser. First demonstrations of coherence lengths  $> 100$  mm and axial scan rates up to 1.2 MHz have been accomplished. Ultrahigh speed, high-resolution imaging (up to 580 kHz), high-speed, long-depth range imaging (100 kHz), and ultra long-range imaging (50 kHz) have been demonstrated. A further advantage of the MEMS-VCSEL is wavelength flexibility. Adaptation of the same technology to other wavelengths from 450 to 2300 nm appears to be feasible. The VCSEL is optically pumped at 980 nm (for 1310 nm) or 850 nm (for 1050 nm) through a top dielectric mirror, generating tunable 1310 nm emission, which emerges from the top mirror and is fiber-coupled and amplified by a low-noise semiconductor optical amplifier. Efforts to date have focused on optically, rather than electrically, pumped devices—this makes the source more complex and expensive. Though the ultimate low-cost device will be electrically pumped, optical pumping provides a number of performance advantages over electrical pumping, including larger tuning range and better spectral purity. However, MEMS-VCSEL, like other MEMS-based tunable lasers, can be linearized through drive waveform preshaping. Linearized drive waveforms at 200 kHz axial scan rates have also been demonstrated. The duty cycle is  $> 90\%$  with symmetric forward and backward sweeps. Unidirectional frequency sweep of this source results in a 400 kHz A-scan rate with a duty cycle of 50% at 1050 nm. The system phase stability, defined as the standard deviation of the phase differences between sequential A-scans, measured from a mirror in the patient interface at a signal-to-noise ratio of 57.5 dB (ratio of peak to mean noise) and a depth of 0.3 mm was 1.5 mrad, which approaches the theoretical limit. Main envisaged innovations include MEMS actuator designs to increase mechanical resonance frequency to support higher-frequency drive, development of electrical instead of optical pumping for VCSELs for lower cost and miniaturization (since it would eliminate the pump, wavelength division multiplexer coupler, and isolator), and higher bandwidth and optical power at 1050 nm with improved booster amplifier. A further increase of the tuning range to 200 nm may be possible by increasing the number of quantum wells in the gain region, using a wider bandwidth top suspended mirror, and by further increasing the free spectral range. In addition, it should also be possible to multiplex two or more VCSELs with offset bandwidths in order to obtain increased sweep ranges and improve axial resolutions.

#### **2.6 Exalos AG, Schlieren, Switzerland (Exalos Inc., Pennsylvania)**

These lasers are ECLs with a resonant MEMS-based one-dimensional (1-D) scanning mirror and a diffraction grating, resulting in fast tunable sources with demonstrated sweep frequencies up to 200 kHz (information in this section is from [www.exalos.com](http://www.exalos.com)). Due to the use of high-Q resonant MEMS scanners, those sources perform a quasi-sinusoidal sweep in  $k$ , which requires linearization and signal postprocessing.

However, the sweep behavior is highly deterministic and provides ultrastable long-term phase stability. The laser architecture itself is similar to polygon mirrors, flexible in wavelength, and allows for realizing swept sources from the visible to the near-infrared (NIR). Due to the miniaturized filter architecture, this approach allows for compact, cost-effective swept sources. At the moment, the company is the only provider that offers swept sources between 400 and 1700 nm with sweep rates from 2 to 200 kHz in a miniaturized optical butterfly package that also allows the integration of optical reference ( $k$ -clock) interferometers or other optical reference filters for spectral calibration. 10-dB sweep ranges as wide as 80 nm at 840 nm, 120 nm at 1060 nm, 100 nm at 1220 nm, 150 nm at 1300 nm, and 200 nm at 1550 nm, respectively, have been achieved. Clean imaging performance results in no secondary coherence peaks as well as sharp and narrow point spread function peaks without side lobes throughout the imaging. Main envisaged innovations include next-generation ultrahigh-speed 1-D MEMS scanners with mechanical resonance frequencies in the range of 75 to 150 kHz, resulting in 150 to 300 kHz swept sources. Ultra-broadband semiconductor optical gain chips at 840, 1050, and 1310 nm enable ultrawide optical sweep ranges and hence unprecedented axial resolution.

## 2.7 Fourier Domain Mode-Locked Laser

So far, the main impact of FDML lasers has been the demonstration of OCT systems with dramatically higher imaging speed.<sup>21,22,76–78</sup> The first versions have pushed the speed from several 10 kHz line rate, which have been standard for the first FD OCT systems, to several 100 kHz, and later on, FDML lasers have helped to break the barrier of a 1 MHz line rate with swept sources. Besides the higher imaging speed, FDML lasers have been proven useful for many different applications, where good phase stability, long coherence, low laser noise, or similar conditions are required. Despite these many initial applications, only a few applied or clinical studies using FDML have been published. This is partly caused by the difficulty to build proper OCT systems that can handle the high imaging speed and the fast generated huge data sets by these multi-megahertz (MHz) OCT systems. It is interesting to see how the high-speed FDML results have triggered vibrant research efforts to realize non-FDML sources, which can achieve similar performance. It can be expected that the availability of more than one swept laser technology for MHz OCT will spur research on applications to find out where MHz OCT imaging speeds are required. FDML lasers can achieve ultrahigh sweep rates of up to 5.2 MHz by buffering or multiplexing the sweeps. FDML works optimally at 1.3 and 1.5  $\mu\text{m}$  wavelengths where optical fiber dispersion and loss are negligible. However, dispersion can be compensated for using fiber Bragg gratings to improve performance at 1 and 1.3  $\mu\text{m}$  wavelengths. The fact that the laser light is seeded from the last round-trip and that FDML is a real stationary laser-operating regime reduces the RIN of the laser. The good saturation of the laser gain medium enables very high output powers of 100 mW and more.

Necessary swept source technological specifications for future envisaged (commercial) OCT systems in the coming years would be at least 200 to 400 kHz (with preferred unidirectional sweep), with a 100 to 150 nm sweep range (ideally not at -10 dB but as flattop in linear scale and with good optical flatness), optical output power >10 mW, coherence length of 100 to 150 mm, duty cycle (>90%), high phase stability,

linear-in-frequency sweep (picometer range; tenths of gigahertz), and low RIN noise (~ – 150 dB/Hz). At the moment, the perfect swept source for (commercial) OCT in terms of optimum specs, size, price, robustness, and future potential does not exist.

The akinetic, all-semiconductor Insight swept source is extremely easy to use, very flexible, compact, suitable for a miniaturized OCT system (OCT on a chip), and has the potential to be very economical with unprecedented performance. However, it has only been partially explored from an OCT imaging point of view. The VCSEL MEMS-based swept source is no doubt the most developed long-coherence high-speed swept source at the moment. Despite its momentary impressive performance, the short micron scale length of the VCSEL cavity will probably be a risk of generating artifacts due to slight misalignments or long-term instabilities. Furthermore, electrical pumping would be preferred to reduce complexity, costs, and size. Exalos is currently the only provider for swept sources at all five wavelength regions, also including 850 nm. Most of the swept source technology companies entered the market only quite recently. Therefore, an absolutely fair judgment regarding lifetime, stability, and other specifications is challenging. In general, nonmechanical/akinetic swept sources should be a better choice due to the proneness to failure of the mechanical scanning mechanism. The NNT-AT KTN-based swept source is non-mechanical, but seems to be significantly harder to operate and does not promise flexibility and performance features like the akinetic all-semiconductor, akinetic Insight swept source.

## 3 Parallelization of Optical Coherence Tomography—Pushing Imaging Speed Limits

During the last two decades, OCT has seen dramatic improvements in resolution, sensitivity, and speed. For *in vivo* imaging, resolution and speed are strongly linked, since motion blurring degrades not only resolution, but also sensitivity. The faster the acquisition, the shorter is the measurement time, which is, in particular, important for human *in vivo* imaging. The speed performance improvement is impressive: first implementations of OCT systems achieved a few depth scans per second. Nowadays, based on rapidly tuning SS technology, even several millions of such A-scans have been demonstrated. This allows, on one hand, dense sampling of large tissue patches, allowing for a comprehensive insight into tissue morphology, and, on the other hand, new functional imaging modalities profited from an enhanced flexibility. Nevertheless, even ultrafast systems ultimately strike the physical boundaries given by the detection process. Especially for *in vivo* imaging, the applied optical power is limited by laser safety regulations. Increasing, therefore, the speed, i.e., reducing the detection time, without being able to adjust the applied power, reduces the sensitivity, and degrades contrast and image quality. It is, therefore, questionable if systems much faster than 100 to 400 kHz will be used for clinical OCT applications.

A natural way out of this dilemma is to parallelize the detection. The theoretical advantage of full-field parallel OCT (FF OCT) regarding its intrinsic better sensitivity and potentially higher speed has been recognized already with early time domain OCT (TD OCT). Sensitivity in the shot noise limit scales proportional with the number of detected photons back-scattered from the sample. It increases, therefore, with sensor recording time and with optical power. Flying-spot OCT covers

each sampling point for a shorter time as the speed is increased. Parallel recording does not suffer from this limitation. In fact, if the time needed for a flying-spot system to sample a tomogram of, let us say,  $N$  lateral points is  $T$ , then each scan has a recording time of only  $T/N$ . In parallel OCT, in contrast, the full time  $T$  is available for recording at all parallel points. This compensates for the spread of power across the parallel detection channels. The advantage in sensitivity for a parallel system comes now from the possibility to apply more power while still complying with laser safety regulations, since a larger patch of the sample is illuminated. Although feasibility of parallelization of OCT for *in vivo* imaging has been demonstrated, there are some serious challenges that need to be resolved in the future to make it suitable for practical clinical applications. In the following, we will review developments in FF and line-field (LF) OCT and discuss current limitations and possible solutions for establishing parallel OCT and exploiting its potential advantages.

### 3.1 Full-Field Time Domain Optical Coherence Microscopy/Tomography

Conventional TD OCT uses a low-coherence light source to achieve micrometer axial resolution. The light is focused on the sample using a low numerical aperture (NA) microscope objective (MO) to keep the confocal gate long enough to cover the full imaging range in the sample. This avoids the need to move the sample in the Z-direction. Instead, the sample at a given lateral point is scanned in depth by modulating the optical path length of the reference arm at a high speed. By scanning the sample in the lateral direction, *in vivo* B-scans ( $X$ - $Z$  cross-section) with high axial resolution can be obtained.<sup>79</sup> But, the use of a low NA sacrifices the lateral resolution, which is typically on the order of  $\sim 10$  to  $30\ \mu\text{m}$ . Beaurepaire et al.<sup>80</sup> demonstrated that by simultaneously irradiating the FF of view on the sample with a low-coherence light source and detecting the backscattered light using a high-NA MO and a two-dimensional (2-D) charge-coupled device (CCD) array in a Michelson interferometric setup, a 2-D *en face* image ( $X$ - $Y$  cross-section) with high lateral resolution can be obtained. A lateral resolution of two was achieved using an MO of NA = 0.25. The axial resolution was  $8\ \mu\text{m}$ , limited by the low-coherence light-emitting diode light source with a center wavelength at  $\lambda_0 = 840\ \text{nm}$  and bandwidth  $\sim \Delta\lambda = 31\ \text{nm}$  (output power = 20 mW). As the confocal gating was narrow due to the MO with a high NA, the sample was scanned in depth to several hundred microns by moving the sample in the Z-direction to create a three-dimensional (3-D) volume image. The magnitude of the interferometric signal from each pixel of the CCD array was extracted in parallel using a lock-in detection technique.<sup>80,81</sup>

A combination of linearly polarized illumination and modulation of detected interferometric data using a photo-elastic birefringence modulator and an analyzer (45 deg) were used to create phase-shifted data.<sup>80</sup> A linear combination of four phase-shifted data (phase shifted by 0, 90, 180, and 270 deg) is used to produce a signal at a given pixel, proportional to  $A \sin(2\pi\delta/\lambda)$  and  $A \cos(2\pi\delta/\lambda)$ , where  $\lambda$  is the center wavelength of the illumination,  $A$  is the amplitude of the coherent backscattered light, and  $\delta$  is the optical path length difference between the light from the reference mirror and backscatters in the corresponding sample voxel.<sup>80</sup> The CCD camera (Dalsa, CA-D1, pixels) offered a frame rate of 200 Hz, but the frame grabber (IC-PCI, Imaging Technology Inc.) limited the frame rate to 50 Hz. Sixty-four quadruplet images were

acquired to produce an *en face* image [ $500 \times 500\ \mu\text{m}^2$  field of view (FOV)] in 5 s with a reported sensitivity of  $\sim 100\ \text{dB}$  ( $300\ \mu\text{W}$  power on sample). Images of plant cells, such as onion cells, were shown up to the depth of  $\sim 200$  to  $350\ \mu\text{m}$ . Dubois et al.<sup>82</sup> further improved the resolution of the system by modifying the system into a Michelson interferometer with a Linnik type configuration with MOs of the same NA in both the reference and the sample arms. The same light source, signal modulation, and detection system were used as in Ref. 80. A higher lateral resolution of  $0.7\ \mu\text{m}$  and axial resolution of  $2.8\ \mu\text{m}$  were reported using the MO with a high NA of 0.5. A depth penetration of only up to  $150\ \mu\text{m}$  was achieved. The lateral resolution degradation with depth was attributed to the increase in multiple scattering of light with depth in the sample. The measured sensitivity of the system was reported to be  $\sim 82\ \text{dB}$ . *En face* images of onion cells with fields of view of  $160 \times 160\ \mu\text{m}^2$  and  $370 \times 370\ \mu\text{m}^2$  were acquired in 0.5 and 1 s, respectively. However, the speed was not enough to image a moving sample, and thus, the imaging was restricted to *ex vivo* samples. Grieve et al.<sup>83</sup> demonstrated 3-D ocular tissue imaging with cellular-level resolution using an ultrahigh-resolution FF TD OCT setup. The system was based on a Michelson interferometer with a Linnik type configuration. A tungsten halogen lamp was used as a light source with a center wavelength of  $\lambda_0 = 770\ \text{nm}$  and a bandwidth of  $\Delta\lambda = 350\ \text{nm}$ . The low coherence of the light source provided a very high axial resolution of  $0.7\ \mu\text{m}$ . A high lateral resolution of  $0.9\ \mu\text{m}$  was achieved using an MO with NA = 0.5. A piezoelectric transducer (PZT) in the reference arm was used to modulate the optical path length in the reference arm to produce the phase-shifted images. An *en face* image (500 × 500 pixels) was acquired in 1 s. However, again due to the limited imaging speed, only *ex vivo* ocular tissue samples (cornea, lens, retina, choroid, and sclera) of rat, mouse, and pig were imaged. It was reported that a sample displacement of  $<1\ \mu\text{m}$  was necessary during the time scale of image acquisition.<sup>83</sup> Oh et al. demonstrated better depth penetration in tissue by using a Xenon arc lamp as a light source and an InGaAs camera (SU320 MSW-RS170, 12 bit, 60 Hz) in an ultrahigh-resolution FF OCT setup.<sup>84</sup> InGaAs cameras have better spectral response in the wavelength range of the Xenon lamp source (0.9 to  $0.4\ \mu\text{m}$  wavelength range) as compared to Si-cameras. Moreover, at longer wavelengths, the effect of multiple scattering is reduced. Depth penetration of  $\sim 800\ \mu\text{m}$  was demonstrated by this setup in human thyroid tissue. The reported axial and lateral resolutions achieved were 1.9 and  $2\ \mu\text{m}$ , respectively.<sup>85</sup> An *en face* image was recorded in 2 s with a sensitivity of 86 dB. Fig. 1 shows the TD FF OCT system based on linnik configuration used by Boccarra et al.

FF TD OCT with an on-pixel signal demodulation and amplification using a smart pixel detector array was demonstrated by Laubscher et al.<sup>87</sup> Although already achieving video rate volumetric imaging, its small sensitivity limited its use for imaging biological tissue.

FF TD OCT has also been extended to endoscopic imaging. It is based on the coupling of two distinct interferometers: one external to the probe and another placed at the distal end of the probe. The external interferometer is used to modulate the source spectrum. The interference between the light reflected from the reference arm and the light back-scattered at different depth in the sample obtained by the interferometer at the distal end is superimposed with the interference signal from the external interferometer on a 2-D camera. The path length difference

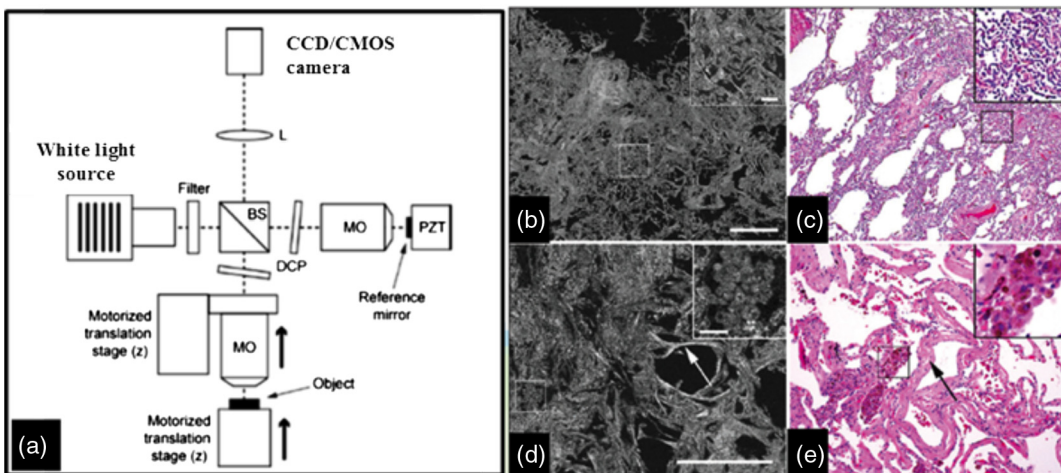


**Fig. 1** (a) Schematic of the FF TD OCT system used by Boccara et al. Figure adapted from Ref. 85. (b–e) Figures taken from Ref. 86 showing comparative full-field optical coherence tomography (FFOCT) and H&E images of non-neoplastic lung with false positive diagnosis. (b, c) Images of non-neoplastic tissue with collapse of normal lung architecture. Boxed areas and insets show dense connective tissue where it is difficult to rule out presence of tumor. (d, e) Images of non-neoplastic tissue showing clusters of smokers' macrophages (boxed areas and insets) and thickened alveolar septa (arrows).

in the external interferometer determines the depth in the sample.<sup>88–90</sup> Oh et al. used a Michelson interferometer as an external interferometer, a Linnik interferometer at the distal end of the optical fiber probe, and a fiber bundle for 2-D image collection. A spatially and temporally incoherent Xenon arc lamp light source was used.<sup>88</sup> Cellular-level imaging at a sensitivity of ~77 dB was demonstrated. However, the imaging speed was too slow (*en face* imaging in 8 s) for any practical clinical application. Also, the use of a Linnik configuration and bulk optics at the distal end of the probe prevented any *in situ* imaging. Ford et al. improved the design by miniaturizing the endoscopic probe by using a Fizeau (common-path) interferometer at the distal end.<sup>89</sup> However, the sensitivity achieved was too low for OCT imaging (~60 dB). Latrive and Boccara were able to demonstrate *in vivo* and *in situ* cellular-level imaging using a rigid endoscopic probe.<sup>90</sup> They also employed a common path interferometer at the distal end and used a Xenon arc lamp as the light source. The axial and lateral resolutions achieved were 1.8 and 3.5  $\mu\text{m}$ , respectively. An *en face* image was obtained in 1 s with a sensitivity of 80 dB. *Ex vivo* images of human breast tissue up to a depth of 40  $\mu\text{m}$  and *in vivo* human skin imaging up to a depth of 20  $\mu\text{m}$  were demonstrated.<sup>90</sup>

### 3.2 Line-Field OCT

The concept of axial-lateral parallel TD OCT was demonstrated by Zeylikovich et al. in 1998, which provides a X-Z cross-section image instead of an *en face* image.<sup>91</sup> The setup typically consists of a free space Michelson interferometer with a broadband light source illuminating a line on the sample using a cylindrical lens in the sample arm. The reference arm has a reflective diffraction grating set in the Littrow configuration with respect to the incoming collimated reference beam. The interference of the image of the grating and the backscattered light from the sample is captured by a 2-D camera. The reference arm is modulated using a PZT to produce phase-shifted signals. The diffraction grating introduces a continuous optical path length delay along the grating dispersion direction. This optical delay allows scanning the sample in depth at each point of the line

illuminating the sample, thus encoding (X-Z) cross-section information. Watanabe et al. demonstrated such a system for high-speed *in vivo* imaging of a human finger.<sup>92</sup> A sample volume of  $5.8(x) \times 2.8(y) \times 2.0(z)$  mm<sup>3</sup> (corresponding to 512×250×512 pixels) was imaged at six volumes per second with a horizontal mechanical scan. An ultrahigh-speed complementary metal oxide semiconductor (CMOS) camera (Photron, 10-bit resolution, at 3000 fps) was used. However, the detection sensitivity was only 76 dB (after 2 × 2-pixel binning).<sup>92</sup>

It has been shown that FD OCT has a sensitivity advantage of 20 to 30 dB over conventional TD OCT.<sup>18,93</sup> Sensitivity well above 80 dB can be achieved in the case of an FD OCT even with low light levels and high-speed detection. This also allows for better depth penetration in the sample. This sensitivity advantage of FD OCT has led researchers to develop LF FD OCT, where an X-Z cross-section image of the sample can be acquired at once rather than an X-Y cross-section (*en face* plane) as in FF TD OCT. The setup typically consists of a Michelson interferometer with an anamorphic illumination system to produce a line illumination on the sample and the reference mirror. The broad bandwidth light reflected from the sample and the reference arm is combined and dispersed using a diffraction grating and detected by a 2-D CCD/CMOS camera. Hence, a spectrally resolved interference signal of each point on the line illuminating the sample can be obtained in parallel. A simple 1-D FFT (after  $\lambda \rightarrow k$  interpolation,  $k$  is wavenumber) along the spectral dimension of the data yields an X-Z cross-sectional image.<sup>94–99</sup> Zuluaga and Kortum were among the first to demonstrate a working LF FD OCT system using a technical sample.<sup>94</sup> Grajciar et al. developed the first LF FD OCT system (shown in Fig. 2) for *in vivo* measurement of the human eye.<sup>95</sup> *In vivo* images of the anterior chamber, iris, and cornea of the human eye were recorded using an SLD light source ( $\lambda_o = 811$  nm, FWHM  $\Delta\lambda = 17$  nm). The detected sensitivity was 89 dB with 2 mW power on the sample. The reported axial and lateral resolutions were 17 and 100, respectively. A full tomogram of size 8 mm(X) × 3.8 mm(Z) was recorded in 1 ms. The degradation of lateral resolution due to cross-talk was reported for the SLD source. A spatially and temporally incoherent halogen

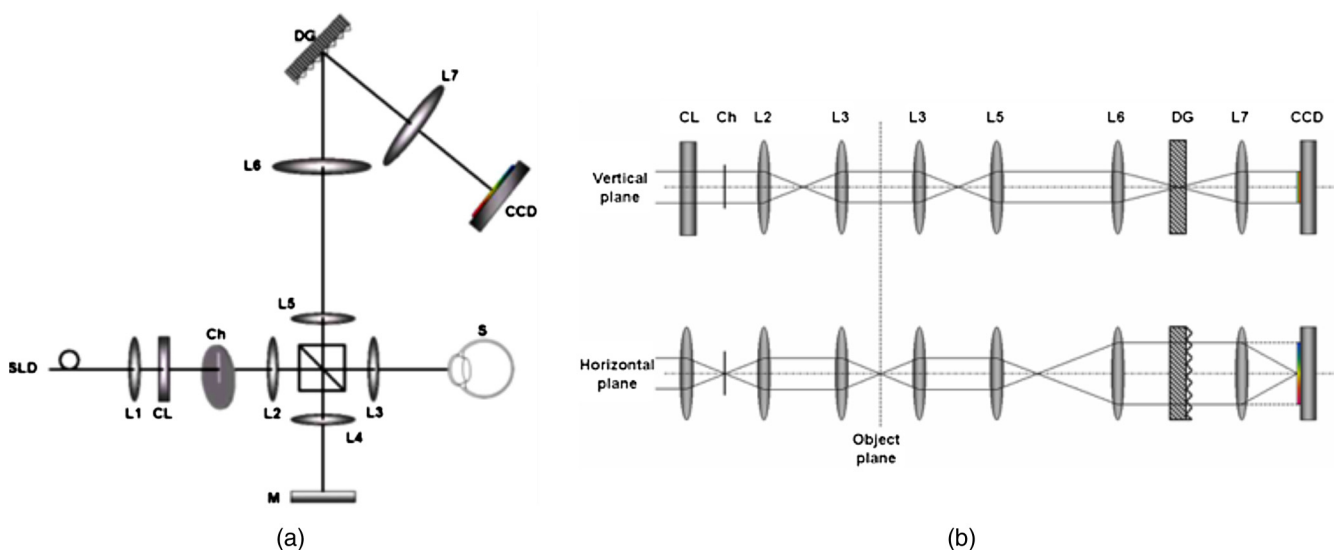


**Fig. 2** (a) Schematic of the line field Fourier domain OCT system used by Grajcar et al. (b) Diagrams of optical paths for the two orthogonal planes of the anamorphic optical system. Figures are taken from Ref. 95.

lamp source ( $\lambda_o = 800$  nm,  $\Delta\lambda = 100$  nm) was also tried to reduce the cross-talk. However, the output power was too low for *in vivo* imaging. Nakamura et al. reported an improved LF FD OCT system for 3-D human retinal imaging.<sup>96</sup> *In vivo* retinal images over a lateral area of  $2.1 \times 2.3$  mm<sup>2</sup> with 256 cross-sectional ( $X-Z$ , 256 A-lines/s) were recorded in 1.3 s. The effective imaging speed of 51,500 A-lines/s achieved was limited by the frame rate (201 fps) of the camera (ATMOS1M60, Atmel Corp., USA, 12 bit). The lateral resolution was  $16.4 \mu\text{m}$  along the parallel direction and  $9.7 \mu\text{m}$  along the scanning direction. The axial resolution achieved was  $7.4 \mu\text{m}$  using an SLD light source ( $\lambda_o = 840$  nm, FWHM  $\Delta\lambda = 50$  nm). It was reported that the ocular aberrations degraded the image quality in the LF OCT system in comparison to the flying-spot FD OCT systems.<sup>96</sup> A sensitivity of 89.4 dB was achieved with 9.7 mW power on the sample. A lateral sensitivity drop of  $-30$  dB was reported at the edges of the measurement, which was attributed to factors such as the spatial coherence cross-talk due to the aberrations, the tolerance, and the extent of the spot size.<sup>96</sup> 3-D LF FD OCT for *in vivo* dermatological investigation has also been reported by Yasuno et al.<sup>97</sup> Zhang et al. demonstrated a combined adaptive optics (AO) and LF FD OCT system for retinal imaging.<sup>98</sup> A flood illumination system was included to aid focusing at different layers in the retina for AO aberration correction. An 843-nm SLD light source ( $\Delta\lambda = 49.4$  nm) was used for LF FD OCT, whereas a 788-nm SLD was used for AO aberration correction. B-scans ( $100 \mu\text{m} \times 500 \mu\text{m}$ ) were acquired at 500 Hz with dynamic aberration compensation at  $\sim 14$  Hz. The reported axial and lateral resolutions were 5.7 and  $3 \mu\text{m}$ , respectively. A maximum detected sensitivity of up to 94 dB was reported. The exposure at the cornea for 843-nm SLD was 1 mW with  $1/3$  deg line illumination at the retina, whereas for the 788-nm SLD, the exposure level at cornea was 0.73 mW with a 1 deg patch illumination at retina. These exposure levels were well below the maximum permissible exposure (MPE) limit according to the American National Standards Institutes (ANSI) standards.<sup>98</sup> It was shown that the detected sensitivity depends on ocular aberrations. A significant improvement of  $\sim 11.4$  dB was achieved by correcting aberrations such as

astigmatism, third order, and higher orders with a focus on the cones. A degradation of 13.1 dB was reported when a defocus of  $\sim 200 \mu\text{m}$  was introduced. Images of subcellular structure in the cone photoreceptors were recorded. The problems such as cross-talk and drop in lateral sensitivity as encountered in other LF FD OCT systems were also reported. A full-range (complex conjugate cancelled) LF FD OCT achieved by dispersion control was reported by Witte et al.<sup>99</sup> The algorithm was adapted from a dispersion encoded full-range method introduced for FD OCT.<sup>100</sup> The robust, fast, and 2-D OCT compatible dispersion encoded full-range method based on an efficient peak-finding algorithm was used to suppress the FD OCT intrinsic mirror image by more than  $-40$  dB and extend the axial measurement range from  $z = -1.6$  mm to  $+1.6$  mm. Full-range single-shot *in vivo* images of fingertip and the anterior chamber of mouse eye *in vitro* were shown. Alternatively to sampling the full signal spectrum for each point along the line using an imaging spectrometer, it is possible to sample the spectrum in time with a line array sensor employing a frequency-sweeping laser. Thus, the problem of spectral cross-talk seen in the spectrometer-based LF FD OCT system is avoided and imaging optics is simplified. Such a system has been reported by Lee et al.<sup>101</sup> The axial resolution achieved with this system was  $8.3 \mu\text{m}$ . A tomogram ( $512 \times 1024$  pixels) was acquired at a speed of 45 fps with a sensitivity of  $\sim 88$  dB.<sup>101</sup>

### 3.3 Full-Field Swept Source OCT

The development of high-speed sweeping (several hundred kilohertz) laser sources has led researchers to investigate their application in an FF OCT setup employing an ultrahigh-speed 2-D camera to increase the imaging speed even more than those of the point scanning SS OCT systems.<sup>102</sup> The FF SS OCT setup usually consists of a free space Michelson interferometer and involves area illumination with a sweeping wavelength laser source on the sample and the reference mirror. The detection of the generated interference signal is performed by a high-speed 2-D camera. The 2-D interference signal is sequentially recorded for each wavelength, and 1-D FFT (after  $\lambda \rightarrow k$

interpolation) is performed along the spectral dimension to get a 3-D volume image with depth information of the sample. Since FF SS OCT is also an FD imaging modality, it enables higher sensitivity as compared to TD OCT systems.<sup>17,18</sup> The interference signal with a varying wavelength can also be recorded in the Fresnel or the Fourier plane instead of the image plane, and digital holographic reconstruction can then be performed on the recorded data to yield OCT equivalent images.<sup>103–105</sup> In the year 2000, Kim demonstrated 3-D imaging of a millimeter-sized biological sample using wavelength scanning wide-field digital interference holography.<sup>103</sup> A wavelength sweeping ring dye laser ( $\lambda_o = 601.7$  nm) was used with a narrow sweeping range of 3.08 nm. As a result, a low axial resolution of only 100  $\mu\text{m}$  could be achieved. Povazay et al. demonstrated an improved FF SS OCT system using a broadband Ti-sapphire laser ( $\lambda_o = 800$  nm,  $\Delta\lambda = 100$  nm) with an acousto-optic frequency tunable element (line width <0.4 nm).<sup>106</sup> The axial and lateral resolutions achieved were 3 and 4  $\mu\text{m}$ , respectively. The detected sensitivity was  $\sim 83$  dB with an average power per A-scan of  $\sim 20$   $\mu\text{W}$ . An acoustic mode-mixer was used to generate different speckle patterns formed due to the different transversal mode of the multimode fiber used for illumination during the exposure time to average out the speckle noise. Due to the speed limitations, only *ex vivo* images of a biological sample (fruit fly) were demonstrated.<sup>106</sup> Later, in 2010, Bonin et al. demonstrated *in vivo* retinal imaging using an FF SS OCT system equipped with an ultrahigh-speed CMOS camera (Y4, Redlake/IDT, Tallahassee, Florida).<sup>102</sup> A-scan rate of 1.5 million A-lines/s was demonstrated for a sample volume of size 640(X)  $\times$  24(Y)  $\times$  512(Z) pixels. An SS laser from Superlum Ireland (Broadsweeper BS840-01,  $\lambda_o = 850$  nm,  $\Delta\lambda = 50$  nm) with an output power of 5 mW was used. The detected sensitivity was only  $\sim 72$  dB with an equivalent power on the sample limited to 92  $\mu\text{W}/\text{pixel}$ . It was noted that at least a 100 Hz sweep rate was required for *in vivo* imaging in order to avoid any significant sample motion blurring.<sup>102</sup>

Wide-field imaging does not introduce a confocal depth gating. This important feature enables collection of out-of-focus light beyond the Rayleigh range. If the amplitude and phase of the out-of-focus signal is known, then numerical holographic reconstruction can be applied to get the focused image. Thus, a uniform lateral resolution can be obtained over the whole imaging range. Hillmann et al proposed Holoscopy, i.e., a combination of wide-field digital lens-less holography and SS OCT to allow focusing beyond the Rayleigh range.<sup>105</sup> The optical setup consists of a lens-less free space Michelson interferometer with a convex mirror in the reference arm to produce a spherical reference wave. The holographic data were acquired with the same sweeping laser as in Ref. 102. For 3-D image reconstruction, the recorded holographic image at each wavenumber was multiplied with the conjugate of the reference wave and propagated to a specific distance using the angular spectrum approach. Finally, the 1-D FFT ( $k \rightarrow z$ ) was calculated to yield an image with depth information. This process was repeated for different reconstruction distances to focus on different depths in the sample. The focused region in each reconstruction was filtered and they were stitched together to get an image with depth-invariant lateral resolution. The axial resolution achieved was 14.7  $\mu\text{m}$ , whereas a lateral resolution of up to 7  $\mu\text{m}$  was achieved. Improvement of over a 30 Rayleigh range was demonstrated using an iron-oxide phantom sample. The detected sensitivity was  $\sim 72$  dB. *In vivo* imaging of a human fingertip was also

shown using an ultrafast camera (FASTCAM SA5, Photron USA Inc., frame rate = 7000 fps).<sup>105</sup> Hillmann et al. further proposed an efficient holoscopy reconstruction method to obtain focused 3-D volume images in a single step.<sup>104</sup> It involves interpolating the recorded 3-D holographic data on a nonequidistance grid in a 3-D spatial frequency space, similar to the inverse scattering reconstruction called inverse synthetic aperture microscopy (ISAM) proposed for FF SS OCT,<sup>107</sup> and then calculating the 3-D FFT to get an OCT equivalent image of the sample. However, unlike ISAM, this method does not calculate the regularized pseudo inverse of the forward-propagating kernel. Instead, the recorded object field is numerically propagated back into the sample volume. A decrease by a factor of 15 in the processing time was demonstrated for an imaging NA of 0.14.<sup>104</sup>

ISAM and holoscopy reconstruction provide 3-D volume images focused over the whole imaging range. But these reconstruction techniques work well only when the sample has a uniform refractive index, the imaging NA is low, and defocus is the main problem.<sup>104,107</sup> However, at a higher NA (>0.2), the effect of higher-order aberrations, such as spherical, astigmatism, coma, etc., becomes dominant. As a result, proper image reconstruction becomes difficult. A computational AO technique has been suggested to reduce higher-order aberration in the case of a phase stable point scanning FD OCT system.<sup>107</sup> But this technique is based on an optimization method that is iterative in nature and increases the computational cost. Numerical complexity increases if the sample is highly inhomogeneous, causing variable aberration with depth.<sup>108</sup> Recently, Kumar et al. proposed a digital aberration correction method, which is, in fact, a digital equivalent of a Hartmann sensor, to deal with variable higher-order aberrations in FF SS OCT.<sup>109</sup> In this method, a 2-D FFT is performed on the aberrated image field corresponding to a layer in the sample to get to the spatial Fourier plane, and then the Fourier data are segmented into small subapertures. 2-D inverse fast Fourier transform (IFFT) s on these segmented Fourier data yield images that are shifted with respect to each other due to aberrations. Cross-correlation of the intensity of these images with respect to a reference image gives shift data from which local slope information of the wavefront error can be calculated. Knowing the slope information, the wavefront error can be calculated using a suitable basis function, such as Zernike's or Taylor monomials. Phase correction can then be applied digitally on the whole Fourier data and an aberration-free image is finally obtained in a single step by calculating the 2-D IFFT. Furthermore, it was shown that this method does not require any *a priori* knowledge of the system parameters. However, this method assumes that the data are uniformly distributed in the spatial frequency plane, i.e., the sample gives diffuse reflection on illumination, and also the spatial coherence is maintained over the FOV. This condition is usually fulfilled when spatially coherent light source is used to image tissue. Aberration corrections on a technical and a biological sample (grape) were demonstrated.<sup>109</sup> Figure 3 shows the SS FF OCT setup used by Kumar et. al and the results obtained by applying digital defocus correction on a grape sample.

FF TD OCT systems achieve cellular-level *en face* images over the depth of few hundred microns into the biological samples with histological-level image quality without the need to stain and histologically prepare the sample.<sup>82–85,88,89</sup> The coherence gating provided by the broadband light source in combination with the confocal gating due to the use of MOs with high NA causes rejection of multiple-scattered

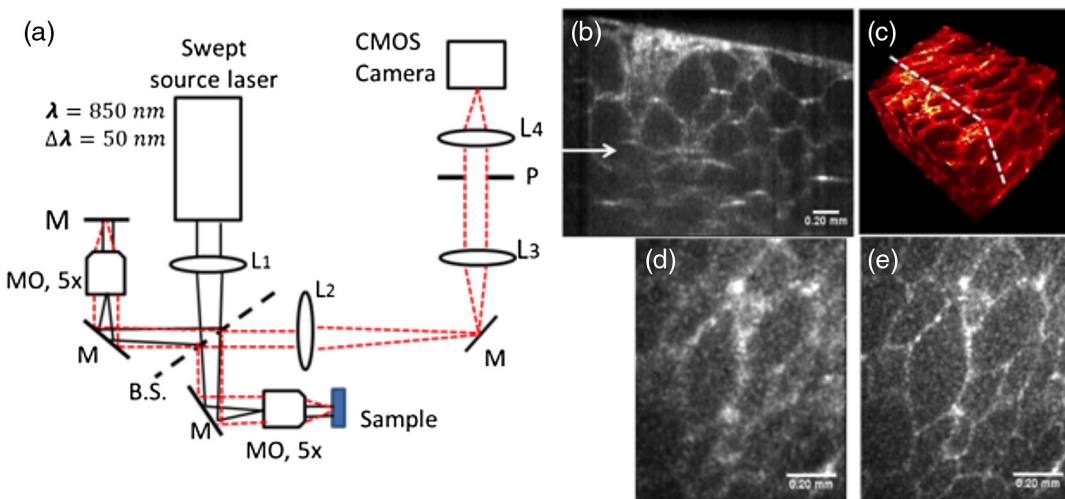


**Fig. 3** (a) Schematic of the FF swept source (SS) OCT system used by Kumar et al. (b) A tomogram of the grape sample. (c) Three-dimensional (3-D) image volume with dotted line showing location of the tomogram shown in (b). (d) Enface image obtained at the depth of 424.8  $\mu\text{m}$  in the grape sample indicated by arrow in (b). (e) is the digitally focused image of (d) obtained using the algorithm described in Ref 109. Figures are taken from Ref. 109.

light and yields high-resolution images. FF TD OCT systems performing rapid thick tissue histopathology have been successfully commercialized.<sup>86</sup> The axial-lateral parallel TD OCT system using an ultrahigh-speed camera has been shown to produce *in vivo* X-Z cross-section images.<sup>92</sup> However, due to the sensitivity limitation of the TD OCT configuration, and increased cross-talk due to multiple scattering with depth, the useful imaging range is limited to few hundred microns in tissue samples.<sup>18,93</sup> The LF FD OCT systems have been shown to produce *in vivo* images with higher sensitivity (>80 dB) over a longer imaging range.<sup>95–99</sup> However, they suffer from problems such as cross-talk (speckle noise) due to multiple-scattered light affecting the lateral resolution, spectral cross-talk along the dispersion direction, and a drop in sensitivity at the edges of the images due to the Gaussian illumination. These problems can be mitigated by using a spatially incoherent light source<sup>95</sup> with uniform illumination along the line and by improving the imaging optics. The FF SS OCT system has also been shown to produce *in vivo* retinal images using an ultrahigh-speed camera.<sup>102</sup> However, the sensitivity was limited to ~72 dB because of the low output power of the sweeping laser source used. Also, the coherent noise caused by backreflections from the lenses in the optical system, which is difficult to avoid in the FF OCT setup, causes reduction of the dynamic range of the detector.<sup>102</sup> A lens-free holoscopy system combining wide-field digital holography with FD OCT has been suggested to mitigate this problem. Wide-field imaging allows for the collection of out-of-focus light and FD imaging provides easy access to the phase information of the detected signal. This enables numerical refocusing of out-of-focus signals beyond the Rayleigh range to produce 3-D image volume with uniform lateral resolution.<sup>104,105</sup> A digital adaptive optics technique based on subaperture correlation has also been implemented in FF SS OCT to correct for higher-order aberrations that can occur in high-NA imaging of a non-uniform sample.<sup>109</sup>

The use of an SS laser in the FF OCT setup has simplified the whole imaging system as no scanning of the sample is needed. The LF SS OCT requires scanning only in one transverse direction. LF and FF OCT setups employ a line and an area

illumination onto the sample, respectively, and, hence, allow for a higher MPE limit as compared to any point scanning system where the illumination beam is focused into the sample. The use of higher power theoretically implies higher sensitivity even at higher speed when the exposure time is very short. Although the feasibility of parallelization of OCT for *in vivo* imaging has been demonstrated, there are some serious challenges that need to be resolved in future to make it suitable for practical clinical applications. Due to parallelization, there is an inherent problem of cross-talk or speckle noise caused by multiple-scattered light. This makes FF SS OCT unsuitable for imaging tissue where multiple scattering is high. However, FF SS OCT may work for ophthalmic imaging where tissues are relatively transparent and multiple scattering is less pronounced. LF FD OCT or LF SS OCT is expected to suffer less from spatial cross-talk as compared to FF SS OCT as it rejects multiple-scattered light along the scanning direction. But, at present, there is no study that directly compares and quantifies the multiple-scattering effects in FF and the LF OCT setup. The use of multimode fibers with mode-mixing techniques has been suggested for destroying the lateral spatial coherence to reduce cross-talk.<sup>106,110</sup> However, the destruction of lateral spatial coherence may destroy phase correlation over the FOV, which is necessary for holographic reconstruction of focused 3-D volume data or any digital aberration correction method. The use of programmable array illumination may be a viable option to separate signals from adjacent parallel channels in time and space to reduce cross-talk while preserving the phase correlation across the lateral FOV.<sup>111</sup> But the feasibility of such a system for *in vivo* imaging has to be tested in the future. There are other technological limitations such as the nonavailability of high-speed and high-power broadband commercial sweeping laser sources at 800 nm suitable for ophthalmic imaging using FF or LF SS OCT. Currently, the strongest bottleneck seems to be the commercially available ultrafast cameras that are economical in cost with low read noise when run at high speed.<sup>102</sup> The reduced cross-talk advantage (along the scanning direction) of the LF OCT system over the FF OCT needs to be quantified in the future, and its application to skin tissue imaging needs to be

investigated. However, for tissue imaging, an 1100 nm SS laser source would be needed, as this wavelength range enables reduced multiple scattering and deeper penetration into the tissue. Also, the commercially available fast CCD/CMOS cameras use silicon-based detectors, which have low sensitivity around 1100 nm. The InGaAs cameras have higher sensitivity around this spectral range, but, currently, they offer lower frame rates as compared to most CCD/CMOS cameras. It is hoped that with technological developments, these issues can be resolved and parallelization in OCT may turn out to be a viable option for imaging in the future.

#### 4 Label-Free Optical Angiography

A shortcoming of OCT is its missing tissue specificity as its contrast mechanism is backscattering. Functional extensions of OCT have the potential to partially mitigate this drawback. They are, therefore, extensively investigated and received additional impetus by the recent technical advances in high-speed sensors and laser technology. Above all, Doppler OCT has matured during the last years to become a reliable method for quantifying blood flow in tissue, as well as for depth-resolved label-free micro-angiography providing unprecedented details of tissue capillary networks. In the following, the approaches for optical angiography are presented, and their advantages, applications, and still open questions are discussed.

The gold standard for performing angiography in the eye is fluorescence angiography (FA). In other organs, CT angiography or MR angiography are mostly used, as they give access to deep vascular structures within the body. Their disadvantage, which is shared with FA, is the need for administering contrast agents that might lead to adverse side effects for the patients. This hinders the possibility for the screening of large populations, which would be advantageous for detecting vascular-related diseases early on, with a huge socioeconomic benefit. Optical angiography will not be able to change the imaging paradigm for deep vascular structures; however, for superficial vascular and microvascular plexuses, including retinal and choroidal vessels, the situation is very different. The eye itself can be seen as a window to the brain, as neural retinal tissue and its perfusion is directly accessible by optical means. Optical angiography based on OCT provides concise 3-D vascular maps that allow distinguishing between different retinal perfusion layers, and also the important choroidal vasculature. Especially, the development of new light source technology operating in the NIR region at  $\sim 1 \mu\text{m}$  wavelength helped to improve contrast for deeper choroidal structures, as longer wavelengths experience less scattering. Apart from ophthalmology, there is also an increasing need and vivid interest to access vasculature and perfusion in dermatology. Recent work demonstrated the capabilities to contrast skin microvasculature in healthy skin as well as in different pathological alterations, including skin cancer. Most pathologies start in the superficial skin layers in the first hundreds of micrometers that are easily accessible by OCT. There are characteristic vascular patterns that might, in the future, be used as biomarkers of disease. For deeper organs, such as the gastro-intestinal tract, or for head and neck diseases, specific delivery probes are needed.

Given the exciting prospects of OCT angiography, it has been the subject of active and proliferative research during the last decade. Early developments based on TD OCT include speckle and phase variance and power Doppler imaging.<sup>112,113</sup> The disadvantages of TD OCT were, however, its limited sensitivity and

speed for 3-D angiography. This changed with the introduction of FD modalities,<sup>18,114</sup> which paved the way for the exciting developments in optical angiography that we see today. Methods based on FD OCT soon adapted the phase approaches from TD OCT.<sup>115,116</sup> However, the differences of the data acquisition process and optical setup in FD versus TD OCT opened a large playfield for many new approaches to optical angiography. For example, spectrometer-based FD OCT suffers from fringe washout and sensitivity loss when imaging moving structures.<sup>117</sup> Resonant Doppler OCT turns this apparent downside into an advantage when contrasting moving structures, by dynamically tuning the reference arm delay, matching speeds in both arms.<sup>118</sup> Other approaches use spatial frequency filtering techniques, by making use of the fact that moving structures appear shifted in spatial frequency.<sup>119,120</sup> Alternatively, one can operate on the Doppler histogram,<sup>121</sup> or use support vector machines operating on phase difference data.<sup>122</sup> Advanced post-processing techniques to filter out vessel structures from static bulk can also operate directly on OCT intensity data. This has been successful for retinal vascular structures as well as for choroidal vasculature.<sup>123–125</sup> Employing dual-beam setups that probe the sample in parallel on laterally displaced positions enhances the sensitivity for contrasting vessels with a large range of velocities. Both beams scan the same spot after an adjustable time interval given by the lateral displacement and the scanning speed.<sup>126–128</sup> The possibility of high-speed data acquisition with FD OCT certainly marked a breakthrough for optical angiography. High speed translated directly to smaller motion artifacts, which is important when visualizing small capillary structures, as well as for keeping signal correlation by dense sampling.<sup>129,130</sup> The latter is of particular importance for high-quality vessel contrasting against static bulk tissue in many angiography approaches. Furthermore, high speed enables specific Doppler analysis methods,<sup>131</sup> enhanced velocity bandwidth,<sup>132,133</sup> as well as the possibility of using flexible scanning patterns to further increase the velocity sensitivity.<sup>134,135</sup>

In general, flow contrasting requires comparing two or more scans preferably taken at the same location. The velocity sensitivity of the contrasting technique scales with the time difference between the scans. Even though angiography aims not necessarily at quantifying the flow, it is important to observe a flow signature by looking either at phase differences, intensity, or speckle changes, or at changes of the full complex OCT signal. In order to observe signatures from small capillary flow, relatively long time intervals of typically a few milliseconds between acquisitions are required. They are equivalent to only few hundred scans per second. Obviously, at such an A-scan rate, the acquisition is too slow for *in vivo* volumetric imaging and would also be heavily affected by motion artifacts. On the other hand, with high-speed OCT, it is possible to achieve B-scan or tomogram rates of several hundred scans per second, which is exactly the timing needed for high-sensitive flow contrasting, including the smallest retinal capillaries. Thus, instead of calculating signal differences between A-scans, one considers successive B-scans or parts of B-scans.

The most impressive results with optical angiography have been achieved when calculating the amount of signal decorrelation between two or more scans.<sup>136</sup> As mentioned before, it is possible to observe decorrelation or variance of phase,<sup>137,138</sup> speckle,<sup>139,140</sup> or the full complex signal.<sup>141</sup> An important factor, apart from the time interval, is the oversampling ratio, which is the number of A-scans per spot size of

the scanning beam. Clearly, if the oversampling is too low, signal decorrelation will occur for all structures even without bulk motion, again degrading the blood flow contrast. This imposes important restrictions concerning the covered angular extent on the retina, as typical imaging times for a full volume should be kept to a few seconds. This is, of course, different if a tracking system is employed, allowing for stitching of several recorded volumes of smaller areas. In this case, the B-scan rate might even be slower, as long as the proper correlation between two acquisitions for the static bulk tissue is maintained.

The strategy for obtaining DOCT micro-angiographies with high motion sensitivity is displayed in Fig. 4. It is based on calculating signal differences between B-scans that are taken at the same vertical position. B-scan rates are typically a few hundred hertz. The signal changes are analyzed pairwise between adjacent B-scans in postprocessing. Averaging over several difference images taken from the same lateral position helps to obtain a motion contrast volume  $A(x, y, z)$  with improved vascular contrast and motion sensitivity.<sup>142</sup>

$$A(x, y, z) = \frac{1}{M(y)} \sum_{i=0}^{N-1} \left\{ \left[ \sum_{x,z} D(x, y_i, z) \right] < T \right\} \cdot D(x, y, z), \quad (1)$$

where  $D(x, y_i, z)$  stands for tomograms that represent, in general, differences between either the intensity, the phase, or the full complex OCT signal of successive tomograms at the vertical position  $y$ . The tomogram or fast scanning direction is denoted by index  $x$ . It is, however, important to exclude the difference tomograms with excessive bulk motion artifacts due to involuntary patient motion. This is accounted for by using a threshold  $T$  for the average signal decorrelation across a full tomogram.

The number  $M$  of remaining average difference tomograms at each position  $y$ ,  $D(x, y_i, z)$ , can be formally written as  $M(y) = \sum_{i=0}^{N-1} \{ [D(x, y_i, z)] < T \}$ , with  $N$  the number of B-scans measured at the same position  $y$ . The logic operation in the brackets [see also Eq. (1)] yields 1 or 0 for TRUE or FALSE, respectively. Easy to implement in particular for SS OCT is to analyze changes in the intensity signal. Phase sensitive analysis is strongly affected by trigger jitter, which can, in principle, be solved by using a hardware trigger provided by the source or a reference interferometer signal. However, if the source does not provide a  $k$ -trigger signal for synchronizing the acquisition, intensity-based imaging has clear advantages by being less complex. In order to contrast moving structures, one calculates differences between logarithmically scaled intensity tomograms taken at the same position  $y$ , i.e.,  $D(x, y_i, z) = \log[I(x, y_{i+1}, z)] - \log[I(x, y_i, z)]$ . Static tissue will ideally cancel out, whereas dynamically changing structures, which cause fluctuations in intensity or speckle, remain [Fig. 4(b)].

Most tissue has flat vascular network structures, which are usually best appreciated from *en face* views. They are obtained by integrating the difference signatures over selected depth ranges as shown in Fig. 4(d) for the inner retina capillary structures. The micro-angiography displays integrated capillary structures of the retinal nerve fiber layer down to the outer nuclear layer. The resulting fine vessel network in the parafoveal region allows for precise assessment of vascular density as well as of diagnostically important anatomical features, such as the size of the foveal avascular zone.

A closer look at Fig. 4(b) reveals, however, intrinsic artifacts of highly sensitive motion contrast techniques being signal tails or shadows below vessel cross-sections. They are due to phase

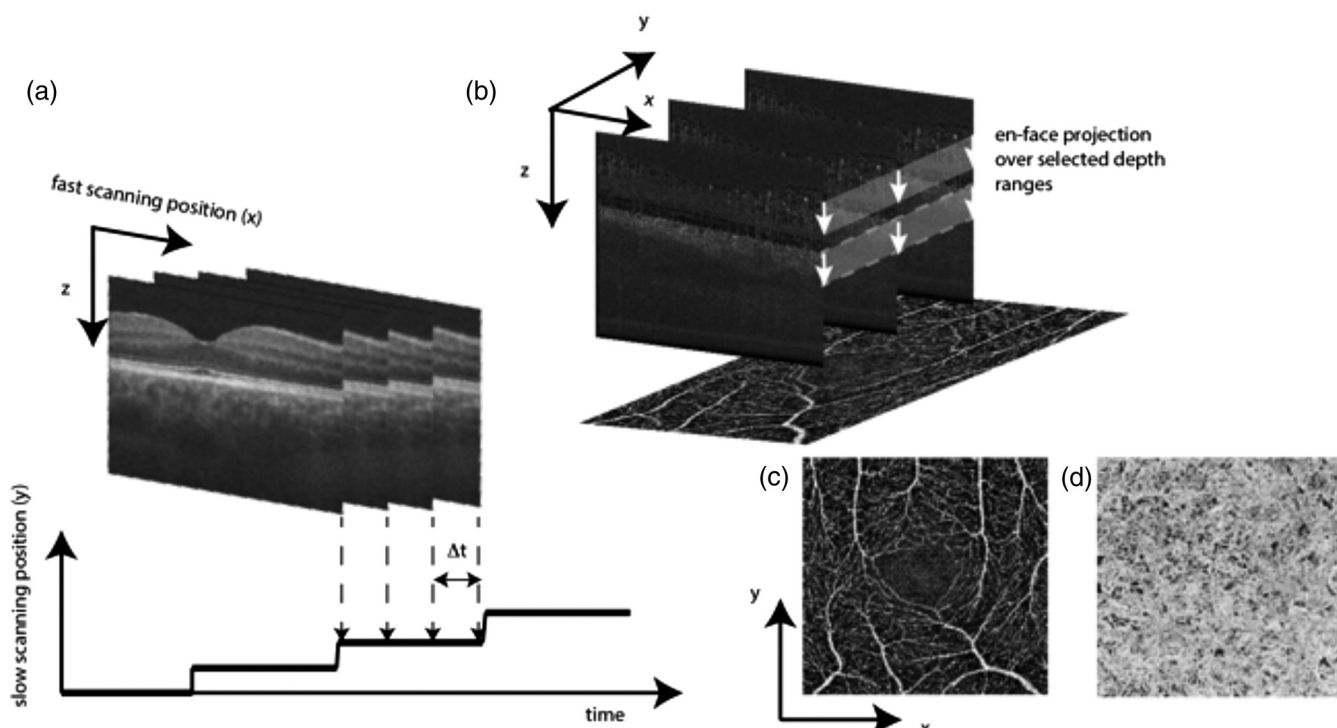


**Fig. 4** (a) Recording scheme for Doppler OCT (DOCT) angiography. (b) Calculated 3-D DOCT angiography. (c) Taking the en-face projection by, e.g., plotting the maximum intensity results in comprehensive en-face angiography maps. (d) Dense choroidal vasculature obtained by integration over dashed depth region in (b).

and speckle decorrelation of light that needs to transverse the strongly scattering blood volume. Multiple scattering, together with the dynamic inhomogeneous refractive index distribution within the vessel lumen, causes phase as well as speckle decorrelation even for light backscattered from static structures below the vessel. Masking or weighting with the original intensity information can reduce this artifact, yielding clearer 3-D rendered angiography maps. An improvement of this artifact has further been accomplished by using Bessel beams for functional tissue imaging.<sup>143</sup> SS OCT usually operates in the longer-wavelength region above a  $1 \mu\text{m}$  central wavelength. Those wavelengths experience less scattering than the ones at 800 nm, allowing, therefore, for better contrast in deeper tissue layers.<sup>144,145</sup> In ophthalmology, it is of increasing interest to achieve better contrast for choroidal structures that lie below the strongly scattering pigment epithelium [Fig. 4(d)].

Figure 5 demonstrates the performance of an intensity-based OCT angiography of a healthy human retina. The image has been obtained with a high-speed FDML SS OCT system, operating at a  $1.06 \mu\text{m}$  central wavelength and achieving a 1.7 MHz A-scan rate.<sup>142</sup> Such speed allows for close to 50 deg large FOV angiography maps of the retina in a fully noninvasive label-free fashion.

The possibility to assess the microvascular structure down to the level of capillaries opens exciting new perspectives in pre-clinical research, in particular for cancer research. Due to the easy label-free contrasting scheme, neovascular growth can be studied *in situ* over time. Figure 6(b) gives an impression of the level of detail achieved with phase variance OCT imaging. The angiography shows features such as satellite metastases that are not visible in the structural OCT image [Fig. 6(a)]. Figures 6(c) to 6(e) demonstrate the sensitivity gain by including an increasing number of frames for the contrasting algorithm.<sup>146</sup>

The method performs equally well even in strongly scattering tissue like human skin. Figure 7 demonstrates the performance of contrasting micro-angiographic details for pathologic skin conditions. A case of basal cell carcinoma, being a nonmelanoma skin cancer, is shown. The gold standard in dermatology is the dermascope, which is basically an epiluminescence microscope to image skin lesions. It yields no in-depth information of the

skin structure, as OCT does. Therefore, OCT is gradually penetrating the dermatology market as well, through dedicated commercially available systems. Still, structural information alone is unspecific, and additional biomarkers of disease are extensively investigated. Most diseases come along with alterations of the microvascular pattern. Thus, methods that are capable of visualizing the patterns in depth are of high diagnostic value. Recent results of OCT angiography indicated that alterations of the vascular pattern are characteristic for different pathologic conditions, such as inflammation, or skin cancer.<sup>147</sup> The expectations to use functional OCT for enhanced diagnosis in dermatology are, therefore, high.

Apart from pure angiography, OCT has also the potential to quantify perfusion in vessels.<sup>112,148,149</sup> For flat vessel beds, signal variance calculations show a linear dependence on the flow.<sup>150</sup> Since most angiographic structures in skin, retina, or the choriocapillaries are parallel to the tissue surface, those methods are currently investigated in detail. Quantitative assessment of the velocity through signal correlation analysis needs, however, fast scan rates in order to avoid complete decorrelation of flow signals. So far those methods have been successfully applied only to well-fixated samples.<sup>151</sup> The reason is the number of correlated scans necessary to perform flow analysis with sufficient dynamics. Bulk motion as well as measurement time might, therefore, be critical for human *in vivo* applications.

For retinal angiography, OCT is in competition with fluorescein or indocyanine green (ICG) angiography. The latter needs intravenous administration of contrast agents, which might lead to adverse side effects for the patient. OCT angiography, on the other hand, does not need dyes and can, therefore, be frequently applied. However, as a motion contrast technique, it does not detect dye leakage. This limits its application for diseases where vascular permeability is altered. Still, for choriocapillary vasculature, the missing sensitivity to leakage is, in fact, of advantage, as the choriocapillaris are fenestrated.<sup>152</sup> This leaves the contrasting of choriocapillaris with fluorescence angiography more challenging due to dye leakage. Most studies of the choriocapillaris have, therefore, been based on postmortem histology or on observation of the temporal perfusion patterns.

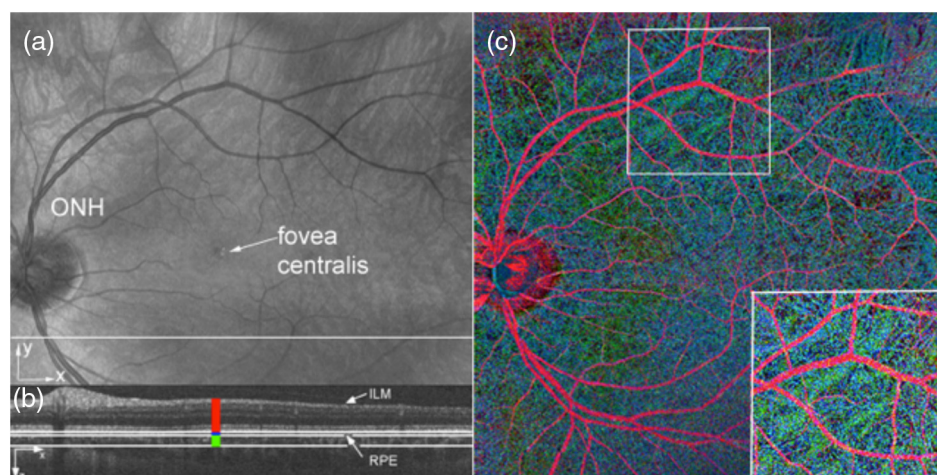


**Fig. 5** Wide field optical angiography over 48 deg. (a) Fundus projection of OCT intensity data. (b) Tomogram taken at indicated line in (a). The colors represent depth ranges for calculating angiography projections. (c) Color coded OCT wide field angiography. White box region is shown zoomed in inlay (from Ref. 142).

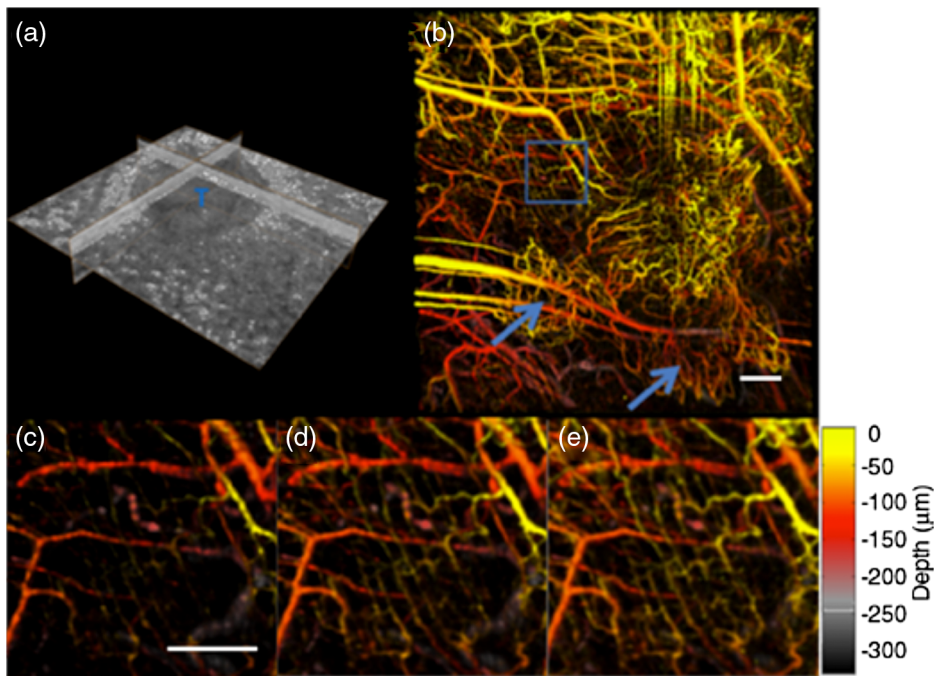


**Fig. 6** (a) OCT intensity image of a tumor. (b) Microvascular projection image calculated over eight B-scans at each vertical position. Blue arrows point to satellite metastases that are not visible in (a). The color indicates relative depth of the vessels. (c) to (e) Magnified region [box in (b)] showing the improvement on increasing the number of B-scans ( $N = 2, 4, 8$ , respectively). Scale bar denotes  $250 \mu\text{m}$  (from Ref. 146).

Knowledge about perfusion pathways is a first step toward understanding the metabolic need. Important additional information is certainly the oxygen consumption. This might be estimated via knowledge of oxygen saturation in the arterial and venous vascular tree. The most common approach for systemic oxygen saturation is pulse oximetry, which, however, is not spatially resolved. Oximetry based on differential spectroscopy, on the other hand, is a spatially resolved method that has been successfully applied to retinal vessels.<sup>153,154</sup> Another approach combines Doppler OCT with hyperspectral imaging for assessing blood oxygenation in tumor vasculature.<sup>155</sup> A relatively young biomedical imaging technique that uses absorption as a contrast mechanism is photoacoustic tomography (PAT) or microscopy (PAM).<sup>156</sup> Multispectral PAM allows for calculating

blood oxygen saturation even in strongly scattering neural tissue.<sup>157</sup> It is, therefore, natural to combine OCT that yields high-resolution anatomic contrast and PAT/PAM that provide absorption or metabolic information. Hybrid imaging approaches with OCT are discussed in Sec. 5.

OCT angiography is a very promising functional extension of OCT that holds great potential for providing additional specific biomarkers of disease. In ophthalmology, the noninvasive and label-free alternative to FA might soon be adapted for commercial OCT platforms. The most important advantage, since no trained specialist is needed for dye administration or for operating the instrument, is the capability of frequent monitoring and large population screening. This is expected to reduce the number of invasive angiographies performed, to

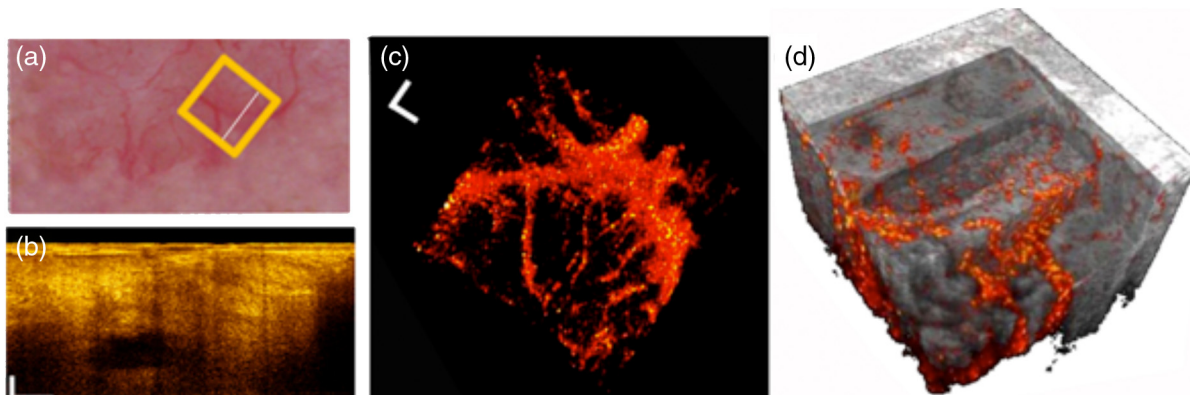


**Fig. 7** (a) Dermascope image of basal cell carcinoma; yellow box denotes field of view of OCT. White line indicates OCT scan position for tomogram displayed in (b). (c) OCT angiography projection. (d) Overlay of OCT angiography (red) to OCT intensity data (gray) (from Ref. 147).

help enhancing early diagnosis of major ophthalmic diseases, as well as to support the understanding of the pathophysiologic mechanisms behind them. In other medical fields, such as dermatology, neurology, cancer research, cardiology, or for endoscopic organ screening, its application is extensively investigated. Further improvement for the clinical applications may also be expected from improved calculation speed for real-time perfusion contrasting using graphics processing units.<sup>158</sup> Without doubt, OCT angiography can be currently seen as the most successful functional extension of OCT that meets immediate diagnostic needs.

## 5 Multimodal Optical Coherence Tomography

### 5.1 Hybrid OCT with Fluorescence and Nonlinear Microscopy

There is a strong need to assess tissue structure and molecular information *in vivo* and in real time with high sensitivity and specificity to circumvent biopsy for improved cancer diagnostics and therapy. OCT provides high-resolution, cross-sectional large-area imaging of tissue microstructures *in situ* and in real time with several millimeters of depth penetration, but one major drawback of OCT is the lack of chemical selectivity, resulting in difficulty in differentiating between pathological and normal tissue with similar morphological or optical properties.<sup>159</sup> To study biological tissue at a cellular level, higher resolution is needed. Confocal microscopy and multiphoton microscopy (MPM) achieve submicrometer resolution with penetration depth limited to several hundreds of micrometers due to severe scattering in biological samples. Compared to confocal microscopy, MPM uses NIR ultrafast lasers to evoke the nonlinear process; therefore, it does not require a pinhole for excluding out-of-focus fluorescence. Due to the use of longer wavelengths, higher penetration depths can be achieved. Ti:sapphire lasers are capable of simultaneously and efficiently addressing the needs for MPM and OCT, respectively, and permit the construction of a combined label-based and label-free imaging platform. Such a platform offers numerous benefits, such as the inherent 3-D sectioning capability, the deeper penetration depth into the sample compared to visible light, and the use of lower average power, which prevents photo damage and photo toxicity, making it an extremely interesting modality for live cell and *in vivo* imaging. The most common nonlinear optical modalities are two-photon excitation fluorescence (TPF),<sup>160</sup> second harmonic generation (SHG),<sup>161</sup> third harmonic generation (THG),<sup>162</sup> and coherent Raman scattering.<sup>163</sup> Each technology provides unique and complementary benefits. High axial and lateral resolution comparable to confocal microscopy without a pinhole can be achieved. Imaging can be performed with either two galvanometric mirrors to scan the beam across the sample or a scanning unit for point-by-point scanning. Filters and dichroic beam splitters are essential to avoid detection of the fundamental laser beam and Rayleigh scattered light. The nonlinear signal can be detected with a single-element detector [photomultiplier tube (PMT)]. TPF and SHG signals are generated simultaneously and can be collected with two photomultipliers. Distinguishing between normal and abnormal tissue types based on morphological and molecular composition will expand the range of noninvasive clinical diagnostic techniques. Noninvasively detecting both chemical and structural changes in healthy as well as diseased tissue can help to diagnose diseases at an early stage, long before structural changes occur.<sup>161–163</sup> Linear

and nonlinear chemically selective imaging methods, such as Raman scattering, coherent anti-Stokes Raman scattering (CARS), or MPM, can be combined with OCT to enable molecular sensitivity in OCT and to simultaneously provide structural and functional information of the tissue. This can greatly boost biomedical applications, such as detecting early diseases and therapeutic interventions. Any single modality typically furnishes only an incomplete picture of the tissue optical response; hence, an approach that integrates complementary optical imaging modalities is needed for a more comprehensive nondestructive and minimally invasive tissue characterization.

#### 5.1.1 Multimodal OCT and Raman

In Raman spectroscopy (RS), monochromatic illumination of a sample can lead to a small fraction of weakly scattered photons, indicating a frequency shift that is directly related to the vibrational or rotational states of the probed molecular bonds. RS is a label-free imaging technique because the signal is purely derived from the vibrational or rotational states probed in the material.<sup>164</sup> A simple sketch of combined OCT/RS is shown in Fig. 8.

The ability to use the structural information of OCT with subsequent RS from two independent modalities to identify early dental caries was demonstrated by Ko et al.<sup>165</sup> Their research showed that the Raman peak sensitivity of enamel is dependent on the Raman sampling arrangement. Further, the obtained Raman spectrum from sound and carious enamel varied with the Raman sampling depth, resulting in difficulties in using RS alone to identify lesions. The additional data obtained from OCT were important for identifying critical related structural changes and depths for the RS, suggesting the usefulness of combining structural and chemical information.

Patil et al.<sup>166,167</sup> demonstrated a combined NIR OCT and Raman system with separate detection channels providing morphological and biochemical information for normal and malignant tissue characterization, including skin cancer. OCT/RS was performed on cancerous skin [basal cell carcinoma (BCC)] and normal skin. OCT alone was capable of indicating hyper-reflective and hypo-reflective features in both; hence, critical reflectivity features cannot be classified as malignant by OCT alone. However, the large morphological scan was used to guide the RS to a region of interest for obtaining biochemical information. A clear differentiation between malignant and normal tissue was achieved by the obtained Raman spectrum, which contained notable differences in specific wavenumber regions. The presence of BCC induced a stronger scattering intensity in the spectral bands associated with proteins ( $1330$  and  $1440\text{ cm}^{-1}$ ) and nucleic acids ( $1090\text{ cm}^{-1}$ ). The increase in the nuclear-to-cytoplasm ratio is often indicated with tumors in histopathology. In conclusion, the OCT/RS system was able to combine imaging

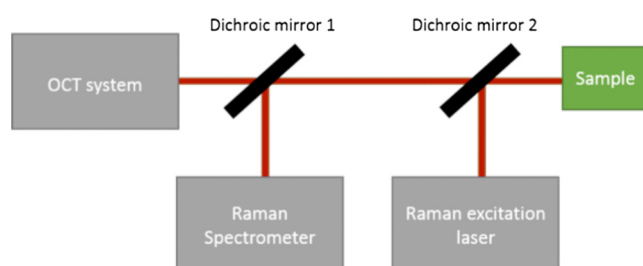


**Fig. 8** Simplified depiction of a combined OCT and Raman system.

and spectroscopy for classification of similar morphological structures found in malignant and healthy tissues. Patil et al.<sup>166</sup> also reported an integrated OCT/RS system using a deep-depleted, back-illuminated, thermo-electrically cooled CCD array as a single detector for both Raman and OCT, respectively.

Simultaneous OCT/RS with *ex vivo* human and porcine retinal samples was demonstrated by Evans et al.<sup>168</sup> The OCT/RS measurements were performed under *in vivo* imaging conditions. To retrieve the Raman signal with an acquisition time of 200 ms, 4 mW was applied on the sample. In contrast, Patil et al.<sup>166</sup> used 40 mW and 5 s, respectively, to obtain the Raman signal. The reduction of the source power and acquisition time implicated an impaired RS signal-to-noise ratio (SNR). To correct for the drop-off in SNR, several Raman spectra from adjacent OCT A-scans were averaged. The simultaneous OCT/RS was able to distinguish the different structures in a polystyrene-polymer phantom, but it was not able to visualize the main retinal layers of the *ex vivo* human and porcine retinal samples due to the low SNR.

Ashok et al.<sup>169</sup> performed a multimodal approach using RS and OCT successively from independent modalities to discriminate malignant colon from normal colon tissue. Their work was based on quantitatively combining the morphological information (OCT) and the biochemical information (RS) to enhance sensitivity and specificity. A texture analysis was performed on OCT data to quantify OCT images to further combine the texture parameters with the chemical information obtained by RS. Principal component analysis was used for both Raman and OCT, respectively, for classification. Table 2 shows the evaluated classification accuracy for each modality, demonstrating the potential of achieving accurate discrimination of malignant or normal tissue by combining both data sets.

All the work mentioned above demonstrated the advantage of combining RS with OCT. However, in each study, the obtained RS was volume integrated from different depths, resulting in an average RS outcome, which can result in difficulties in achieving a more detailed biochemical analysis for a given tissue. Khan et al.<sup>170</sup> demonstrated a combined OCT/RS system capable of layered tissue analysis. Depth-resolved RS was achieved due to a confocal Raman configuration rejecting out-of-focus Raman scattered light. The performance of the OCT/RS system was validated with a paraffin-Acetaminophen phantom and promising results were also obtained on a mucosal tissue sample from goat. Biochemical maps from the epithelium and stroma were retrieved.

### 5.1.2 Multimodal OCT and CARS

CARS is a four-wave mixing (FWM) process where three incident fields (pump photon  $\omega_p$ , Stokes photon  $\omega_s$ , and probe photon) interact with the sample to generate a fourth blueshifted

anti-Stokes field with frequency  $\omega_{as} = \omega_p - \omega_s + \omega_p$ .<sup>171</sup> When the frequency difference of the pump and Stokes photon matches a molecular vibrational resonance  $\Omega = \omega_p - \omega_s$ , the CARS signal is enhanced, making CARS a coherent label-free chemical specific imaging modality.<sup>172</sup>

In molecularly sensitive OCT, CARS was used for nonlinear optical contrast enhancement.<sup>52,173</sup> The contrast enhancement was obtained with a method called NIVI.<sup>48,49</sup> The interferometry setup for molecularly sensitive OCT is based on a conventional OCT setup. However, NIVI differs from conventional linear interferometry. A second wavelength-shifted beam is needed to generate the CARS signal. The experimental setup is shown in Fig. 9.

In Fig. 9 (left), a regenerative amplifier is used to create a pump pulse for the sample arm and to pump the SHG optical parametric amplifier (OPA). The OPA creates two pulses, a Stokes pulse for the sample arm and a coherent anti-Stokes pulse for the reference arm to cause interference with the CARS signal retrieved in the sample arm. Molecularly sensitive OCT imaging of a biological sample was performed from a thin lipid-

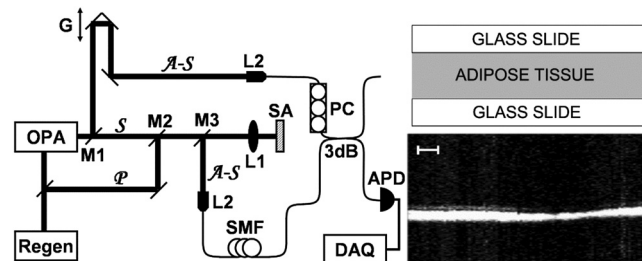


**Fig. 9** Experimental setup. Left: Regen, regenerative amplifier; G, galvanometer-controlled optical delay; M1 to M3, long-pass dichroic mirrors with different cutoffs; P, pump; S, Stokes; A-S, anti-Stokes; L1, 30-mm focal-length lens; SA, sample; L2, 10x microscope objective; SMF, single-mode fiber; PC, polarization controller; APD, avalanche photodiode; DAQ, data acquisition. Right: Coherent anti-Stokes Raman scattering image from lipid resonance at  $2845\text{ cm}^{-1}$  of a thin lipid-dense layer of beef tissue sandwiched between two glass slides.<sup>52</sup>

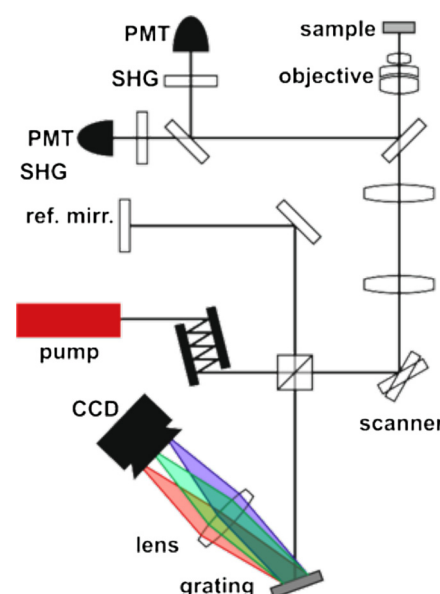


**Fig. 10** Typical combined spectral domain and nonlinear optical microscopy setup.

dense layer of beef tissue sandwiched between two glass slides. The CARS signal was retrieved from a lipid resonance at  $2845\text{ cm}^{-1}$ , as shown in Fig. 9 (right).

### 5.1.3 Multimodal OCT and MPM

There is a great interest in combining MPM with optical coherence microscopy (OCM). A typical schematic of a combined platform is shown in Fig. 10. In OCT and OCM, imaging contrast is due to the difference in refractive index of different tissues. For many applications, changes in the sample linear scattering properties are small and difficult to measure. MPM provides biochemical and metabolism information which is related to nonlinear effects based on the simultaneous interaction of two or more photons within a molecule related to higher order susceptibilities. Hence, multiphoton excited

fluorescence and/or harmonic generation provide molecular contrast and specificity with submicron resolution. The theoretical estimation of the lateral resolution can be derived from the Rayleigh criterion and the axial resolution is referred to as the depth of focus of the illuminating beam. For a high-NA objective, the axial resolution can be estimated as approximately three to four times its lateral resolution. The integration of OCT and MPT in a combined setup allows for depth-resolved high-resolution structural and functional imaging and is demonstrated in many biomedical and clinical applications.

The concept of TPF was first described by Göppert-Mayer<sup>174</sup> in 1931 and first observed after the invention of the laser to achieve the high photon flux density.<sup>175</sup> It is a three-stage process of photon emission by a molecule or fluorophore. The probability of a two-photon absorption occurring

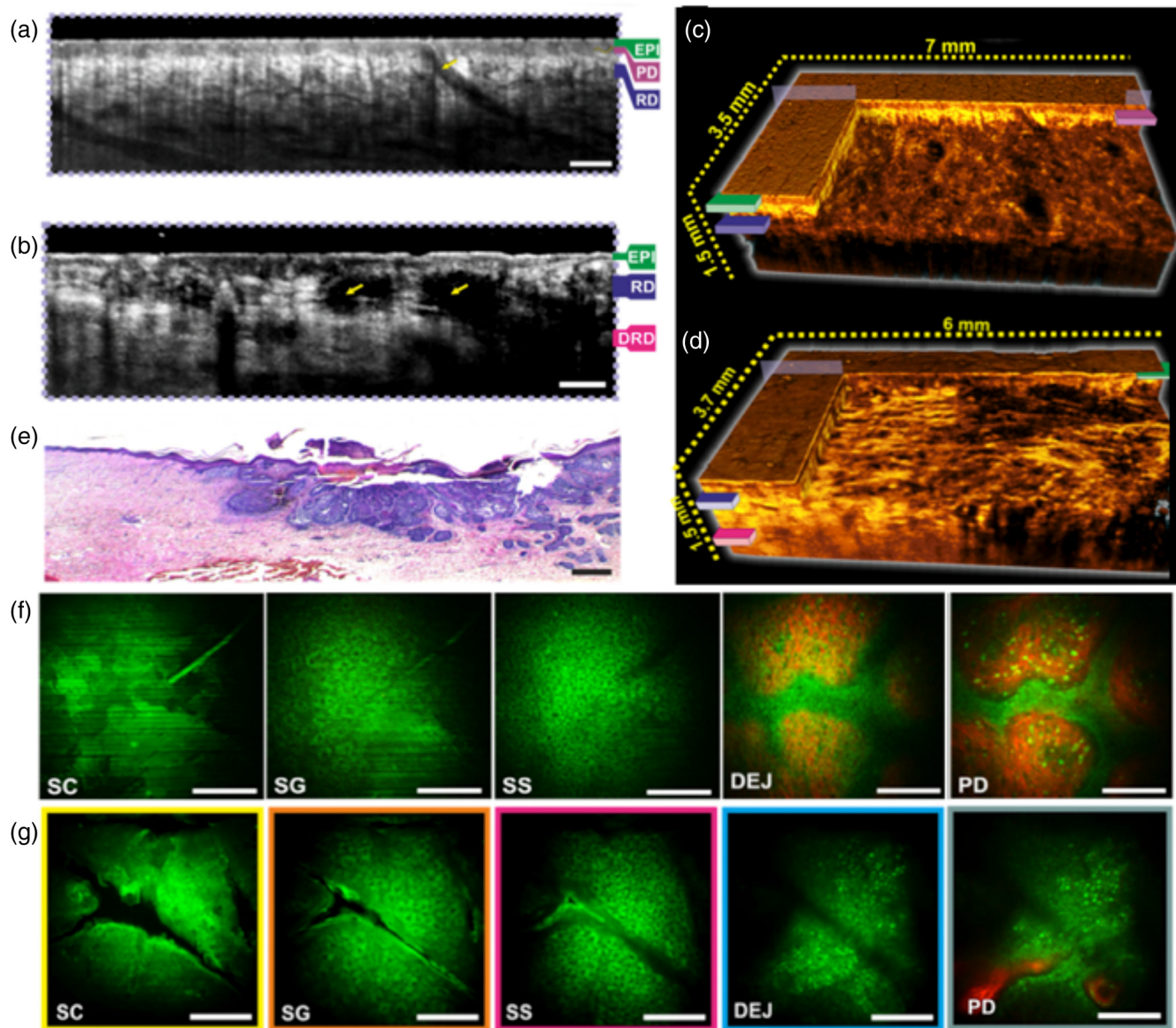


**Fig. 11** *In vivo* clinical MPT/OCT in basal cell carcinoma in the dorsal forearm. (a) and (c) Two-dimensional (2-D) and 3-D OCT of normal skin. (b) and (d) 2-D and 3-D OCT of basal cell carcinoma. (e) Histology of excised basal cell carcinoma after imaging. (f) MPT of normal skin at different depths. (g) MPT of basal cell carcinoma. MPT was acquired in the center of 3-D OCT. SC, stratum corneum; SG, stratum granulosum; SS, stratum spinosum; DEJ, dermalepidermal junction, and PD, papillary dermis.

in a fluorophore is extremely low. Hence, a high photon flux density is required. NIR femtosecond lasers have sufficient peak intensity to enable a high probability for two or three photon excitations raising the fluorescent molecule into an excited state. TPF can be detected from exogenous contrast agents like ICG or green-fluorescent protein (GFP). Label-free two-photon imaging is possible by selecting targeting intrinsic cellular molecules such as NADH and flavins. This approach is usually called two-photon autofluorescence imaging. Features extracted from NAD(P)H and keratin autofluorescence in TPF images have been used to differentiate between normal, precancerous, and cancerous squamous epithelia. The potential of molecular imaging with multiphoton excitation fluorescence was first demonstrated in 1990<sup>160</sup> by the scanning of chromosomes in dividing cells (LLC-PK-1; American Type Culture Collection) stained by cellular DNA labeled with a UV excitable fluorescent stain (Hoechst 33258) and a mode-locked dye laser. Although TPF has enhanced our knowledge on how cells behave within intact tissue environments, it still has limitations inherent to fluorescence microscopy. It can only visualize fluorescing features with the FOV of a few hundred microns. Label-free MPM is also possible via three-photon processes and can be used to image tryptophan and serotonin.<sup>176</sup>

Unlike TPF, SHG is a parametric process which does not involve photon absorption and emission.<sup>161</sup> It only occurs in noncentrosymmetric molecules when the electric field of the excitation light is strong enough. Due to the intense laser pulse, a nonlinear polarization is generated. SHG is the lowest-order nonlinear optical process in which second-order nonlinear optical susceptibility is responsible for the generation of light at the second-harmonic frequency. The quadratic power dependence of SHG on the refractive index provides better optical contrast for imaging tissue structures than conventional linear reflectance microscopy. The first biological SHG imaging experiment dates back to 1986, showing the orientation of collagen fibers in a rat tail tendon.<sup>177</sup> Imaging can be performed with a single widely tunable NIR femtosecond laser. The successful combination of SHG with OCT was first reported in 2004 with an ultrafast Ti:sapphire laser with 110 fs pulse duration.<sup>178</sup> Two collagen layers were sandwiched among glass slides. Since then a vast number of implementations by other groups have been reported.<sup>49,179</sup> Collagen is the most abundant extracellular structural protein of the vertebrate body, making up ~6% of muscle tendons.<sup>180</sup> Collagen, in the form of elongated fibrils, is mainly found in bone, cartilage, skin, blood vessels, tendon, and cornea. Due to its longevity, it constitutes a prominent target of structural modifications usually associated with various physiological processes, such as diabetes, renal diseases, aging, and cancer.<sup>181</sup>

THG occurs even in centrosymmetric structures and can visualize interface heterogeneities as well as myelin sheaths in studies of the nervous system in animal models.<sup>182</sup> Since SHG and THG do not excite coupling of electronic levels, photobleaching can be suppressed, enabling observation of structures over extended periods. Squier et al.<sup>162</sup> demonstrated THG microscopy with dynamic living specimens for the first time in 1998 with a 100 fs excitation pulse at 1.2 μm and 250 kHz repetition rate resulting in a signal at 400 nm arising from the cytoplasmic streaming and statolith movement of the chara plant rhizoids. Both are parameters for the vitality of the plant.

A number of groups have demonstrated a multimodal OCT and nonlinear optical imaging platform with Ti:sapphire lasers

to obtain structural and biochemical information from tissue. Beaurepaire et al.<sup>183</sup> were the first who demonstrated the potential of TD OCM and TPF microscopy with an ultrafast Ti:sapphire laser (Spectra Physics, Santa Clara, California) with a pulse duration of 80 fs and 82 MHz repetition rate. The possibility of coupling functional and structural imaging based on the different contrast mechanisms derived from fluorescence and backscattered light was demonstrated *in vivo* with a drosophila embryo transfected to express GFP in its cell nuclei. Furthermore, the combination of OCT and fluorescence spectroscopy has been reported for diagnosis of carcinoma in esophageal and cervical tissue by Kuranov et al.<sup>184</sup> Pan et al.<sup>185</sup> were the first who reported an experimental study enhancing efficiency and sensitivity of early bladder cancer diagnosis with an aminolevulinic acid hydrochloride (ALA) fluorescence-guided endoscopic OCT for *ex vivo* rat bladder imaging in the rat model. *In vivo* bladder imaging was performed as well.<sup>186</sup> Jiang et al.<sup>178</sup> used a femtosecond laser pulse with 110 fs pulse duration and 76 MHz repetition rate to generate second-harmonic signals from collagen harvested from rat tail tendon sandwiched among glass slides and combined it for the first time with OCT. This technique added contrast and enhanced the resolution of OCT due to the strong dependence of SHG on molecular and tissue structures. In the same year, Yeh et al.<sup>187</sup> combined OCT with a superluminescent diode centered at 1310 nm and MPM with an ultrafast Ti:sapphire laser (150 fs, 800 nm) in two separate systems and compared it with histopathology to monitor laser thermal injury and subsequent wound healing in organotypic, skin-equivalent tissue models. The *in vitro* skin-equivalent rat tissue model was composed of dermis with type I collagen and fibroblast cells and epidermis of differentiated keratinocytes. High-resolution MPM imaging using SHG revealed alterations in collagen microstructure organization with subsequent matrix reconstruction. Fibroblast cell migration in response to injury was monitored by MPM using TPF. Vinegoni et al.<sup>188</sup> reported an integrated microscope that combined SD OCM, TPF, and SHG signals to allow for simultaneous acquisition of structural and functional information based on a single Ti:sapphire laser with a 60-nm bandwidth and 80-MHz pulse repetition rate (Femtolasers, Vienna, Austria). An average sample power between 1 and 10 mW was focused with a 20 × 0.95 MO onto fibroblast cells transfected with GFP-labeled vinculin and stained with a nuclear dye (Hoechst 33342). Also, dynamic cell-scaffold interactions under more physiological 3-D conditions and *in vitro* smooth muscle tissue from a transgenic GFP mouse were studied.

A noninvasive dual-modality imaging system was demonstrated that incorporated OCT and fluorescence lifetime imaging microscopy (FLIM) capable of simultaneously characterizing the 3-D tissue morphology and its biochemical composition into a single optical system for the first time.<sup>189</sup> A spectrometer-based OCT based on a SLD centered at 830 nm provided high-resolution morphological volumetric tissue images with an axial and lateral resolution of 7.3 and 13.4 μm, respectively was combined with a pulsed Q-switched tripled Nd:YAG laser for excitation. The multispectral FLIM based on a direct pulse-recording approach (upon 355 nm laser excitation) provided 2-D superficial maps of the tissue autofluorescence intensity and lifetime at three customizable emission bands with a 100-μm lateral resolution. Both systems shared the same excitation/illumination optical path to facilitate the coregistration of OCT volumes and FLIM images. The

developed OCT/FLIM system was capable of a maximum A-line rate of 59 kHz for OCT and a pixel rate of up to 30 kHz for FLIM and was validated with standard fluorophore solutions and subsequently applied to characterize two biological tissue types: postmortem human coronary atherosclerotic plaques, and *in vivo* normal and cancerous hamster cheek pouch epithelial tissue. Sets of biomarkers in a Syrian hamster cheek pouch model of epithelial cancer were identified. OCT provided morphological information for cancer, including thickening of the epithelial layer and loss of layered structure, and FLIM provided chemical information, including increased nicotinamide adenine dinucleotide and reduced collagen emission, to discriminate benign lesions. Additional lifetime characteristics provided a better quantification of tissue biochemistry, as lifetime measurements can resolve fluorophores with overlapping spectra, such as collagen and NADH. The fluorescence signal was detected with a microchannel plate-PMT and simultaneous multispectral time-resolved fluorescence detection was achieved by separating the fluorescence emission in three bands to selectively quantify the fluorescence emission of collagen ( $390 \pm 20$  nm), NADH ( $452 \pm 22.5$  nm), and flavin adenine dinucleotide (FAD,  $550 \pm 20$  nm).

Multimodal OCT setups were also used to investigate the eye. Dobre et al.<sup>190</sup> developed a dual-channel OCT-ICG fluorescence system based on an ophthalmic OCT confocal imaging system with the confocal channel tuned to the fluorescence wavelength range of ICG. A SLD was implemented to visualize *en face* OCT slices and corresponding ICG angiograms of the ocular fundus simultaneously, demonstrating the potential for a more complete view of the pathologic conditions in ocular diseases.<sup>191</sup> A combined nonlinear optical microscopy and OCM imaging system based on an ultrabroad bandwidth Ti:sapphire laser (sub 10 fs) was used to measure the mechanical and microstructural response of the central cornea from New Zealand white rabbits postmortem.<sup>192</sup> Autofluorescence and SHG imaging were performed to image cornea anatomy in normal and diseased states and to characterize the collagen microstructural response to changes in intraocular pressure. A trimodal microscopy with MPM, OCM, and OCT for multiscale and multicontrast imaging was demonstrated in leaves and fish cornea samples (cf. Fig. 12) by a sliding for rapid scanning over a large area and a high-resolution zoom-in for cellular-level structures on regions of interest.<sup>193</sup> Cross-sectional OCT over millimeter FOV and *en face* high-resolution MPM with submicrometer resolution from the same sample position could be obtained by switching the focusing objective. All layers of a fish cornea were imaged at a frame rate of  $\sim 100$  frames/s with OCT and cells and collagen fibers were visualized at a frame rate of 0.4 frames/s. Dai et al.<sup>194</sup> demonstrated in a proof of principle study with an ultrafast Ti:sapphire laser simultaneous OCT and autofluorescence microscopy to address biomolecules like lipofuscin. *Ex vivo* ocular tissues and a rat retina *in vivo* were successfully imaged. A single 12 fs broadband (100 nm) source (Femtolasers) was used to combine three-channel MPM and OCT in a single platform by Tang et al.<sup>195</sup> The ultrafast Ti:sapphire laser was dispersion compensated to simultaneously provide short pulses necessary for efficient MPM excitation and the broad bandwidth required for high-resolution OCT. MPM and OCT channels were coregistered with a lateral resolution of  $\sim 0.5 \mu\text{m}$  and an axial resolution of  $\sim 1.5 \mu\text{m}$ , showing the potential of providing simultaneous functional and structural information from cells and an extracellular

matrix with a 3-D organotypic epithelial tissue model. SHG revealed information about the cellular and extracellular collagen matrix, the autofluorescence signal added information from the cell body of fibroblasts and OCT visualized the internal structure.

Yazdanfar et al.<sup>196</sup> demonstrated a trimodal microscope for multifunctional imaging of endogenous contrast by combining the functionality of OCM, TPF, and SHG in fluorescent microspheres and *ex vivo* skin tissue. A combined instrument of two imaging modalities to acquire information on the cardiac function in larval *Drosophila melanogaster* was demonstrated.<sup>197</sup> The imaging platform was able to sequentially provide cross-sectional OCT and C-scan laser scanning fluorescence microscopy images with a SLD and a continuous-wave solid-state laser (FDC488, JDSU, Milpitas, California) operating at 488 nm, where the major excitation peak of GFP is located. With this dual-imaging system, the heart could be easily located and visualized within the specimen and the change of the heart shape in a cardiac cycle could be monitored.

Various laser sources were integrated into multimodal MPM and OCT to optimize the performance for such platforms. Since the skin and eye are easily accessible with OCT, many studies were related to the skin or eye. A dual-spectrum laser source based on fiber continuum generation in combination with a widely tunable Ti:sapphire laser was used for *in vivo* OCT and TPM high-resolution tissue imaging to target a broader range of fluorescent markers.<sup>198</sup> Jeong et al.<sup>199</sup> proposed a combined TPF and OCT using individually optimized sources. TPM was performed with a Ti:sapphire laser and provided molecular and cellular information. OCT was performed with a swept source centered at 1300 nm and provided simultaneous large-area screening of simple microsphere specimens to demonstrate the spatial coregistration in the small intestine and ear tissues of mouse models *ex vivo*. König et al.<sup>200</sup> reported the first clinical study with a variety of skin diseases and disorders, such as skin cancer, psoriasis, hemangioma, connective tissue diseases, pigmented lesions, and autoimmune bullous skin diseases. Two different OCT systems were combined with MPT and dermoscopy to provide 2-D color images of the skin surface. A stack of cross-sectional OCT wide-field images with a typical FOV of  $5 \times 2 \text{ mm}^2$  gave fast information on the depth and volume of the lesion. MPT provided  $0.36 \times 0.36 \text{ mm}^2$  horizontal/diagonal optical sections within seconds of a particular region of interest with superior submicron resolution down to tissue depths of  $200 \mu\text{m}$ .<sup>201</sup> The clinical diagnostic potential of this multimodal MPT/OCT system in dermatology had been demonstrated in a further study by acquiring sequential 3-D MPT and OCT images of various dermatological disorders<sup>202</sup> (cf. Fig. 11). Recently, a combined MPT/OCT system capable of simultaneously acquiring high-resolution OCM and MPM was demonstrated in a single platform to enable simultaneous acquisition and coregistration for *in vivo* skin imaging and dynamic imaging of blood flow in capillaries.<sup>203</sup> A widely tunable ultrafast Ti:sapphire laser was used to excite the endogenous proteins NADH and FAD at 760 nm. A part of the Ti:sapphire laser beam was launched into a photonic crystal fiber for high-resolution OCT for structural imaging.<sup>203</sup> Furthermore, *in vivo* 3-D multimodal optical imaging was used to search for evidence of epidermal regeneration by bone marrow (BM)-derived cells during various skin repair processes.<sup>204</sup> *In vivo* imaging was demonstrated for visualizing GFP BM-derived cells in the skin, as well as for detecting collagen in the dermis layer. OCT structural and

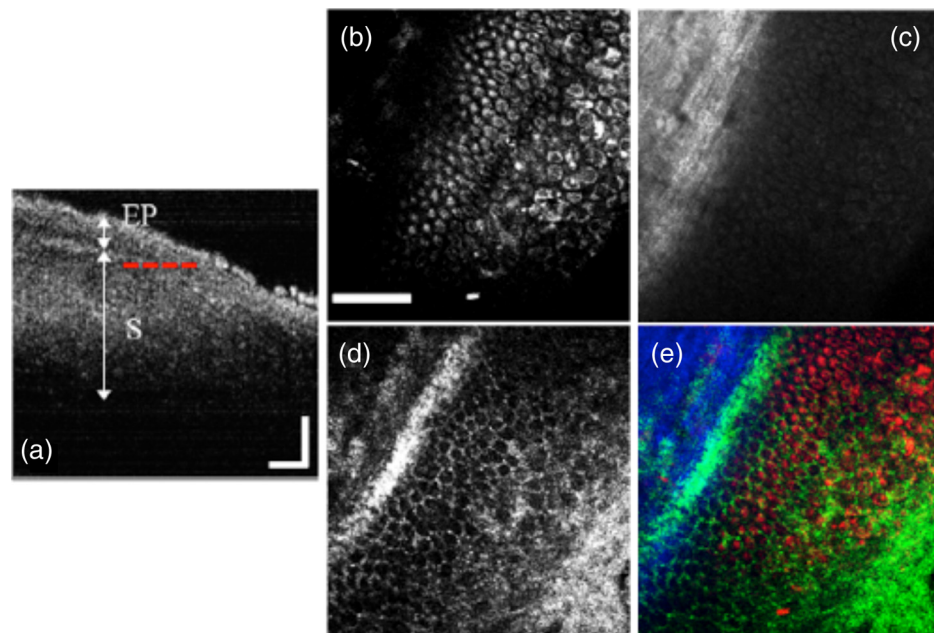


**Fig. 12** OCT, multiphoton microscopy (MPM), and optical coherence microscopy (OCM) images from fish cornea sample. (a) Large field of view (FOV) cross-sectional OCT image where the epithelium (EP) and stroma (S) could be differentiated. Dashed line shows the region where the MPM/OCM is performed. (b) to (d) High-resolution two photon excitation fluorescence (TPF), second harmonic generation (SHG), and OCM images. (e) Overlay of the TPF, SHG, and OCM images with color codes of red, blue, and green, respectively. Scale bars in (a) and (b) represent 100 and 50  $\mu\text{m}$ , respectively. (b) to (e) share the same FOV.<sup>193</sup>

microvascular imaging was demonstrated for assessing the state of skin following wounding and grafting. This study demonstrated the potential of *in vivo* multimodal imaging to contribute to a better understanding of the general mechanisms by which skin regeneration is influenced by BM-derived cells. Since multimodal imaging without an endoscope or fiber delivery probe is mainly limited to cell, skin, and ocular imaging, thorough efforts have been undertaken to integrate an endoscope or build a fiber delivery probe. Pan et al.<sup>185</sup> suggested that an ALA fluorescence-guided endoscopic OCT could enhance the efficiency and sensitivity of early bladder cancer diagnosis and demonstrated in animal studies that the specificity of fluorescence detection of transitional cell carcinoma was significantly enhanced by fluorescence-guided OCT. Tumlinson et al.<sup>205</sup> have demonstrated a combined miniaturized OCT and laser-induced fluorescence (LIF) spectroscopy imaging catheter for *in vivo* mouse colon imaging to monitor the disease progression in mouse colon longitudinally and to identify colorectal adenomatous mouse colon.<sup>206–208</sup> OCT images showed significant changes in mucosal layer thickness and loss of visibility of tissue boundary lines between healthy and diseased tissue. Similarly, the LIF spectra of healthy and diseased tissues were distinguishable by the emissions at 405 and 680 nm. The autofluorescence signal measured by LIF provided biochemical information that was correlated to a dietary metabolite. Coregistered OCT and MPM enabled simultaneous imaging of tissue morphology and molecular information of mouse intestinal tissues at high resolution (10  $\mu\text{m}$ ) over a 2 to 3 mm FOV with the potential for small animal imaging and clinical imaging. A fiber-based multimodal imaging system that combined MPM with FD OCT simultaneously was suggested.<sup>209</sup> It consisted of a fiber laser centered at 1.04  $\mu\text{m}$ , fiber couplers, and a double-clad fiber and

was tested with a thin slice of fixed rabbit heart. OCM and MPM shared the same excitation light path in the core of a double-clad fiber. The OCM signal was collected by the core without significant losses and the MPM by the clad of the double-clad fiber with 20% collection efficiency. Xi et al.<sup>210</sup> reported a compact all-fiber-optic scanning multimodal endomicroscope capable of simultaneous OCT and TPF imaging. Both imaging modalities shared the same miniature fiber-optic scanning endomicroscope consisting of a double-clad fiber for the 1310-nm swept source for *en face* OCT and a 1550-nm light source (passive mode-locked) for TPF. The endomicroscopy system was used to image *in vitro* cell cultures and *ex vivo* tissue with ICG as fluorescence dye (cf. Fig. 13).

Multimodal and multiscale imaging has found widespread biomedical applications and will further advance with improved optical probes. It can be used to increase the understanding of the molecular and functional changes associated with disease progression. TPF, SHG, THG, and CARS can be seamlessly integrated into a single, unified microscopy platform and OCT can easily be added to obtain complementary structural and functional information within tissue samples and cells. The progress of multimodal optical imaging platforms has been facilitated by advances in ultrafast laser technology, high-performance specialized optical filters, and high-sensitivity detectors. Proper coregistration is needed for large-area prescreening with zoom-in function for chemical specific information.

## 5.2 Dual-Modality Optical Coherence Tomography and Photoacoustic Imaging

Having been clinically readily investigated and applied in ophthalmology<sup>211</sup> and intravascular imaging<sup>212</sup> for over a decade,

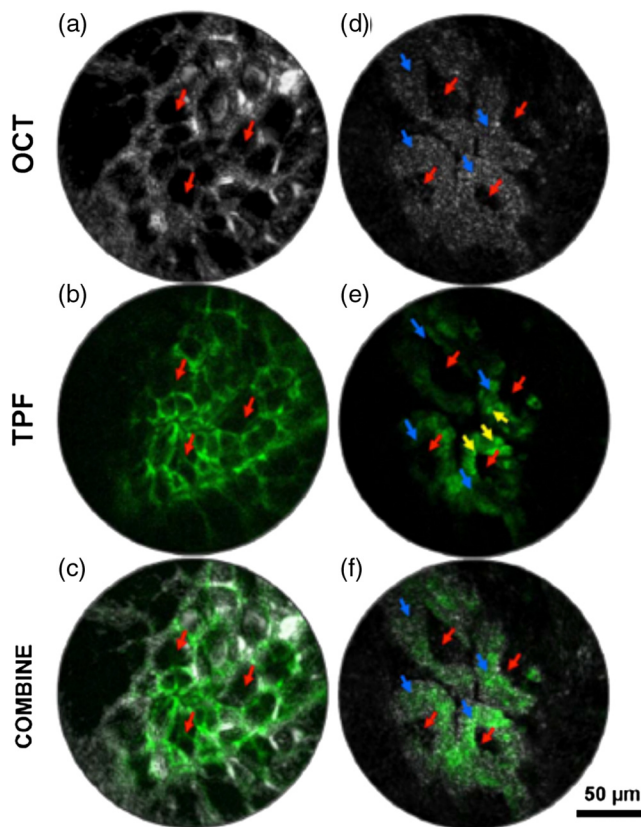


**Fig. 13** (a) OCT, (b) TPF, and (c) superposed images of mouse adipose tissue with local indocyanine green (ICG) administration. Each red arrow in (a) and (b) indicates one of the adipocytes visualized under both imaging modalities. (d) OCT, (e) TPF, and (f) superposed images of mouse small intestine tissue with local ICG administration. Blue arrows (right downward) shown in (d) and (e) indicate villus structures and red arrows (left downward) indicate lacteals. The stronger fluorescence dots indicated by yellow arrows at center shown in (e) may be either enterocytes or lymphocytes. Both sets of images show great correlation between two imaging modalities.<sup>210</sup>

OCT has gained great success, and has become even more successful with the ever increasing imaging speed and finer resolution introduced by new optical sources, which enabled OCT to achieve MHz A-line rate.<sup>213</sup> However, due to the highly scattering nature of biological tissues and the contrast mechanism of OCT, which relies on the difference of tissue scattering

properties, the penetration depth is limited to be within a few millimeters in most cases, even with the 1300-nm sources whose beam gets less scattered than the 800-nm sources.<sup>4</sup> For interconnected soft tissues whose scattering properties are similar, OCT's contrast is also hampered. In order to overcome these disadvantages, efforts have been made to combine OCT with other imaging modalities, such as MPM (Ref. 183) and confocal fluorescence microscopy (CFM),<sup>214</sup> but both MPM and CFM use fluorescence as the contrast mechanism and cannot give OCT any extra imaging depth. Some advanced OCT modalities, such as Doppler OCT<sup>215</sup> and polarization-sensitive OCT (Ref. 216), can generate fluid flow information and bring extra differentiation capability by exploiting the birefringence of biological samples, but the inherent contrast stemming from OCT and the imaging depth limit set by the scattering tissues are yet to be breached.

Compared to the well-developed and mature optical imaging modality OCT, photoacoustic imaging is a relatively novel imaging modality that has attracted much research interest in the past decade. Photoacoustic imaging uses the photoacoustic effect—a certain chromophore absorbs a short laser pulse's energy; this absorbed energy is partially converted to heat; then under thermoelastic expansion, the heat is further converted to a local pressure rise and, hence, an acoustic wave—the photoacoustic wave; by detecting the laser pulse-induced photoacoustic waves, one can reconstruct in 3-D the chromophore distribution in the illuminated volume.<sup>217</sup> Different from OCT that detects backscattered light, photoacoustic imaging detects acoustic waves. Since the photoacoustic waves are inherently broadband, detection of different bandwidths of the photoacoustic wave can generate a variety of different imaging depths ranging from several hundred micrometers by submicron-resolution PAM (Ref. 218) to the centimeter level in whole-body illumination PAT with a resolution of ~100  $\mu\text{m}$ .<sup>219</sup> A table comparing OCT and photoacoustic imaging is given below in Table 3 for a brief comparison of some important features of these two modalities.

From Table 3 we can see that OCT and photoacoustic imaging systems have distinctive but complementary contrast mechanisms. While most PAM imaging systems have imaging depth comparable with that of OCT, PAT systems can image beyond the optical diffusion regime. In optical-resolution PAM (OR-PAM),<sup>220</sup> the lateral resolution is determined by the focal spot size of the excitation laser beam, therefore, it is comparable to that of OCT. The complementary information of these two modalities makes it interesting to compare the results for the

**Table 3** Comparison of OCT and photoacoustic imaging.

	OCT	Photoacoustic imaging
<b>Contrast mechanism</b>	Difference in tissues' optical scattering properties	Difference in tissues' optical absorption properties
<b>Imaging depth</b>	~2 mm	~0.42 to >10 mm depends on implementation
<b>Lateral resolution</b>	Diffraction limited, generally within a few tens of micrometers	from ~0.5 to >100 $\mu\text{m}$ depends on implementation
<b>Axial resolution</b>	Determined by laser source, generally within 10 $\mu\text{m}$	Determined by the detected photoacoustic wave bandwidth, generally several tens of micrometers
<b>Imaging speed</b>	Video rate	Generally slow due to either transducer raster scanning speed or excitation laser pulse repetition rate

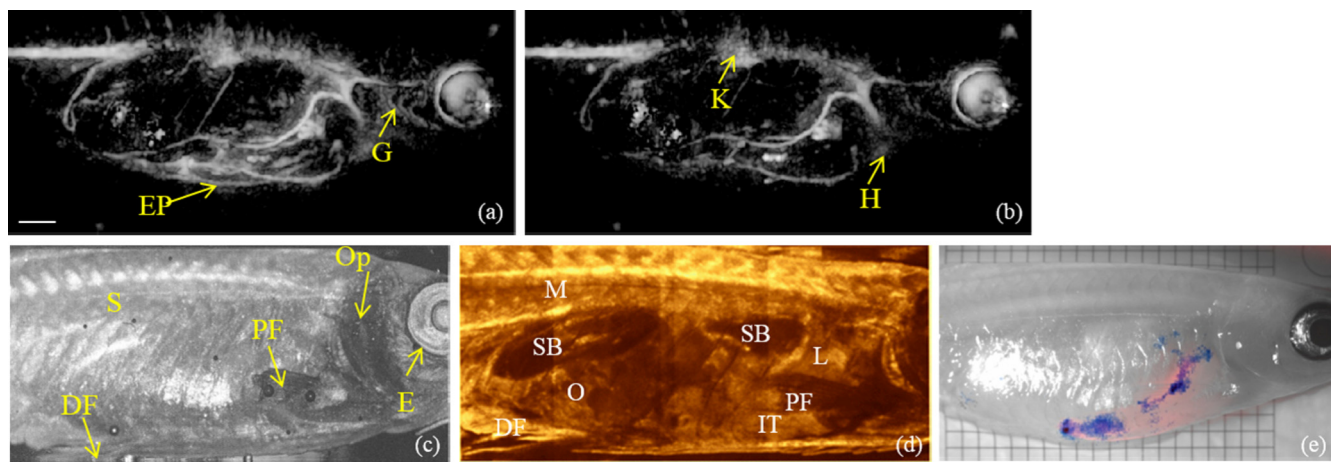


**Fig. 14** (a) and (b) are photoacoustic tomography maximum intensity projection (MIP) images of a zebrafish expressing E2-Crimson in its exocrine pancreas imaged at 611 nm and 640 nm, respectively; (c) and (d) are OCT MIP and B-scan images of the same fish, respectively; (e) is an epifluorescence image showing the E2-Crimson labeled exocrine pancreas (red) overlaid with the E2-Crimson distribution calculated from photoacoustic images. G: gills; EP: exocrine pancreas; K: kidney; H: heart; S: spine; DF: dorsal fin; PF: pectoral fin; OP: opercular; E: eye; M: muscle; SB: swim bladder; O: oocyte; L: liver; IT: intestinal tracts.<sup>222,223</sup>

same sample imaged by these two methods. Multiple studies have employed these two techniques for the same object using separate OCT and photoacoustic imaging systems, such as the study of chemically induced bovine cartilage osteoarthritis where OCT provides the general structural background and OR-PAM shows the locations of clefts and fissures in the cartilage due to osteoarthritis,<sup>221</sup> or the zebrafish exocrine pancreas imaging where an FD OCT system gives the morphological background of the adult zebrafish, while PAT resolves the fluorescent protein (FP) labeled exocrine pancreas and the blood vessels<sup>222</sup> (cf. Fig. 14), or the clinical test of port wine stain (PWS) depth by using OCT to measure the epidermal thickness and using photoacoustic imaging to test the epidermal-to-PWS distance.<sup>224</sup>

All these reports justify the benefits of combining these two imaging modalities together. This section reviews the various implementations of dual-modality OCT/photoacoustic imaging system designs, their characteristics, and their applications in biomedical studies, as well as the technical challenges of the dual-modality systems and their potential applications.

### 5.2.1 Implementations of dual-modality OCT/photoacoustic imaging system

Due to the various submodalities of OCT and photoacoustic imaging, different implementations of OCT/photoacoustic imaging systems have been tested and published. In this section, three major categories are reviewed, namely OCT/photoacoustic endoscopy, OCT/PAM, and OCT/PAT, each having unique features and applications.

**Combined OCT/photoacoustic endoscopy.** Driven by the increasing need for internal body imaging, OCT endoscopes were introduced in the 1990s and demonstrated their feasibility in inner cavity imaging.<sup>225</sup> This specific type of OCT has since undergone a series of improvements in terms of miniaturization, imaging speed, and safety. Compared to OCT endoscopy, photoacoustic endoscopy has suffered a prolonged development phase due to the technical challenges of the comparatively thick multimode fiber's flexibility<sup>226</sup> as well as the detection of

photoacoustic waves by miniaturized probes. Real *in vivo* photoacoustic endoscopy imaging was accomplished only recently.<sup>227</sup> Despite these challenges, a few designs of combined OCT/photoacoustic endoscopes have been tested, as are shown in Figs. 15 and 16. One major difference between the two designs is how the excitation light for photoacoustics and the OCT sample beam are delivered to the sample. In Fig. 15, we can see that the excitations for photoacoustic imaging and the OCT sample arm are delivered by separate fibers while an ultrasound transducer takes additional space in the probe design.

This design makes the outer diameter of the endoscope 5 mm. Compared to the design shown in Fig. 15, Fig. 16 uses a combined OCT/photoacoustics probe, of which OCT and photoacoustic imaging share the same light delivery fiber to the sample. The use of a gradient index (GRIN) lens and a prism pair enables the ultrasound transducer to be mounted right on top of the prism pair and reduces the probe diameter to 2.3 mm.

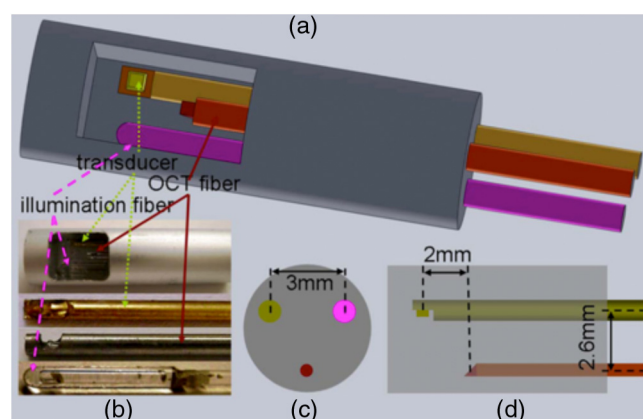


**Fig. 15** Design of a combined miniaturized OCT/photoacoustic endoscope head. (a) Sketch of the general design. (b) Photograph of the OCT fiber, photoacoustic illumination fiber, and the transducer, respectively. (c) Relative placement of the probe. (d) Side view of the probe head.<sup>228</sup>

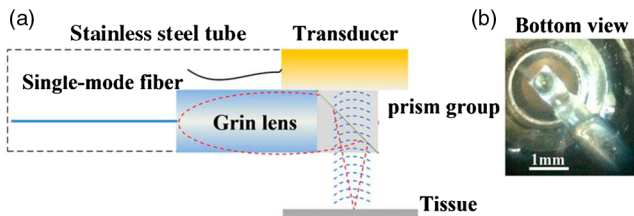


**Fig. 16** An OCT/photoacoustic probe design employing a single fiber. (a) Schematic of the design (red dashed line: photoacoustic excitation beam; blue dashed line: photoacoustic wave). (b) Photograph of the bottom view of the probe.<sup>233</sup>

With a few to several hundred micrometer lateral resolution of the photoacoustic part achieved from the design in Fig. 15 and an SNR of 25 dB for the photoacoustic part in Fig. 16, along with a mechanically scanned stepper motor for 2-D and 3-D imaging, these two dual-modality OCT/photoacoustics miniaturized probes are tested by imaging ovarian tissue and mouse ear, respectively. However, the imaging speed is quite limited by the use of a stepper motor. Unlike the circumferential cavity images quite often seen from OCT endoscopic studies, these two studies gave only traditional B-mode images. The imaging speed, sensitivity, and, hence, application are quite limited for these preliminary prototypes.

**Combined OCT/PAM.** Several different implementations of OCT/PAM dual-modality imaging system have been introduced since 2009, including an SD OCT system combined with a transmission mode OR-PAM system,<sup>229</sup> an SD OCT system combined with a laser scanning optical resolution PAM (LSOR-PAM) system,<sup>230</sup> and a dual-modality system in which OCT and PAM use the same NIR supercontinuum laser source<sup>231</sup> or the same visible laser source.<sup>232</sup> Two representative designs are given in Figs. 17(a) and 17(b).

The resolutions of the system in Fig. 17(a) for OCT are 20  $\mu\text{m}$  laterally and 6  $\mu\text{m}$  axially, while those of the LSOR-PAM are 2.8 and 23  $\mu\text{m}$ .

Using a laser source with a much wider bandwidth and proper focusing, the OCT resolutions in Fig. 17(b) reach 5  $\mu\text{m}$  laterally and 5.9  $\mu\text{m}$  axially. A 75 MHz central frequency ultrasound transducer in the second generation (G2) OR-PAM system shown in Fig. 17(b) was able to achieve a lateral resolution of 5  $\mu\text{m}$ , the same as that of the OCT system combined with it, and an axial resolution of 14  $\mu\text{m}$ . The use of a pair of scanning mirrors to direct the PAM excitation beam, which is given in the schematic of Fig. 17(a), enables this system to perform fast scanning over a sample. This is compared to the design in Fig. 17(b) that uses linear stage for scanning a better choice in regard of imaging speed. However, the G2 OR-PAM design in Fig. 17(b) uses a rhomboid prism and an acoustic lens to maximize the sensitivity,<sup>220</sup> and the FOV can also be much larger than that of Fig. 17(a).

The OCT/PAM systems, represented by the designs shown in Fig. 17, have been applied in *in vivo* studies, such as the metabolic rate of oxygen in mouse ear,<sup>234</sup> the neovascularization in 3-D porous scaffolds,<sup>235</sup> epilepsy mapping with high temporal and spatial resolutions and dual optical contrasts,<sup>236</sup> and retinal imaging in rats.<sup>237</sup> Results of the OCT/PAM imaging of the neovascularization in mouse ear is given in Fig. 18 as an example.

The OCT/PAM systems can well demonstrate the advantages of the dual-modality imaging system by the comparable resolutions of OCT and OR-PAM, the similar imaging depth of 1 to 2 mm, and the complementary optical imaging contrast. With the help of a spectroscopic PAM system, which is capable of extracting the concentration of a certain absorber<sup>238</sup> and the fluid flow rate that can be calculated by Doppler OCT,<sup>234</sup> OCT/PAM systems can be used not only in morphological and angiogenesis studies, but also in functional and dynamic biological studies.

**Combined OCT/PAT.** As is reviewed in the previous section, OCT/PAM generally cannot exploit the depth advantage of photoacoustic imaging. Also, LSOR-PAM has the inherent problem of a very limited FOV within only several square millimeters, and G2 OR-PAM is limited in imaging speed by the

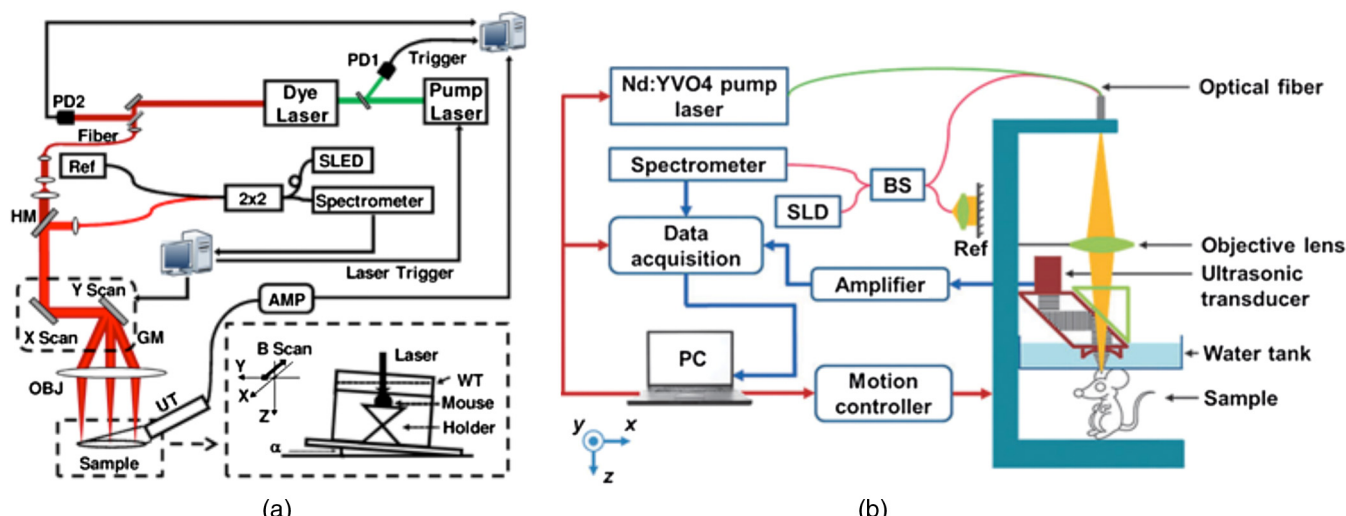


**Fig. 17** Representative designs of the OCT/PAM system. (a) combines a spectral domain (SD) OCT system with a laser scanning optical resolution PAM system. The sample is placed in a tilted water tank for DOCT measurement.<sup>234</sup> (b) employs a second generation optical resolution PAM (OR-PAM) system with an SD OCT system.<sup>235</sup> PD, photodiode; SLED, superluminescent emitting diode; WT, water tank; UT, ultrasound transducer; OBJ, objective; GM, galvanometer scanning mirrors; HM, hot mirror; Ref, OCT reference arm; SLD, superluminescent diode; BS, beam splitter.

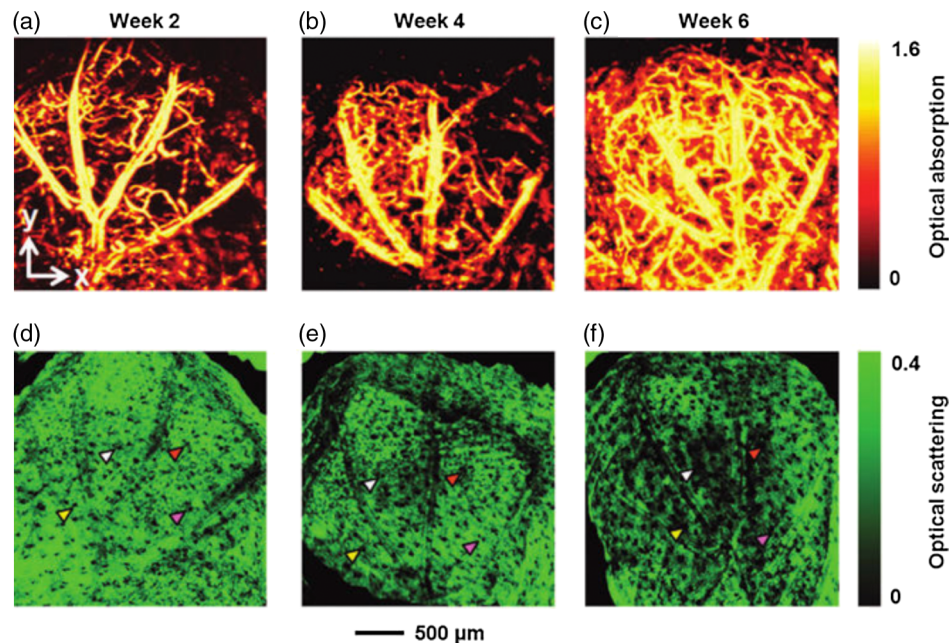


**Fig. 18** Maximum amplitude projection (MAP) images of OR-PAM [(a) to (c)] and OCT [(d) to (f)] showing chronic vasculature and scaffold/tissue construct. The scaffolds can be seen in the OCT images clearly while the blood vessels stand out of the background in the PAM images. The arrowheads indicate scaffold degradation caused pore size increase.<sup>235</sup>

slow mechanical scanning. Although fast B-mode scanning is made possible by using a voice coil for OR-PAM (Ref. 239) and is applicable in a combined OCT/PAM system, it only enables fast scanning in a certain frame. To fully use the beyond optical mean free path feature of photoacoustic imaging, and to enable a large FOV with coregistered OCT/photoacoustics dual-modality imaging, an OCT/PAT system was introduced and tested *in vivo*.<sup>240</sup>

Since this report, the system has been further developed and an SS OCT system with higher bandwidth has been incorporated with the optical detection whole-body illumination PAT system. The newest design of the system is given in Fig. 19. The working mechanism of the optical detection PAT system can be found in Ref. 222. In brief, a multimode fiber (green line in Fig. 19) delivers the excitation pulse to illuminate the whole sample sitting on top of the Fabry-Perot interferometer (FPI) sensor, where distilled water is used as the acoustic couplant. The interrogation beam from the telecom wavelength continuous wave laser probes the FPI sensor in a point-by-point manner and detects the acoustically modulated reflectivity change. This detected modulation linearly correlates to the intensity of the photoacoustic waves, and by using 3-D PAT reconstruction algorithms,<sup>241</sup> the absorber distribution can be mapped in 3-D. For the SS OCT system, a dual-balanced detector (DBD1) is used to compensate for the jitter of the swept source, while DBD2 can extract the interferogram for further postprocessing and image reconstruction. Both systems are controlled by homemade LabVIEW control applications.

This OCT/PAT system has an FOV that is limited only by the size of the FPI sensor, which, in this case, is 3 cm × 5 cm. The sensitivity of the SS OCT part of the system achieves 95 dB. While the imaging depth of SS OCT does not go beyond a few millimeters, the PAT part gives an effective penetration depth of >5 mm in soft tissue. Though sub-100 μm resolution

is achievable both axially and laterally for the PAT part, due to the low repetition rate of the optical parametric oscillator (OPO) used in our system (50 Hz), a scan step size of 100 μm is generally applied to reduce the imaging time. Since the imaging time is two orders of magnitude different between the two modalities, the OCT/PAT system runs in a sequential order. The results of *in vivo* human palm imaging using an OCT/PAT system are given in Fig. 20. From the human palm imaging results, we can see that the vasculature is very well resolved by PAT, including detailed branching information. At the same time, OCT shows the stratum information of skin and the layers in the skin can be distinguished from the OCT B-mode image. The *en face* projection images and the 3-D volume renderings of the fused OCT/PAT images perfectly demonstrate the dual optical contrast and complementary information feature of OCT/PAT. They also illustrate the large scanning area easily achievable by using the optical detection mechanism for photoacoustic imaging.

### 5.2.2 Challenges of OCT/photoacoustic imaging

Having drawn research interests over the past few years, combining OCT and photoacoustic imaging still has some challenges to overcome. The very first one is the imaging speed mismatch. In order to perform real-time functional studies of dynamic biological processes, and also to reduce motion artifact, imaging speed is very critical. OCT, with faster swept sources coming to the market and newer wavelengths being introduced, has no problem when combined with photoacoustic imaging to reach video rate over a large scanning area. However, mechanical scanning of the probe head or the fast scanning available only in single slices for the photoacoustic imaging drags down the imaging speed of the combined dual-modality system. Although LSOR-PAM claims fast scanning speed, the effective FOV is very limited. The obliquely positioned

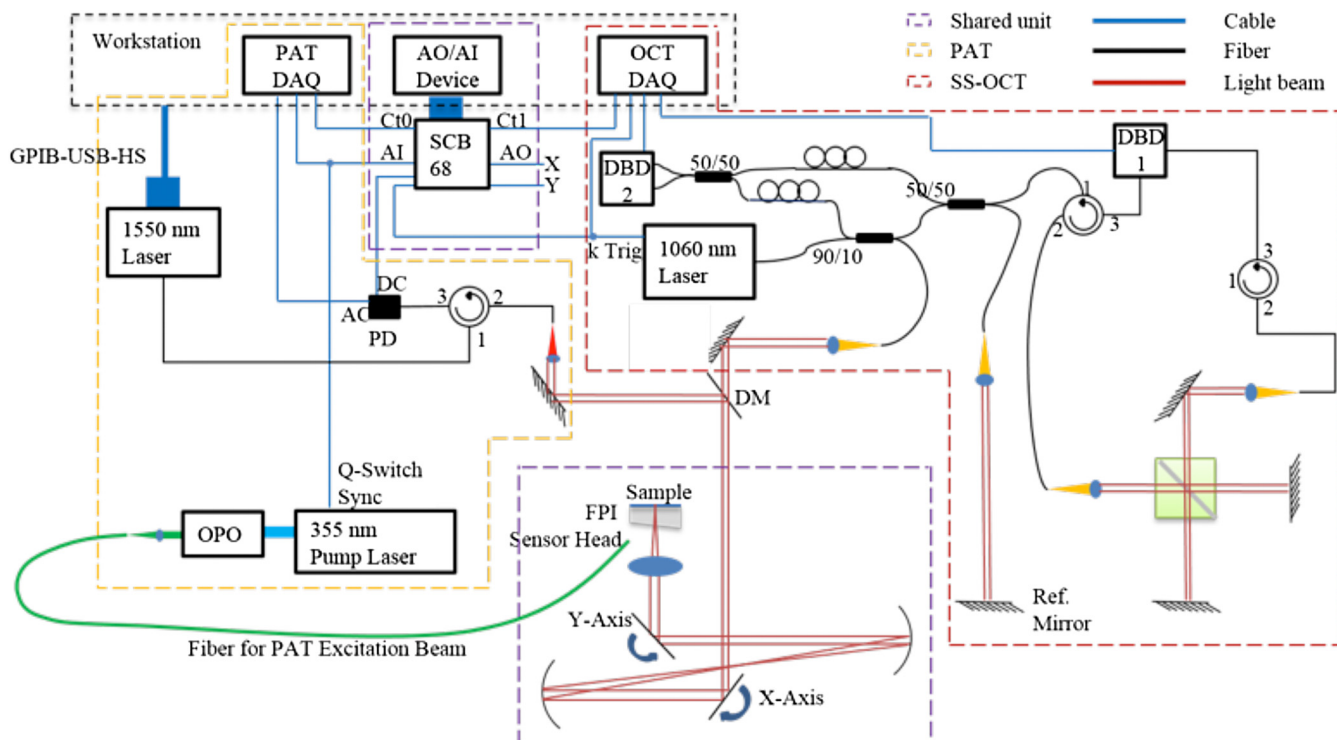


**Fig. 19** Schematic of the OCT/PAT system. An optical detection PAT system using an Nd:YAG pumped OPO as the whole-body illuminating source is combined with an SS OCT system featuring a 1060-nm swept source with 100 nm bandwidth and 100 kHz sweep rate. Data acquisition of the two systems is performed with individual data acquisition devices (DAQ) and is synchronized with the scanning of the 2-D galvanometer scanning mirrors with the AO/AI devices. Both the OCT part and the PAT part share the same scanning unit with the sample sitting on top of the Fabry-Perot polymer film sensor for coregistered imaging. AO, analog output; AI, analog input; OPO, optical parametric oscillator; FPI, Fabry-Perot interferometer; Ref., reference arm; DBD, dual-balanced detector; PD, photodiode; Ct, counter; DM, dichroic mirror.<sup>223</sup>

unfocused ultrasound transducer further reduces the sensitivity of the photoacoustic part when combined with OCT. Though 2-D fast scanning, using a focusing transducer in its focal spot in the reflection mode OR-PAM has been reported<sup>242</sup> and the small focal spot can be mosaicked to form a larger FOV.<sup>243</sup> It has to use a comparatively low-bandwidth ultrasound transducer for its relatively larger focal spot size, which in turn reduces the achievable axial resolution dramatically that is acoustically determined. Also, the nonuniform piezoelectric response of the low-bandwidth transducers to the photoacoustic sources in their focal spots makes it difficult to normalize the signals acquired in the FOV and, hence, is problematic in spectroscopic applications, where it is necessary to extract chromophore concentrations in photoacoustic imaging. The OCT/PAT system suffers the same imaging speed issue due to the low repetition rate of OPO with only 50 Hz currently. Therefore, OCT/photoacoustic imaging systems with the features of real time and large FOV can be a future direction. The second challenge could be the combination of different submodalities of OCT with photoacoustic imaging. Currently, TD OCT, SD OCT, and SS OCT have been tested to combine with different photoacoustic systems. One study already showed the benefit of using Doppler OCT with PAM for the metabolic rate of oxygen measurement.<sup>234</sup> But in their system, the water tank has to be tilted for the flow rate measurement. Newer three-beam Doppler OCT,<sup>244</sup> if it can be combined with PAM, will make the measurement of flow rate easier without *a priori* knowledge.

Polarization-sensitive OCT combined with PAM or PAT is also of special interest due to the extra contrast that can be retrieved by polarization-sensitive OCT. If the detection of the optical detection whole-body illumination PAT system can be parallelized, meaning a line's or a field's photoacoustic waves can be detected simultaneously, then combining line-field OCT or full-field OCT or OCM with PAT will revolutionize the imaging speed and enable simultaneous functional OCT/photoacoustic imaging.

### 5.2.3 Outlook of OCT/photoacoustic imaging

As a hybrid imaging modality, OCT/photoacoustic imaging brings the benefits of OCT and photoacoustic imaging together. Although facing a few technical challenges, the application of OCT/photoacoustic imaging, from endoscopy to whole-body tomography, still has a lot to explore. Not only would it be potentially powerful in all the biomedical, preclinical, and clinical fields where OCT and photoacoustic imaging have been investigated, knowing that OCT has already been reported for biometric identification studies,<sup>245</sup> OCT/photoacoustic imaging may also be used in biometric applications. In summary, in light of the new laser sources, new detection methods, and new applications, OCT/photoacoustic dual-modality imaging is highly expected to get more and more research and application interests in the years to come.

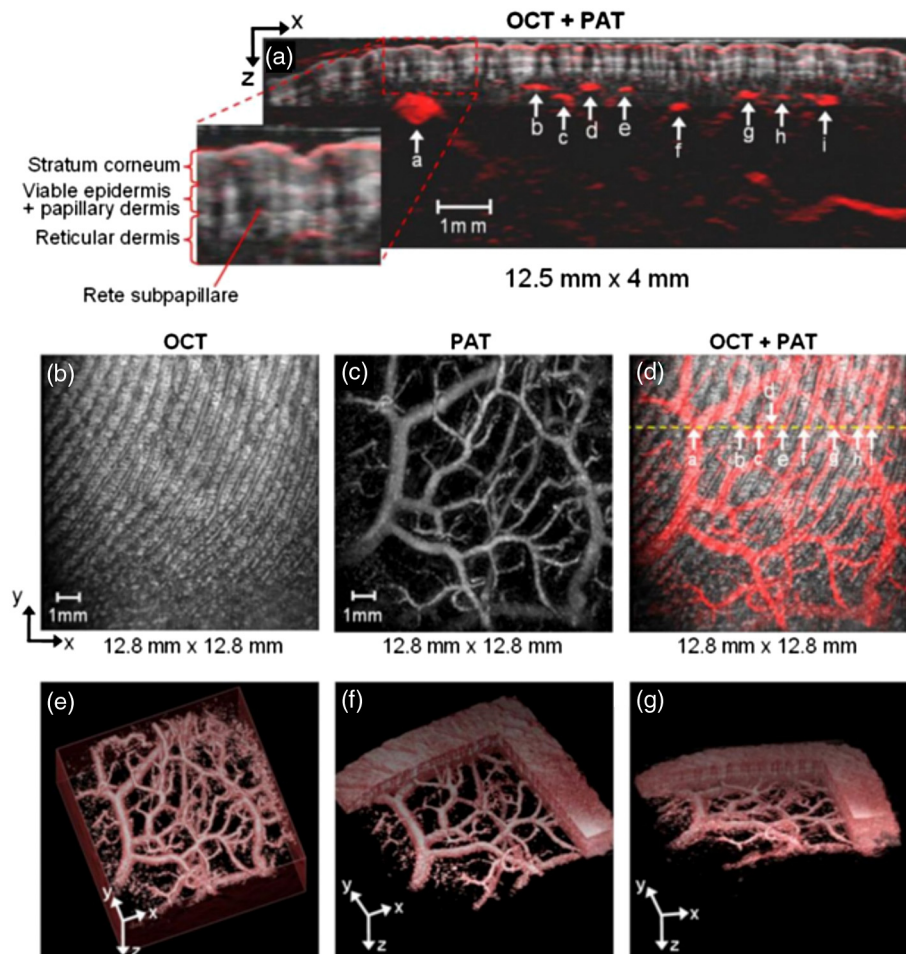


**Fig. 20** Human palm imaging using OCT/PAT. (a) B-mode image where OCT differentiates the layered structures of the skin while PAT shows the blood vessels beneath. (b) *En face* OCT MAP image in which the ridges of the skin can be clearly seen. (c) PAT MAP image giving the distributions of the blood vessels over a depth range of 5 mm. (d) fuses (b) and (c). (e) to (g) 3-D representations of the imaged palm.<sup>240</sup>

## 6 Summary and Outlook

Although ultrahigh (axial and isotropic) resolution and ultrahigh speed for OCT have been demonstrated on a research level, there is still some time to wait for their commercialization—especially for the latter one. Particularly for the wavelength region above 1  $\mu\text{m}$ , it seems that SS technology has significant potential for enabling OCT imaging speeds beyond 400 kHz—up to 1 MHz. Therefore, seven different state-of-the-art SS technologies have been reviewed in this article. A recently developed akinetic, all-electronic swept source promises the highest flexibility and unprecedented performance among its peers along with the features of being cost-effective and compact. The optically pumped VCSEL-based swept source offers by far the longest coherence length and fastest sweep range of commercial sources. To make it commercially attractive, though, electrically pumped VCSELs with identical specifications as the optically pumped ones are a necessity. FDML technology is unique for ultrahigh speed and high optical output power OCT research applications—its widespread commercialization is still unclear at this point in time. There is, at the moment, only one company offering MEMS-based swept sources in five wavelength regions with very competitive specifications. Parallelization of OCT detection based on LF and FF

OCT—preferably swept source based—or digital holography might increase OCT scanning speed even further in an efficient, quasi-akinetic (scanning free) manner. Camera technology (line and area), especially in the wavelength region above 1  $\mu\text{m}$ , has to improve (especially in terms of speed and noise by maintaining sufficient pixels) and become more cost-effective to commercialize these technologies, though.

Although numerous functional and contrast-enhanced extensions of OCT have been developed, they have had limited clinical impact so far as compared to pure morphological OCT systems. This is related to the fact that functional tissue information is inherently more challenging to quantify and reproduce. One recently emerging, contrast-enhancing technique—also referred to as phase variance, speckle correlation based label-free optical coherence angiography—has great potential for providing additional specific diagnostic information. Already highly established in ophthalmology, this technique is being extensively investigated, at the moment, in other clinical applications, such as in dermatology, neurology, and cancer research, in general.

Multiscale, multiresolution imaging promises to be the future of biomedical and clinical diagnosis, enabling multiscale 3-D morphologic and functional imaging at different resolutions

in order to accomplish morphofunctional performance, i.e., the fusion of anatomic and functional imaging at the cellular or even molecular resolution level. Optical imaging, on the other hand, has the potential to enable low-cost, noninvasive, accurate, rapid alternatives in order to address global medical needs, addressing noninvasively to minimally invasive optical imaging from molecular to (sub)cellular to individual organs enabling point-of-care diagnosis. Having already gained broad acceptance in ophthalmic diagnosis, OCT is being comprehensively investigated in other clinical fields, too, such as in cardiology, dermatology, and gastrointestinal as well as oncologic imaging, in general. However, despite the various efforts to improve OCT's performances, its scattering-based contrast mechanism has limited OCT in certain respects, e.g., visualization of subcellular tissue morphology and extraction of biochemical and, in general, molecular tissue information due to its lack of sensitivity to absorption. Therefore, incorporating OCT with other imaging modalities into a hybrid platform has become a hot topic in optical imaging with the ultimate challenging goal to provide easy-to-use, cost-effective optical technologies with higher sensitivity and specificity and to enable a step-change in diagnostics for a range of diseases. Among them, hybrid OCT/MPT, OCT/nonlinear microscopy/spectroscopy, and OCT/photoacoustic imaging are under vigorous investigation, with each of them bearing unique complementary features and potential applications. Unfortunately—especially for nonlinear optical microscopy and photoacoustic imaging—light sources are still based on expensive, large footprint, not extremely reliable (as compared to OCT light sources) technology that can mainly be used and maintained by high-level specialists. Hence, core photonics technology for optical imaging still has to be developed focusing on a reduction in size, reliability, ease-of-operation, and cost-effectiveness as well as the capability to supply more than one imaging modality. Cost reduction would facilitate widespread application throughout the healthcare system, thereby enabling earlier diagnosis, which, in turn, means earlier treatment in the disease process and an improved prognosis.

Other application-oriented hurdles that have to be overcome with multimodal OCT imaging include the inherent limitation of (nonlinear optical) microscopic techniques suffering from small FOVs providing only tunnel vision—in terms of clinical diagnosis. In addition to time-intensive postprocessing-based mosaicking and stitching of smaller FOVs resulting in a sufficiently large one, prescreening with macroscopic techniques (OCT) over a large FOV with subsequent zooming in at the subcellular/biochemical (with, e.g., MPM) or even label-free molecular-level nonlinear optical microscopy (Raman, CARS, or stimulated Raman scattering) on the suspicious areas seems to be a clinically viable way. The clinical impact of nonlinear optical microscopy is still under scientific investigation, although dermatologic and, recently, endoscopic diagnosis, lipid detection for cancer diagnosis, pharmacokinetic applications, as well as improved detection of tumor borders show significant clinical promise.

Hybrid photoacoustic imaging and OCT are an exquisite example of combining two modalities with complementary, synergistic visualization performances: OCT being based on scattering depicts tissue morphology and photoacoustic imaging being sensitive to absorption reveals endogenous or exogenous chromophore-based contrast. In addition, the latter one offers the ability to quantify chromophore concentrations, e.g., oxy-

and deoxy-hemoglobin and, therefore, oxygenation or melanin concentration. Hence, oncologic applications investigating angiogenetic factors as well as a better understanding of tumorigenesis seem to be promising applications.

Combining OCT with complementary optical imaging modalities offers higher sensitivity with modalities enabling high specificity (best of both worlds) and, therefore, fulfilling diagnostic requirements. Furthermore, critical parameters (imaging speed, penetration depth, resolution, as well as biochemical/molecular sensitivity) are significantly improved, which is essential for the successful introduction of a new diagnostic standard.

## **Appendix Basic Terminologies and Key Performance Parameters in Optical Coherence Tomography**

Optical coherence tomography (OCT) systems are usually based on the Michelson interferometer. The light from the source is split by a beam splitter into the sample and the reference arm. The interference of the backreflected light from the sample and the reference mirror is then captured by a detector. OCT systems can be broadly classified as follows (Fig. 21).

### **A1 Time Domain OCT**

In this case, a broadband light source is used. Due to the low coherence of the light source, the interference signal is obtained only when the optical path length of the sample and reference arm is matched to within the narrow coherence length. The reference arm is then scanned to match the optical path length of the reflections from within the sample. The recorded interference signal at different depths or relative time delays between reference and sample is then demodulated to generate a reflectivity depth profile or A-scan.

### **A2 Fourier Domain OCT**

In this case, the spectrum of the interference signal is detected. Fourier domain (FD) OCT can be further classified as spectrometer based and swept source (SS) based. In the case of a spectrometer-based system, a broadband light source is used and the interference signal is split into different optical frequencies using a diffraction grating and detected by a one-dimensional (1-D) CCD array as shown in Fig. 21, whereas in case of a swept source-based system, the interference signal is detected by a photo diode as the spectrum of the light source is scanned with a narrow instantaneous line width in time. The detected intensity spectrum is then Fourier transformed to obtain the depth-resolved reflectivity profile (A-scan) of the sample as shown in Fig. 21.

The key technological parameters associated with the OCT are described briefly below.

#### **A2.1 Axial/Longitudinal Resolution**

In OCT, the axial resolution depends on the coherence length of the light source. The coherence length is the spatial width of the field autocorrelation measured by the interferometer. Since the light travels twice the distance to a given sample arm interface, OCT axial resolution is given by the round trip coherence length, which is half the standard coherence length. The envelope of the field correlation is equivalent to the Fourier transform of the power spectrum. The axial resolution is, therefore, inversely proportional to the spectral bandwidth of the light source as  $\Delta z = 2 \ln(2)\lambda_o^2 / (\pi\Delta\lambda)$ , where  $\Delta\lambda$  is the FWHM bandwidth

and  $\lambda_o$  is the center wavelength of the light source (assuming a Gaussian spectrum, refer to Fig. 21).

## A2.2 Lateral/Transverse Resolution

Lateral resolution in OCT is independent of the bandwidth of the light source and, hence, independent of the axial resolution. It is limited by geometrical optics constraints of the sample arm design, given by Abbe's criteria of the lateral resolution  $\Delta x = 0.61\lambda_o/NA$ , where NA is the numerical aperture of the objective lens.

## A2.3 Depth of Focus

It is dependent on the NA of the imaging optics. It is twice the Rayleigh range  $z_R$ , given by  $2z_R = 2\lambda_o n/NA^2$ , where  $n$  is the refractive index of the sample. Hence, increasing the NA increases the resolution (see above) but decreases the depth of focus quadratically. Thus, in OCT, a compromise has to be found between the lateral resolution and the depth of focus.

## A2.4 Imaging Depth

In the case of FD OCT, it depends on the center wavelength  $\lambda_o$  and the spectral resolution  $\Delta\lambda_{full}/N$ , given by  $z_{max} = \lambda_o^2 N / (4n\Delta\lambda_{full})$ , where  $\Delta\lambda_{full}$  is the total bandwidth of the light source and  $N$  is the number of spectral data points. In the case of TD OCT, the imaging depth is given by the reference arm travel range.

## A2.5 Detection Sensitivity

OCT, being an interferometric detection technique, boosts the weak backscattered optical field by effectively multiplying it with a strong reference field. In the shot noise limit, the power signal-to-noise ratio (SNR) performance of the OCT

system is given by  $SNR = 10 \log(\eta P_s/E_p B)$ , where  $P_s$  is the power at the detector backscattered from a single interface in the sample arm, which is proportional to the A-scan peak height,  $B$  is the bandwidth of electronic detection,  $\eta$  is the photodetector efficiency, and  $E_p = h\nu$  is the energy of the photon associated with the center frequency  $\nu$ .  $P_s$  is assumed to be much lower than the power from the reference arm. Sensitivity in OCT is defined as the inverse minimal sample reflectivity, which leads to an SNR of 1, i.e.,  $\Sigma = 1/R_{S,min}|SNR = 1$ . In the case of SS OCT, assuming a single sample reflector, the total power associated with the peak value of the interferometric portion of the A-scan after Fourier transform is, by Parvesal's theorem, half the sum of the power associated with each spectral point. In order to obtain an A-scan peak,  $N$  instantaneous sample exposures are done by an illuminating swept source if  $N$  spectral points are recorded. In the case of time domain (TD) OCT, the power associated with the peak value of an A-scan is due to a single exposure. The instantaneous exposure power (under the constraint of ANSI exposure) in the case of SS OCT can be same as in TD OCT. Thus, the power  $P_{ss}$  associated with the peak value of an A-scan in the case of SS OCT is about  $N$  times the power  $P_{td}$  associated with the A-scan peak of TD OCT.<sup>17</sup> Usually with bandwidth  $B$  being same for both TD and SS OCT (17), and  $N \geq 1024$ , a sensitivity advantage of ~20 to 30 dB is obtained for SS OCT over TD OCT. In the case of a spectrometer-based system, the detection of the spectral interference signal is done with a 1-D CCD array as shown in Fig. 21. The A-scan in this case is acquired by a single exposure as opposed to the case of TD OCT, where reference arm scanning is required. However, the total power is distributed among  $N$  channels of the spectrometer. Thus, the power associated with the peak after Fourier transform is  $P_{sd} = P_{td} = P_{ss}/N$ . However, the bandwidth  $B$  in this case is reduced by a factor  $1/N$  (17), and therefore, the effective SNR is same as in the case of SS OCT. The bandwidth can be related to the

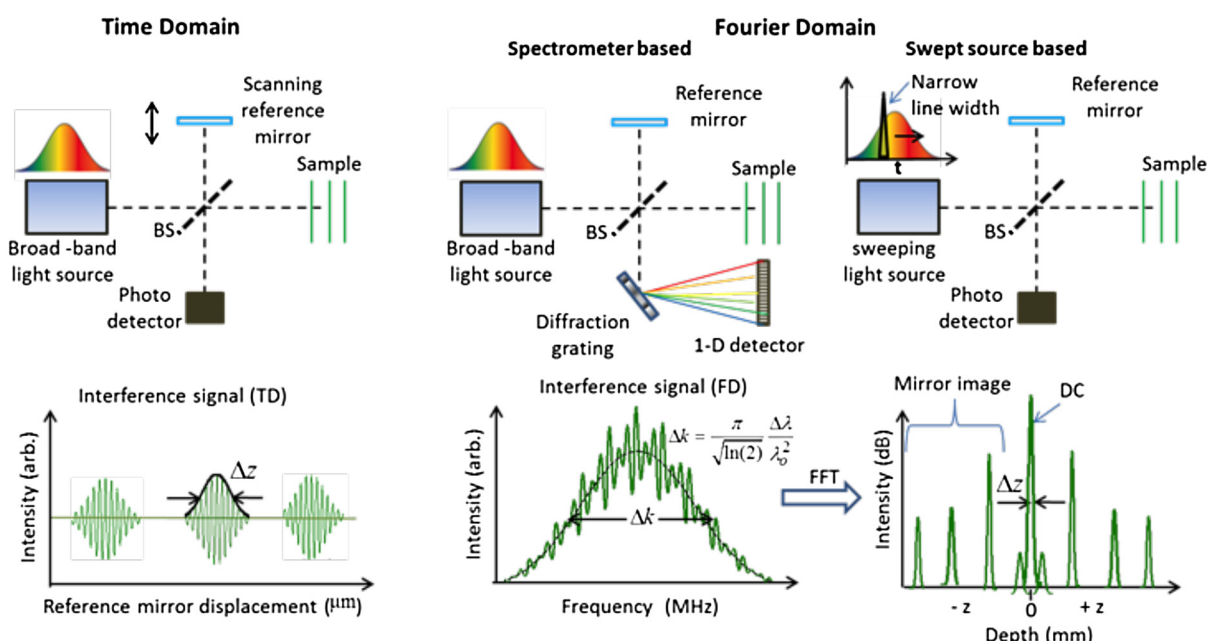


**Fig. 21** Schematic of different OCT modalities. OCT systems can be classified into time domain (TD) and Fourier domain (FD) systems. FD OCT systems can be divided into spectrometer based and swept source based systems.

exposure or A-scan time  $\tau$  as  $B = 1/(2\tau)$ . Hence, we see that FD OCT systems have 20 to 30 dB of sensitivity advantage over a TD OCT system.

Obviously, there is a tradeoff between the electronic bandwidth or the data acquisition rate and the SNR. Faster data acquisition speed results in degradation of SNR. Furthermore for the shot noise limited performance, an optimum optical power output from the light source is required for sample illumination. However, the power of the illumination is restricted by the maximum permissible ANSI exposure limit. Thus, there is a limitation to the maximum power that can be applied during the short exposure time of a high-speed OCT system. Hence, the OCT system design should be optimized according to the optical power limitations and data acquisition speed requirement.

## A2.6 Depth Penetration

OCT imaging at different wavelengths can be used to enhance tissue contrast and penetration, as well as to measure absorbing or scattering properties of various pigments and structures. Tissue scattering and absorption properties are strongly dependent on tissue morphology, such as cell and nuclei size, shape, and density, as well as the physiological state of certain chromophores. Hence, OCT penetration depth is significantly affected by light scattering within biological tissue, which is scaled as  $1/\lambda_o^k$ , where the coefficient  $k$  is dependent on the size, shape, and relative refractive index of the scattering particles (14). The difference in tissue scattering, which usually dominates over chromophore absorption, provides structural contrast for OCT. Most biological tissues absorb in the visible and near-IR wavelength range because of the presence of hemoglobin and melanin. In the range between 0.8 and 1.8  $\mu\text{m}$ , scattering and water absorption are the predominant mechanisms limiting image penetration depth. Since scattering depends strongly on wavelength and decreases for longer wavelengths, significantly better image penetration depth can be achieved with light centered at 1.35  $\mu\text{m}$  than at 0.85  $\mu\text{m}$ . It has been shown that the optimum wavelengths for imaging in opaque biological tissues are in the range of 1.3 to 1.5  $\mu\text{m}$ . In this range, imaging depths of 1 to 2 mm can be achieved (14). An exception is human retinal imaging, where water absorption becomes dominant due to the ocular media. There, the optimum wavelength is either between 750 and 850 nm, or in the region of 1.06  $\mu\text{m}$ . Water absorption becomes dominant for wavelengths  $>1.8 \mu\text{m}$ . A strong water absorption peak at  $\sim 1.43 \mu\text{m}$  can also reduce the spectral width of a broad bandwidth light source centered at 1.3  $\mu\text{m}$  as a function of depth in biological tissue, since most soft tissues have 50 to 90% water content. Hence, by choosing the center wavelength and bandwidth of the OCT light source from within the range of 500 to 1500 nm, axial resolution and contrast as well as penetration may be adjusted to the imaging procedure and medical application.

## Acknowledgments

This work is supported by the Medical University of Vienna, the European projects FAMOS (FP7 ICT 317744) and FUN OCT (FP7 HEALTH 201880), Macular Vision Research Foundation, Austrian Science Fund (FWF) project number S10510-N20, and the Christian Doppler Society (Christian Doppler Laboratory “Laser development and their application in medicine”).

## References

1. D. Huang et al., “Optical coherence tomography,” *Science* **254**(5035), 1178–1181 (1991).
2. B. Bouma and G. Tearney, *Handbook of Optical Coherence Tomography*, Taylor & Francis, USA (2001).
3. J. Schuman, C. Puliafito, and J. G. Fujimoto, *Everyday OCT: A Handbook for Clinicians and Technicians*, SLACK Incorporated, USA (2007).
4. W. Drexler and J. G. Fujimoto, *Optical Coherence Tomography: Technology and Applications*, Springer Publishing, Berlin, Heidelberg (2008).
5. A. F. Fercher and E. Roth, “Ophthalmic laser interferometer,” *Proc. SPIE* **658**, 48–51 (1986).
6. A. F. Fercher, K. Mengedoht, and W. Werner, “Eye length measurement by interferometer with partially coherent light,” *Opt. Lett.* **13**(3), 186–188 (1988).
7. J. G. Fujimoto et al., “Femtosecond optical ranging in biological systems,” *Opt. Lett.* **11**(3), 150–152 (1986).
8. M. Kemerink et al., “Characteristics of a first-generation x-ray system,” *Radiology* **259**(2), 534–539 (2011).
9. J. G. Fujimoto et al., “Optical biopsy and imaging using optical coherence tomography,” *Nat. Med.* **1**(9), 970–972 (1995).
10. B. E. Bouma et al., “Self-phase-modulated Kerr-lens mode-locked Cr:forsterite laser source for optical coherence tomography,” *Opt. Lett.* **21**(22), 1839–1841 (1996).
11. B. E. Bouma et al., “Optical coherence tomographic imaging using a mode locked Cr<sup>4+</sup>:Forsterite laser source,” presented at *Proc. of Ultrafast Phenomena 1997 OSA Technical Digest Series Vol. 8, 28 May–1 June 1997, San Diego, CA*, Opt. Soc. America, Washington, DC (1996).
12. W. Drexler et al., “In vivo ultrahigh-resolution optical coherence tomography,” *Opt. Lett.* **24**(17), 1221–1223 (1999).
13. W. Drexler et al., “Ultrahigh-resolution ophthalmic optical coherence tomography,” *Nat. Med.* **7**(4), 502–507 (2001).
14. W. Drexler, “Ultrahigh-resolution optical coherence tomography,” *J. Biomed. Opt.* **9**(1), 47–74 (2004).
15. A. F. Fercher et al., “Measurement of intraocular distances by backscattering spectral interferometry,” *Opt. Commun.* **117**(1–2), 43–48 (1995).
16. M. Wojtkowski et al., “In vivo human retinal imaging by Fourier domain optical coherence tomography,” *J. Biomed. Opt.* **7**(3), 457–463 (2002).
17. M. A. Choma et al., “Sensitivity advantage of swept source and Fourier domain optical coherence tomography,” *Opt. Express* **11**(18), 2183–2189 (2003).
18. R. Leitgeb, C. K. Hitzenberger, and A. F. Fercher, “Performance of Fourier domain vs. time domain optical coherence tomography,” *Opt. Express* **11**(8), 889–894 (2003).
19. B. Golubovic et al., “Optical frequency-domain reflectometry using rapid wavelength tuning of a Cr<sup>4+</sup>:forsterite laser,” *Opt. Lett.* **22**(22), 1704–1706 (1997).
20. S. Yun et al., “High-speed optical frequency-domain imaging,” *Opt. Express* **11**(22), 2953–2963 (2003).
21. R. Huber, M. Wojtkowski, and J. G. Fujimoto, “Fourier domain mode locking (FDML): a new laser operating regime and applications for optical coherence tomography,” *Opt. Express* **14**(8), 3225–3237 (2006).
22. T. Klein et al., “Megahertz OCT for ultrawide-field retinal imaging with a 1050 nm Fourier domain mode-locked laser,” *Opt. Express* **19**(4), 3044–3062 (2011).
23. T. Klein et al., “Multi-MHz retinal OCT,” *Biomed. Opt. Express* **4**(10), 1890–1908 (2013).
24. M. R. Hee et al., “Polarization-sensitive low-coherence reflectometer for birefringence characterization and ranging,” *J. Opt. Soc. Am. B* **9**(6), 903–908 (1992).
25. J. F. de Boer et al., “Two-dimensional birefringence imaging in biological tissue by polarization-sensitive optical coherence tomography,” *Opt. Lett.* **22**(12), 934–936 (1997).
26. C. Hitzenberger et al., “Measurement and imaging of birefringence and optic axis orientation by phase resolved polarization sensitive optical coherence tomography,” *Opt. Express* **9**(13), 780–790 (2001).
27. J. F. de Boer and T. E. Milner, “Review of polarization sensitive optical coherence tomography and Stokes vector determination,” *J. Biomed. Opt.* **7**(3), 359–371 (2002).

28. Y. Yasuno et al., "Birefringence imaging of human skin by polarization-sensitive spectral interferometric optical coherence tomography," *Opt. Lett.* **27**(20), 1803–1805 (2002).
29. C. K. Hitzenberger and A. F. Fercher, "Differential phase contrast in optical coherence tomography," *Opt. Lett.* **24**(9), 622–624 (1999).
30. A. Wax, S. Bali, and J. E. Thomas, "Time-resolved phase-space distributions for light backscattered from an disordered medium," *Phys. Rev. Lett.* **85**(1), 66–69 (2000).
31. C. H. Yang et al., "Interferometric phase-dispersion microscopy," *Opt. Lett.* **25**(20), 1526–1528 (2000).
32. C. K. Hitzenberger et al., "Differential phase measurements in low-coherence interferometry without 2 pi ambiguity," *Opt. Lett.* **26**(23), 1864–1866 (2001).
33. C. Yang et al., "Phase-dispersion optical tomography," *Opt. Lett.* **26**(10), 686–688 (2001).
34. J. M. Schmitt, "OCT elastography: imaging microscopic deformation and strain of tissue," *Opt. Express* **3**(6), 199–211 (1998).
35. R. C. Chan et al., "OCT-based arterial elastography: robust estimation exploiting tissue biomechanics," *Opt. Express* **12**(19), 4558–4572 (2004).
36. A. S. Khalil et al., "Tissue elasticity estimation with optical coherence elastography: toward mechanical characterization of *in vivo* soft tissue," *Ann. Biomed. Eng.* **33**(11), 1631–1639 (2005).
37. S. J. Kirkpatrick, R. K. Wang, and D. D. Duncan, "OCT-based elastography for large and small deformations," *Opt. Express* **14**(24), 11585–11597 (2006).
38. A. Nahas et al., "3D static elastography at the micrometer scale using full field OCT," *Biomed. Opt. Express* **4**(10), 2138–2149 (2013).
39. A. Nahas et al., "From supersonic shear wave imaging to full-field optical coherence shear wave elastography," *J. Biomed. Opt.* **18**(12), 121514 (2013).
40. M. D. Kulkarni and J. A. Izatt, "Spectroscopic optical coherence tomography," in *Conf. Proc. of Lasers and Electro Optics Society Annual Meeting*, pp. 59–60, CLEO, OSA, USA (1996).
41. U. Morgner et al., "Spectroscopic optical coherence tomography," *Opt. Lett.* **25**(2), 111–113 (2000).
42. D. J. Faber et al., "Light absorption of (oxy-)hemoglobin assessed by spectroscopic optical coherence tomography," *Opt. Lett.* **28**(16), 1436–1438 (2003).
43. D. C. Adler et al., "Optical coherence tomography contrast enhancement using spectroscopic analysis with spectral autocorrelation," *Opt. Express* **12**(22), 5487–5501 (2004).
44. A. Wax and J. E. Thomas, "Measurement of smoothed Wigner phase-space distributions for small-angle scattering in a turbid medium," *J. Opt. Soc. Am. A Opt. Image Sci. Vis.* **15**(7), 1896–1908 (1998).
45. A. Wax et al., "Measurement of angular distributions by use of low-coherence interferometry for light-scattering spectroscopy," *Opt. Lett.* **26**(6), 322–324 (2001).
46. A. Wax, C. H. Yang, and J. A. Izatt, "Fourier-domain low-coherence interferometry for light-scattering spectroscopy," *Opt. Lett.* **28**(14), 1230–1232 (2003).
47. T. M. Lee et al., "Engineered microsphere contrast agents for optical coherence tomography," *Opt. Lett.* **28**(17), 1546–1548 (2003).
48. D. L. Marks and S. A. Boppart, "Nonlinear interferometric vibrational imaging," *Phys. Rev. Lett.* **92**(12), 123905 (2004).
49. C. Vinegoni et al., "Nonlinear optical contrast enhancement for optical coherence tomography," *Opt. Express* **12**(2), 331–341 (2004).
50. C. Xu et al., "Separation of absorption and scattering profiles in spectroscopic optical coherence tomography using a least-squares algorithm," *Opt. Express* **12**(20), 4790–4803 (2004).
51. S. A. Boppart et al., "Optical probes and techniques for molecular contrast enhancement in coherence imaging," *J. Biomed. Opt.* **10**(4), 041208 (2005).
52. J. S. Bredfeldt et al., "Molecularly sensitive optical coherence tomography," *Opt. Lett.* **30**(5), 495–497 (2005).
53. R. L. Shelton et al., "Optical coherence tomography for advanced screening in the primary care office," *J. Biophotonics* (2013).
54. A. G. Podoleanu, "Optical coherence tomography," *J. Microsc.* **247**(3), 209–219 (2012).
55. W. Jung and S. A. Boppart, "Optical coherence tomography for rapid tissue screening and directed histological sectioning," *Anal. Cell Pathol. (Amst.)* **35**(3), 129–143 (2012).
56. G. Lamouche et al., "Review of tissue simulating phantoms with controllable optical, mechanical and structural properties for use in optical coherence tomography," *Biomed. Opt. Express* **3**(6), 1381–1398 (2012).
57. M. Wojtkowski, "High-speed optical coherence tomography: basics and applications," *Appl. Opt.* **49**(16), D30–D61 (2010).
58. A. M. Zysk et al., "Optical coherence tomography: a review of clinical development from bench to bedside," *J. Biomed. Opt.* **12**(5), 051403 (2007).
59. M. Wojtkowski, B. Kaluzny, and R. J. Zawadzki, "New directions in ophthalmic optical coherence tomography," *Optom. Vis. Sci.* **89**(5), 524–542 (2012).
60. J. L. Ramos, Y. Li, and D. Huang, "Clinical and research applications of anterior segment optical coherence tomography—a review," *Clin. Experiment. Ophthalmol.* **37**(1), 81–89 (2009).
61. W. Drexler and J. G. Fujimoto, "State-of-the-art retinal optical coherence tomography," *Prog. Retin. Eye Res.* **27**(1), 45–88 (2008).
62. T. Yonetstu et al., "Optical coherence tomography—15 years in cardiology," *Circ. J.* **77**(8), 1933–1940 (2013).
63. M. J. Suter et al., "Intravascular optical imaging technology for investigating the coronary artery," *JACC Cardiovasc. Imaging* **4**(9), 1022–1039 (2011).
64. H. C. Lowe et al., "Intracoronary optical diagnostics current status, limitations, and potential," *JACC Cardiovasc. Interv.* **4**(12), 1257–1270 (2011).
65. A. Tanaka, G. J. Tearney, and B. E. Bouma, "Challenges on the frontier of intracoronary imaging: atherosclerotic plaque macrophage measurement by optical coherence tomography," *J. Biomed. Opt.* **15**(1), 011104 (2010).
66. H. G. Bezerra et al., "Intracoronary optical coherence tomography: a comprehensive review clinical and research applications," *JACC Cardiovasc. Interv.* **2**(11), 1035–1046 (2009).
67. E. Sattler, R. Kastle, and J. Welzel, "Optical coherence tomography in dermatology," *J. Biomed. Opt.* **18**(6), 061224 (2013).
68. C. A. Banzhaf et al., "In vivo imaging of Sarcoptes scabiei infestation using optical coherence tomography," *Case Rep. Dermatol.* **5**(2), 156–162 (2013).
69. M. A. Boone et al., "High-definition optical coherence tomography imaging of melanocytic lesions: a pilot study," *Arch. Dermatol. Res.* **306**(1), 11–26 (2014).
70. M. A. Boone et al., "Imaging actinic keratosis by high-definition optical coherence tomography. Histomorphologic correlation: a pilot study," *Exp. Dermatol.* **22**(2), 93–97 (2013).
71. L. P. Hariri et al., "Seeing beyond the bronchoscope to increase the diagnostic yield of bronchoscopic biopsy," *Am. J. Respir. Crit. Care Med.* **187**(2), 125–129 (2013).
72. B. J. Vakoc et al., "Cancer imaging by optical coherence tomography: preclinical progress and clinical potential," *Nat. Rev. Cancer* **12**(5), 363–368 (2012).
73. X. Liang, V. Crecea, and S. A. Boppart, "Dynamic optical coherence elastography: a review," *J. Innov. Opt. Health Sci.* **3**(4), 221–233 (2010).
74. A. Ahmad et al., "Real-time computed optical interferometric tomography," *Nat. Photonics* **7**(6), 444–448 (2013).
75. R. Kafieh, H. Rabbani, and S. Kermani, "A review of algorithms for segmentation of optical coherence tomography from retina," *J. Med. Signals Sens.* **3**(1), 45–60 (2013).
76. R. Huber et al., "Fourier domain mode locking at 1050 nm for ultra-high-speed optical coherence tomography of the human retina at 236,000 axial scans per second," *Opt. Lett.* **32**(14), 2049–2051 (2007).
77. B. R. Biedermann et al., "Recent developments in Fourier domain mode locked lasers for optical coherence tomography: imaging at 1310 nm vs. 1550 nm wavelength," *J. Biophotonics* **2**(6–7), 357–363 (2009).
78. W. Wieser et al., "Multi-megahertz OCT: high quality 3D imaging at 20 million A-scans and 4.5 GVOXels per second," *Opt. Express* **18**(14), 14685–14704 (2010).
79. W. Drexler, "Ultrahigh resolution optical coherence tomography," *J. Biomed. Opt.* **9**(1), 47–74 (2004).
80. E. Beaurepaire et al., "Full-field optical coherence microscopy," *Opt. Lett.* **23**(4), 244–246 (1998).
81. A. C. Boccara et al., "D'etection analogique multicanal," French patent FR90.092255 (29 June 1990).
82. A. Dubois et al., "High-resolution full-field optical coherence tomography with a Linnik microscope," *Appl. Opt.* **41**(4), 805–812 (2002).

83. K. Grieve et al., "Ocular tissue imaging using ultrahigh-resolution, full-field optical coherence tomography," *Invest. Ophthalmol. Vis. Sci.* **45**(11), 4126–4131 (2004).
84. W. Y. Oh et al., "Ultrahigh-speed optical frequency domain imaging and application to laser ablation monitoring," *Appl. Phys. Lett.* **88**(10), 103902 (2006).
85. A. Dubois, G. Moneron, and C. Boccara, "Thermal-light full-field optical coherence tomography in the 1.2  $\mu\text{m}$  wavelength region," *Opt. Commun.* **266**(2), 738–743 (2006).
86. M. Jain et al., "Full-field optical coherence tomography for the analysis of fresh unstained human lobectomy specimens," *J. Pathol. Inform.* **4**, 26 (2013).
87. M. Laubscher et al., "Video-rate three-dimensional optical coherence tomography," *Opt. Express* **10**(9), 429–435 (2002).
88. W. Y. Oh et al., "Spectrally-modulated full-field optical coherence microscopy for ultrahigh-resolution endoscopic imaging," *Opt. Express* **14**(19), 8675–8684 (2006).
89. H. D. Ford et al., "Comparative signal-to-noise analysis of fibre-optic based optical coherence tomography systems," *J. Mod. Opt.* **52**(14), 1965–1979 (2005).
90. A. Latrive and A. C. Boccara, "In vivo and in situ cellular imaging full-field optical coherence tomography with a rigid endoscopic probe," *Biomed. Opt. Express* **2**(10), 2897–2904 (2011).
91. I. Zeylikovich, A. Gilerson, and R. R. Alfano, "Nonmechanical grating-generated scanning coherence microscopy," *Opt. Lett.* **23**(23), 1797–1799 (1998).
92. Y. Watanabe, K. Yamada, and M. Sato, "Three-dimensional imaging by ultrahigh-speed axial-lateral parallel time domain optical coherence tomography," *Opt. Express* **14**(12), 5201–5209 (2006).
93. M. Choma et al., "Sensitivity advantage of swept source and Fourier domain optical coherence tomography," *Opt. Express* **11**(18), 2183–2189 (2003).
94. A. F. Zuluaga and R. Richards-Kortum, "Spatially resolved spectral interferometry for determination of subsurface structure," *Opt. Lett.* **24**(8), 519–521 (1999).
95. B. Grajciar et al., "Parallel Fourier domain optical coherence tomography for in vivo measurement of the human eye," *Opt. Express* **13**(4), 1131–1137 (2005).
96. Y. Nakamura et al., "High-speed three-dimensional human retinal imaging by line-field spectral domain optical coherence tomography," *Opt. Express* **15**(12), 7103–7116 (2007).
97. Y. Yasuno et al., "Three-dimensional line-field Fourier domain optical coherence tomography for in vivo dermatological investigation," *J. Biomed. Opt.* **11**(1), 014014 (2006).
98. Y. Zhang et al., "Adaptive optics parallel spectral domain optical coherence tomography for imaging the living retina," *Opt. Express* **13**(12), 4792–4811 (2005).
99. S. Witte et al., "Single-shot two-dimensional full-range optical coherence tomography achieved by dispersion control," *Opt. Express* **17**(14), 11335–11349 (2009).
100. B. Hofer et al., "Dispersion encoded full range frequency domain optical coherence tomography," *Opt. Express* **17**(1), 7–24 (2009).
101. S. W. Lee and B. M. Kim, "Line-field optical coherence tomography using frequency-sweeping source," *IEEE J. Sel. Topics Quantum Electron.* **14**(1), 50–55 (2008).
102. T. Bonin et al., "In vivo Fourier-domain full-field OCT of the human retina with 1.5 million A-lines/s," *Opt. Lett.* **35**(20), 3432–3434 (2010).
103. M. K. Kim, "Tomographic three-dimensional imaging of a biological specimen using wavelength-scanning digital interference holography," *Opt. Express* **7**(9), 305–310 (2000).
104. D. Hillmann et al., "Efficient holoscopy image reconstruction," *Opt. Express* **20**(19), 21247–21263 (2012).
105. D. Hillmann et al., "Holoscopy—holographic optical coherence tomography," *Opt. Lett.* **36**(13), 2390–2392 (2011).
106. B. Povazay et al., "Full-field time-encoded frequency-domain optical coherence tomography," *Opt. Express* **14**(17), 7661–7669 (2006).
107. D. L. Marks et al., "Inverse scattering for frequency-scanned full-field optical coherence tomography," *J. Opt. Soc. Am. A Opt. Image Sci. Vis.* **24**(4), 1034–1041 (2007).
108. S. G. Adie et al., "Computational adaptive optics for broadband optical interferometric tomography of biological tissue," *Proc. Natl. Acad. Sci. U S A* **109**(19), 7175–7180 (2012).
109. A. Kumar, W. Drexler, and R. A. Leitgeb, "Subaperture correlation based digital adaptive optics for full field optical coherence tomography," *Opt. Express* **21**(9), 10850–10866 (2013).
110. A. H. Dhalla, J. V. Migacz, and J. A. Izatt, "Crosstalk rejection in parallel optical coherence tomography using spatially incoherent illumination with partially coherent sources," *Opt. Lett.* **35**(13), 2305–2307 (2010).
111. P. Krížek, I. Raška, and G. M. Hagen, "Flexible structured illumination microscope with a programmable illumination array," *Optics Express* **20**(22), 24585–24599 (2012).
112. Y. Zhao et al., "Phase-resolved optical coherence tomography and optical Doppler tomography for imaging blood flow in human skin with fast scanning speed and high velocity sensitivity," *Opt. Lett.* **25**(2), 114–116 (2000).
113. V. Yang et al., "High speed, wide velocity dynamic range Doppler optical coherence tomography (Part I): System design, signal processing, and performance," *Opt. Express* **11**(7), 794–809 (2003).
114. M. A. Choma et al., "Sensitivity advantage of swept source and Fourier domain optical coherence tomography," *Opt. Express* **11**(18), 2183–2189 (2003).
115. S. Makita et al., "Optical coherence angiography," *Opt. Express* **14**(17), 7821–7840 (2006).
116. B. H. Park et al., "Real-time fiber-based multi-functional spectral-domain optical coherence tomography at 1.3  $\mu\text{m}$ ," *Opt. Express* **13**(11), 3931–3944 (2005).
117. S. H. Yun et al., "Motion artifacts in optical coherence tomography with frequency-domain ranging," *Opt. Express* **12**(13), 2977–2998 (2004).
118. A. H. Bachmann et al., "Resonant Doppler flow imaging and optical vivisection of retinal blood vessels," *Opt. Express* **15**(2), 408–422 (2007).
119. Y. K. Tao, A. M. Davis, and J. A. Izatt, "Single-pass volumetric bidirectional blood flow imaging spectral domain optical coherence tomography using a modified Hilbert transform," *Opt. Express* **16**(16), 12350–12361 (2008).
120. L. An and R. K. Wang, "In vivo volumetric imaging of vascular perfusion within human retina and choroids with optical microangiography," *Opt. Express* **16**(15), 11438–11452 (2008).
121. C. Kolbitsch, T. Schmoll, and R. A. Leitgeb, "Histogram-based filtering for quantitative 3D retinal angiography," *J. Biophotonics* **2**(6–7), 416–425 (2009).
122. A. S. G. Singh, T. Schmoll, and R. A. Leitgeb, "Segmentation of Doppler optical coherence tomography signatures using a support-vector machine," *Biomed. Opt. Express* **2**(5), 1328–1339 (2011).
123. E. Dittrich et al., "Detection of capillary vessels in optical coherence tomography based on a probabilistic kernel," in *Proc. 13th Annual Meeting, Medical Image Understanding and Analysis*, A. H. Bhalerao and N. M. Rajpoot, Eds., pp. 37–41, University of Warwick, Warwick (2009).
124. T. Schmoll et al., "Imaging of the parafoveal capillary network and its integrity analysis using fractal dimension," *Biomed. Opt. Express* **2**(5), 1159–1168 (2011).
125. V. Kaji et al., "Automated three-dimensional choroidal vessel segmentation of 3D 1060 nm OCT retinal data," *Biomed. Opt. Express* **4**(1), 134–150 (2013).
126. F. Jaillon et al., "Enhanced imaging of choroidal vasculature by high-penetration and dual-velocity optical coherence angiography," *Biomed. Opt. Express* **2**(5), 1147–1158 (2011).
127. S. Zotter et al., "Visualization of microvasculature by dual-beam phase-resolved Doppler optical coherence tomography," *Opt. Express* **19**(2), 1217–1227 (2011).
128. F. Jaillon, S. Makita, and Y. Yasuno, "Variable velocity range imaging of the choroid with dual-beam optical coherence angiography," *Opt. Express* **20**(1), 385–396 (2012).
129. T. Schmoll, C. Kolbitsch, and R. A. Leitgeb, "Ultra-high-speed volumetric tomography of human retinal blood flow," *Opt. Express* **17**(5), 4166–4176 (2009).
130. W. Choi et al., "Choriocapillaris and choroidal microvasculature imaging with ultrahigh speed OCT angiography," *PLoS ONE* **8**(12), e81499 (2013).
131. M. Szkulmowski et al., "Flow velocity estimation using joint spectral and time domain optical coherence tomography," *Opt. Express* **16**(9), 6008–6025 (2008).

132. P. Meemon and J. P. Rolland, "Swept-source based, single-shot, multi-detectable velocity range Doppler optical coherence tomography," *Biomed. Opt. Express* **1**(3), 955–966 (2010).
133. C. Blatter et al., "Dove prism based rotating dual beam bidirectional Doppler OCT," *J. Biomed. Opt.* **4**(7), 1188–1203 (2013).
134. I. Grulkowski et al., "Scanning protocols dedicated to smart velocity ranging in spectral OCT," *Opt. Express* **17**(26), 23736–23754 (2009).
135. B. Braaf et al., "Angiography of the retina and the choroid with phase-resolved OCT using interval-optimized backstitched B-scans," *Opt. Express* **20**(18), 20516–20534 (2012).
136. M. S. Mahmud et al., "Review of speckle and phase variance optical coherence tomography to visualize microvascular networks," *J. Biomed. Opt.* **18**(5), 050901 (2013).
137. D. Y. Kim et al., "In vivo volumetric imaging of human retinal circulation with phase-variance optical coherence tomography," *Biomed. Opt. Express* **2**(6), 1504–1513 (2011).
138. B. J. Vakoc et al., "Three-dimensional microscopy of the tumor microenvironment in vivo using optical frequency domain imaging," *Nat. Med.* **15**(10), 1219–1223 (2009).
139. A. Mariampillai et al., "Speckle variance detection of microvasculature using swept-source optical coherence tomography," *Opt. Lett.* **33**(13), 1530–1532 (2008).
140. J. Barton and S. Stromski, "Flow measurement without phase information in optical coherence tomography images," *Opt. Express* **13**(14), 5234–5239 (2005).
141. L. An, J. Qin, and R. K. Wang, "Ultrahigh sensitive optical microangiography for in vivo imaging of microcirculations within human skin tissue beds," *Opt. Express* **18**(8), 8220–8228 (2010).
142. C. Blatter et al., "Ultrahigh-speed non-invasive widefield angiography," *J. Biomed. Opt.* **17**(7), 070505 (2012).
143. C. Blatter et al., "Extended focus high-speed swept source OCT with self-reconstructive illumination," *Opt. Express* **19**(13), 12141–12155 (2011).
144. B. Povazay et al., "Enhanced visualization of choroidal vessels using ultrahigh resolution ophthalmic OCT at 1050 nm," *Opt. Express* **11**(17), 1980–1986 (2003).
145. Y. Yasuno et al., "In vivo high-contrast imaging of deep posterior eye by 1- $\mu\text{m}$  swept source optical coherence tomography and scattering optical coherence angiography," *Opt. Express* **15**(10), 6121–6139 (2007).
146. A. Mariampillai et al., "Optimized speckle variance OCT imaging of microvasculature," *Opt. Lett.* **35**(8), 1257–1259 (2010).
147. C. Blatter et al., "In situ structural and microangiographic assessment of human skin lesions with high-speed OCT," *Biomed. Opt. Express* **3**(10), 2636–2646 (2012).
148. S. Yazdanfar, M. Kulkarni, and J. Izatt, "High resolution imaging of in vivo cardiac dynamics using color Doppler optical coherence tomography," *Opt. Express* **1**(13), 424–431 (1997).
149. R. A. Leitgeb et al., "Real-time assessment of retinal blood flow with ultrafast acquisition by color Doppler Fourier domain optical coherence tomography," *Opt. Express* **11**(23), 3116–3121 (2003).
150. G. Liu et al., "A comparison of Doppler optical coherence tomography methods," *Biomed. Opt. Express* **3**(10), 2669–2680 (2012).
151. J. Lee et al., "Dynamic light scattering optical coherence tomography," *Opt. Express* **20**(20), 22262–22277 (2012).
152. M. H. Bernstein and M. J. Hollenberg, "Fine structure of the chorio-capillaris and retinal capillaries," *Invest. Ophthalmol. Vis. Sci.* **4**(6), 1016–1025 (1965).
153. S. H. Hardarson et al., "Automatic retinal oximetry," *Invest. Ophthalmol. Vis. Sci.* **47**(11), 5011–5016 (2006).
154. F. C. Delori, "Noninvasive technique for oximetry of blood in retinal vessels," *Appl. Opt.* **27**(6), 1113–1125 (1988).
155. M. C. Skala et al., "Combined hyperspectral and spectral domain optical coherence tomography microscope for noninvasive hemodynamic imaging," *Opt. Lett.* **34**(3), 289–291 (2009).
156. L. V. Wang, "Multiscale photoacoustic microscopy and computed tomography," *Nat. Photonics* **3**(9), 503–509 (2009).
157. H. F. Zhang et al., "Functional photoacoustic microscopy for high-resolution and noninvasive in vivo imaging," *Nat. Biotechnol.* **24**(7), 848–851 (2006).
158. K. K. C. Lee et al., "Real-time speckle variance swept-source optical coherence tomography using a graphics processing unit," *Biomed. Opt. Express* **3**(7), 1557–1564 (2012).
159. T. M. Lee et al., "Engineered microsphere contrast agents for optical coherence tomography," *Opt. Lett.* **28**(17), 1546–1548 (2003).
160. W. Denk, J. H. Strickler, and W. W. Webb, "Two-photon laser scanning fluorescence microscopy," *Science* **248**(4951), 73–76 (1990).
161. F. S. Pavone and P. J. Campagnola, *Second Harmonic Generation Imaging*, p. 479, CRC Press, Boca Raton, FL (2013).
162. J. Squier et al., "Third harmonic generation microscopy," *Opt. Express* **3**(9), 315–324 (1998).
163. M. D. Duncan, J. Reintjes, and T. J. Manuccia, "Scanning coherent anti-Stokes Raman microscope," *Opt. Lett.* **7**(8), 350–352 (1982).
164. C. V. Raman and K. S. Krishnan, "A new type of secondary radiation," *Nature* **121**, 501–502 (1928).
165. A. C. T. Ko et al., "Ex vivo detection and characterization of early dental caries by optical coherence tomography and Raman spectroscopy," *J. Biomed. Opt.* **10**(3), 031118 (2005).
166. C. A. Patil et al., "Combined Raman spectroscopy and optical coherence tomography device for tissue characterization," *Opt. Lett.* **33**(10), 1135–1137 (2008).
167. C. A. Patil et al., "A clinical instrument for combined Raman spectroscopy—optical coherence tomography of skin cancers," *Lasers Surg. Med.* **43**(2), 143–151 (2011).
168. J. W. Evans et al., "Optical coherence tomography and Raman spectroscopy of the ex-vivo retina," *J. Biophotonics* **2**(6–7), 398–406 (2009).
169. P. C. Ashok et al., "Multi-modal approach using Raman spectroscopy and optical coherence tomography for the discrimination of colonic adenocarcinoma from normal colon," *Biomed. Opt. Express* **4**(10), 2179–2186 (2013).
170. K. M. Khan et al., "Depth-sensitive Raman spectroscopy combined with optical coherence tomography for layered tissue analysis," *J. Biophotonics* **7**(1–2), 77–85 (2014).
171. A. Zumbusch, G. R. Holtom, and X. S. Xie, "Three-dimensional vibrational imaging by coherent anti-Stokes Raman scattering," *Phys. Rev. Lett.* **82**, 4142–4145 (1999).
172. E. O. Potma and X. S. Xie, "CARS microscopy for biology and medicine," *Opt. Photon. News* **15**(11), 40–45 (2004).
173. D. L. Marks et al., "Interferometric differentiation between resonant coherent anti-Stokes Raman scattering and nonresonant four-wave-mixing processes," *Appl. Phys. Lett.* **85**(23), 5787–5789 (2004).
174. M. Göppert-Mayer, "Über Elementarkräfte mit zwei Quantensprüngen," *Annalen der Physik* **401**(3), 273–294 (1931).
175. W. Kaiser and C. G. Garrett, "Two-photon excitation in CaF<sub>2</sub>: Eu<sup>2+</sup>," *Phys. Rev. Lett.* **7**(6), 229–231 (1961).
176. W. R. Zipfel et al., "Live tissue intrinsic emission microscopy using multiphoton-excited native fluorescence and second harmonic generation," *Proc. Natl. Acad. Sci. U.S.A.* **100**(12), 7075–7080 (2003).
177. I. Freund, M. Deutsch, and A. Sprecher, "Connective tissue polarity. Optical second-harmonic microscopy, crossed-beam summation, and small-angle scattering in rat-tail tendon," *Biophys. J.* **50**(4), 693–712 (1986).
178. Y. Jiang et al., "Second-harmonic optical coherence tomography," *Opt. Lett.* **29**(10), 1090–1092 (2004).
179. B. E. Applegate et al., "Polarization-resolved second-harmonic-generation optical coherence tomography in collagen," *Opt. Lett.* **29**(19), 2252–2254 (2004).
180. P. Fratzl, *Collagen: Structure and Mechanics*, p. 524, Springer, New York (2008).
181. P. Jeannesson, "Impact of carbamylation and glycation of collagen type I on migration of HT1080 human fibrosarcoma cells," *Int. J. Oncol.* **40**(6), 1797–1804 (2012).
182. M. J. Farrar et al., "In vivo imaging of myelin in the vertebrate central nervous system using third harmonic generation microscopy," *Biophys. J.* **100**(5), 1362–1371 (2011).
183. E. Beaurepaire et al., "Combined scanning optical coherence and two-photon-excited fluorescence microscopy," *Opt. Lett.* **24**(14), 969–971 (1999).
184. R. V. Kurano et al., "Combined application of optical methods to increase the information content of optical coherent tomography in diagnostics of neoplastic processes," *Quantum Electron.* **32**(11), 993 (2002).

185. Y. T. Pan et al., "Enhancing early bladder cancer detection with fluorescence-guided endoscopic optical coherence tomography," *Opt. Lett.* **28**(24), 2485–2487 (2003).
186. J. Liu et al., "In vivo bladder imaging with microelectromechanical-systems-based endoscopic spectral domain optical coherence tomography," *J. Biomed. Opt.* **12**(3), 034009 (2007).
187. A. T. Yeh et al., "Imaging wound healing using optical coherence tomography and multiphoton microscopy in an in vitro skin-equivalent tissue model," *J. Biomed. Opt.* **9**(2), 248–253 (2004).
188. C. Vinegoni et al., "Integrated structural and functional optical imaging combining spectral-domain optical coherence and multiphoton microscopy," *Appl. Phys. Lett.* **88**(5), 053901 (2006).
189. J. A. Jo et al., "In vivo simultaneous morphological and biochemical optical imaging of oral epithelial cancer," *IEEE Trans. Biomed. Eng.* **57**(10), 2596–2599 (2010).
190. G. M. Dobre, A. G. Podoleanu, and R. B. Rosen, "Simultaneous optical coherence tomography—indocyanine green dye fluorescence imaging system for investigations of the eye's fundus," *Opt. Lett.* **30**(1), 58–60 (2005).
191. R. B. Rosen et al., "Simultaneous OCT/SLO/ICG imaging," *Invest. Ophthalmol. Vis. Sci.* **50**(2), 851–860 (2008).
192. Q. Wu, B. E. Applegate, and A. T. Yeh, "Cornea microstructure and mechanical responses measured with nonlinear optical and optical coherence microscopy using sub-10-fs pulses," *Biomed. Opt. Express* **2**(5), 1135–1146 (2011).
193. S. P. Chong et al., "Tri-modal microscopy with multiphoton and optical coherence microscopy/tomography for multi-scale and multi-contrast imaging," *Biomed. Opt. Express* **4**(9), 1584–1594 (2013).
194. C. Dai, X. Liu, and S. Jiao, "Simultaneous optical coherence tomography and autofluorescence microscopy with a single light source," *J. Biomed. Opt.* **17**(8), 080502 (2012).
195. S. Tang et al., "Combined multiphoton microscopy and optical coherence tomography using a 12-fs broadband source," *J. Biomed. Opt.* **11**(2), 020502 (2006).
196. S. Yazdanfar et al., "Multifunctional imaging of endogenous contrast by simultaneous nonlinear and optical coherence microscopy of thick tissues," *Micrsc. Res. Techn.* **70**(7), 628–633 (2007).
197. A. Bradu et al., "Dual optical coherence tomography/fluorescence microscopy for monitoring of *Drosophila melanogaster* larval heart," *J. Biophotonics* **2**(6–7), 380–388 (2009).
198. B. W. Graf et al., "Dual-spectrum laser source based on fiber continuum generation for integrated optical coherence and multiphoton microscopy," *J. Biomed. Opt.* **14**(3), 034019 (2009).
199. B. Jeong et al., "Combined two-photon microscopy and optical coherence tomography using individually optimized sources," *Opt. Express* **19**(14), 13089–13096 (2011).
200. K. König et al., "Clinical optical coherence tomography combined with multiphoton tomography of patients with skin diseases," *J. Biophotonics* **2**(6–7), 389–397 (2009).
201. K. König, "Hybrid multiphoton multimodal tomography of in vivo human skin," *IntraVital* **1**(1), 11–26 (2012).
202. A. Alex et al., "Three-dimensional multiphoton/optical coherence tomography for diagnostic applications in dermatology," *J. Biophotonics* **6**(4), 352–362 (2013).
203. Y. Zhao et al., "Integrated multimodal optical microscopy for structural and functional imaging of engineered and natural skin," *J. Biophotonics* **5**(5–6), 437–448 (2012).
204. B. W. Graf et al., "In vivo multimodal microscopy for detecting bone-marrow-derived cell contribution to skin regeneration," *J. Biophotonics* **7**(1–2), 96–102 (2014).
205. A. R. Tumlinson et al., "Miniature endoscope for simultaneous optical coherence tomography and laser-induced fluorescence measurement," *Appl. Opt.* **43**(1), 113–121 (2004).
206. J. B. McNally et al., "Task-based imaging of colon cancer in the Apc(Min+)/ mouse model," *Appl. Opt.* **45**(13), 3049–3062 (2006).
207. L. P. Hariri et al., "Endoscopic optical coherence tomography and laser-induced fluorescence spectroscopy in a murine colon cancer model," *Lasers Surg. Med.* **38**(4), 305–313 (2006).
208. L. P. Hariri et al., "Serial endoscopy in azoxymethane treated mice using ultra-high resolution optical coherence tomography," *Cancer Biol. Ther.* **6**(11), 1753–1762 (2007).
209. S. Yuan et al., "Combining optical coherence tomography with fluorescence molecular imaging: towards simultaneous morphology and molecular imaging," *Phys. Med. Biol.* **55**(1), 191–206 (2010).
210. J. Xi et al., "Integrated multimodal endomicroscopy platform for simultaneous en face optical coherence and two-photon fluorescence imaging," *Opt. Lett.* **37**(3), 362–364 (2012).
211. M. Wojtkowski et al., "In vivo human retinal imaging by Fourier domain optical coherence tomography," *J. Biomed. Opt.* **7**(3), 457–463 (2002).
212. I.-K. Jang et al., "Visualization of coronary atherosclerotic plaques in patients using optical coherence tomography: comparison with intravascular ultrasound," *J. Am. Coll. Cardiol.* **39**(4), 604–609 (2002).
213. W. Wieser et al., "Extended coherence length megahertz FDML and its application for anterior segment imaging," *Biomed. Opt. Express* **3**(10), 2647–2657 (2012).
214. J. Dunkers, M. Cicerone, and N. Washburn, "Collinear optical coherence and confocal fluorescence microscopies for tissue engineering," *Opt. Express* **11**(23), 3074–3079 (2003).
215. X. J. Wang, T. E. Milner, and J. S. Nelson, "Characterization of fluid flow velocity by optical Doppler tomography," *Opt. Lett.* **20**(11), 1337–1339 (1995).
216. C. E. Saxon et al., "High-speed fiber based polarization-sensitive optical coherence tomography of in vivo human skin," *Opt. Lett.* **25**(18), 1355–1357 (2000).
217. Y. N. Billeh, M. Liu, and T. Buma, "Spectroscopic photoacoustic microscopy using a photonic crystal fiber supercontinuum source," *Opt. Express* **18**(18), 18519–18524 (2010).
218. C. Zhang et al., "Reflection-mode submicron-resolution in vivo photoacoustic microscopy," *J. Biomed. Opt.* **17**(2), 020501 (2012).
219. J. Laufer et al., "In vivo preclinical photoacoustic imaging of tumor vasculature development and therapy," *J. Biomed. Opt.* **17**(5), 056016 (2012).
220. S. Hu, K. Maslov, and L. V. Wang, "Second-generation optical-resolution photoacoustic microscopy with improved sensitivity and speed," *Opt. Lett.* **36**(7), 1134–1136 (2011).
221. M. Liu, "A study of spectral domain optical coherence tomography and photoacoustic microscopy for biometric and biomedical applications," M.S. Thesis, University of Delaware, Newark, Delaware (2011).
222. M. Liu et al., "In vivo three dimensional dual wavelength photoacoustic tomography imaging of the far red fluorescent protein E2-Crimson expressed in adult zebrafish," *Biomed. Opt. Express* **4**(10), 1846–1855 (2013).
223. M. Liu et al., "In vivo spectroscopic photoacoustic tomography imaging of a far red fluorescent protein expressed in the exocrine pancreas of adult zebrafish," *Proc. SPIE* **8943**, 894341 (2014).
224. J. A. Viator et al., "Clinical testing of a photoacoustic probe for port wine stain depth determination," *Lasers Surg. Med.* **30**(2), 141–148 (2002).
225. G. J. Tearney et al., "Scanning single-mode fiber optic catheter-endoscope for optical coherence tomography," *Opt. Lett.* **21**(7), 543–545 (1996).
226. J.-M. Yang et al., "Photoacoustic endoscopy," *Opt. Lett.* **34**(10), 1591–1593 (2009).
227. J.-M. Yang et al., "A 2.5-mm diameter probe for photoacoustic and ultrasonic endoscopy," *Opt. Express* **20**(21), 23944–23953 (2012).
228. Y. Yang et al., "Integrated optical coherence tomography, ultrasound and photoacoustic imaging for ovarian tissue characterization," *Biomed. Opt. Express* **2**(9), 2551–2561 (2011).
229. L. Li et al., "Three-dimensional combined photoacoustic and optical coherence microscopy for in vivo microcirculation studies," *Opt. Express* **17**(19), 16450–16455 (2009).
230. S. Jiao et al., "Simultaneous multimodal imaging with integrated photoacoustic microscopy and optical coherence tomography," *Opt. Lett.* **34**(19), 2961–2963 (2009).
231. C. Lee et al., "Combined photoacoustic and optical coherence tomography using a single near-infrared supercontinuum laser source," *Appl. Opt.* **52**(9), 1824–1828 (2013).
232. X. Zhang, H. F. Zhang, and S. Jiao, "Optical coherence photoacoustic microscopy: accomplishing optical coherence tomography and photo-acoustic microscopy with a single light source," *J. Biomed. Opt.* **17**(3), 030502 (2012).
233. L. Xi et al., "Miniature probe combining optical-resolution photo-acoustic microscopy and optical coherence tomography for in vivo microcirculation study," *Appl. Opt.* **52**(9), 1928–1931 (2013).

234. T. Liu et al., "Combined photoacoustic microscopy and optical coherence tomography can measure metabolic rate of oxygen," *Biomed. Opt. Express* **2**(5), 1359–1365 (2011).
235. X. Cai et al., "Investigation of neovascularization in three-dimensional porous scaffolds in vivo by a combination of multiscale photoacoustic microscopy and optical coherence tomography," *Tissue Eng. Part C Methods* **19**(3), 196–204 (2013).
236. V. Tsytarev et al., "Photoacoustic and optical coherence tomography of epilepsy with high temporal and spatial resolution and dual optical contrasts," *J. Neurosci. Methods* **216**(2), 142–145 (2013).
237. S. Jiao et al., "Photoacoustic ophthalmoscopy for in vivo retinal imaging," *Opt. Express* **18**(4), 3967–3972 (2010).
238. B. Cox et al., "Quantitative spectroscopic photoacoustic imaging: a review," *J. Biomed. Opt.* **17**(6), 061202 (2012).
239. L. Wang et al., "Fast voice-coil scanning optical-resolution photoacoustic microscopy," *Opt. Lett.* **36**(2), 139–141 (2011).
240. E. Z. Zhang et al., "Multimodal photoacoustic and optical coherence tomography scanner using an all optical detection scheme for 3D morphological skin imaging," *Biomed. Opt. Express* **2**(8), 2202–2215 (2011).
241. B. E. Treeby and B. T. Cox, "k-Wave: MATLAB toolbox for the simulation and reconstruction of photoacoustic wave fields," *J. Biomed. Opt.* **15**(2), 021314 (2010).
242. W. Shi et al., "In vivo near-realtime volumetric optical-resolution photoacoustic microscopy using a high-repetition-rate nanosecond fiber-laser," *Opt. Express* **19**(18), 17143–17150 (2011).
243. P. Shao et al., "Mosaic acquisition and processing for optical-resolution photoacoustic microscopy," *J. Biomed. Opt.* **17**(8), 080503 (2012).
244. W. Träischker et al., "In vitro and in vivo three-dimensional velocity vector measurement by three-beam spectral-domain Doppler optical coherence tomography," *J. Biomed. Opt.* **18**(11), 116010 (2013).
245. M. Liu and T. Buma, "Biometric mapping of fingertip eccrine glands with optical coherence tomography," *IEEE Photonics Technol. Lett.* **22**(22), 1677–1679 (2010).

**Wolfgang Drexler** received his MS and PhD in electrical engineering from the Technical University of Vienna, Austria. He spent two years (1998 to 1999) at the Massachusetts Institute of Technology, Cambridge, and from 2006 to 2009, he was a full professor of biomedical imaging at Cardiff University, Wales, United Kingdom. Since 2009, he has been a full professor of medical physics and the head of the Center for Medical Physics and Biomedical Engineering at the Medical University of Vienna, Austria.

**Mengyang Liu** is a PhD student at the Medical University of Vienna, Austria. He received his MSc degree in electrical and computer engineering from the University of Delaware. His research interests span from photoacoustic microscopy and photoacoustic tomography to optical coherence tomography. He is currently developing novel photoacoustic systems as well as conducting small animal experiments.

**Abhishek Kumar** earned his master's degree in optics from the Institute of Optics, Rochester, New York, in 2011. He is currently pursuing his PhD research in full field optical coherence tomography (OCT) at the Medical University of Vienna. His research interests include novel imaging and image reconstruction techniques, digital wavefront sensing, and lens-less imaging.

**Tschackad Kamali** completed his master's degree in biomedical engineering from the University of Applied Sciences Mittelhessen, Germany, in March 2010. In September 2011, he received his master's degree in medical physics at the interface between medical physics from the University of Applied Sciences Mittelhessen and the Biophotonics group at the University of Otago, New Zealand. Currently, his PhD studies cover the field of OCT and nonlinear imaging (second harmonic generation, coherent anti-Stokes Raman scattering).

**Angelika Unterhuber** has 15 years of experience in ultrafast optics. She received her PhD from the Vienna University of Technology and worked as an R&D engineer in different laser-related companies. From 2006 to 2009, she stayed at the School of Optometry and Vision Sciences at Cardiff University. Currently, she works at the Medical University of Vienna, focused on the development of novel light sources and their biomedical application in the field of OCT and nonlinear imaging.

**Rainer A. Leitgeb** received his PhD in theoretical physics from the Technical University Vienna, Austria, in 1998 and then joined the Department of Medical Physics, University of Vienna. From 2004 to 2007, he worked at the EPFL, Switzerland, as project leader. Since 2007, he has been an associate professor of medical physics at the Medical University Vienna specializing on functional and multimodal tomography, and advanced microscopy. In 2014, he was elected a fellow of SPIE.